

IMPROVING MODELING AND SIMULATION OF
RAINFALL-INDUCED LANDSLIDES: FROM PREDICTION
TO POST-FAILURE DYNAMICS

Ph.D. Dissertation

Nunziarita Palazzolo



University of Pavia

DICAr - Department of Civil Engineering and Architecture

A thesis submitted for the degree of Doctor of Philosophy in

Design, Modeling And, Simulation in Engineering

XXXIV Cycle

IMPROVING MODELING AND SIMULATION OF
RAINFALL-INDUCED LANDSLIDES: FROM PREDICTION
TO POST-FAILURE DYNAMICS

Nunziarita PALAZZOLO

Supervisor: Prof. Enrico CREACO

Co-supervisors: Prof. Antonino CANCELLIERE, Dr. David Johnny PERES,
Prof. Sauro MANENTI

Ph.D. coordinator: Prof. Alessandro REALI

Pavia, June 2022

Contents

Abstract	5
Chapter 1 Introduction	7
Abstract.....	7
1.1 Overview	8
1.2 Aim of the research	11
1.3 Outline of the dissertation	11
Chapter 2 Literature review	15
Abstract.....	15
2.1 Landslides triggered by rainfall.....	16
2.2 Empirical models	20
2.3 Physically-based models	24
2.4 Runout analysis	28
Chapter 3 Soil moisture information for improving landslide prediction	31
Abstract.....	31
3.1. Main hydraulic soil factors influencing landslides	32
3.2. In situ soil moisture measurements.....	36
3.3. Remote sensing soil moisture data	39
3.4. Reanalysis soil moisture data	41
Chapter 4 Identification of regional landslide triggering thresholds using multivariate statistical analysis and reanalysis soil moisture data	47
Abstract.....	47
4.1. Introduction	49
4.2. Materials and method.....	52

4.2.1. Dataset creation.....	52
4.2.2. Principal components analysis.....	55
4.2.3. Thresholds identification	57
4.3. Study area.....	61
4.4. Results and discussion	63
4.4.1. Principal component analysis	63
4.4.2. Analysis using observed rainfall.....	65
4.4.3. Analysis using ERA5-Land rainfall.....	72
4.5. Conclusions.....	78
Chapter 5 Improving Spatial Landslide Prediction with 3D Slope Stability Analysis and Genetic Algorithm Optimization.....	79
Abstract.....	79
5.1. Introduction	81
5.2. Materials and methods.....	84
5.2.1. Pressure Head Computation by TRIGRS Model (The Transient Infiltration and Grid-Based Regional Slope-Stability Model – v.2.1)	86
5.2.2. Slope Stability Analysis by TRIGRS Model (The Transient Rainfall Infiltration and Grid-Based Regional Slope-Stability Model – v.2.1)	89
5.2.3. Slope Stability Analysis by SCOOPS 3D Model (Software to Analyze Three-Dimensional Slope-Stability throughout a Digital Landscape)	90
5.2.4. SCOOPS 3D Search Grid Configuration and Optimization by NSGAI Genetic algorithm.....	93
5.3. Simulation framework.....	96
5.4. Study area.....	97
5.5. Results and discussion	101

5.6. Conclusions.....	108
Chapter 6 Post-Failure Dynamics of Rainfall-Induced Landslide in Oltrepò Pavese.....	111
Abstract.....	111
6.1. Introduction.....	112
6.2. Model description and Test Case Configuration.....	115
6.3. Results and discussion	121
6.3.1. Analysis of viscosity	122
6.3.2. Validation.....	125
6.3.3. Influence of input parameters.....	127
6.4. Conclusions.....	131
6.5. Acknowledgment.....	132
Chapter 7 Conclusions	133
7.1 Main conclusions.....	133
7.2 Limitations and future perspectives.....	135
Acknowledgments.....	137
List of symbols.....	139
List of figures.....	143
List of tables.....	149
References	151

Abstract

Landslides are a natural hazard that cause impactful effects not only on the earth's natural environment (i.e., morphology, flora, and fauna) but also on people and infrastructures. Direct and indirect damage to property and human settlements, as well as many casualties all over the world are unfortunately consequences of landslide events. Hence, the prediction and modeling of such events is of high interest to scholars aiming at understanding both the triggering mechanism and the post-failure dynamics, either by empirical or physically-based approaches.

The present thesis addresses this key problem by identifying innovative approaches to one of the most key aspects of landslide hazard assessments, namely the spatio-temporal prediction of landslide occurrence. In particular, the main goals of the work can be summarized as follows: *i*) the improvement of performances of empirical rainfall thresholds through the integration of the reanalysis soil moisture information within a hydro-meteorological framework; *ii*) the improvement of the spatial prediction of landslides through physically-based models, with a special focus on the real advantages and disadvantages of 1D vs. 3D slope stability analysis at the catchment scale; *iii*) the analysis of the post-failure dynamics of a rainfall-induced fast shallow landslide as well as the influence of the geotechnical and rheological parameters on the front celerity and the impact force of the sliding mass.

Concerning the first research goal, the investigation regarding the definition of a hydro-meteorological threshold (using ERA5 Land Reanalysis soil moisture and rainfall information), revealed that significant improvements of performance can be obtained, respect to the traditional approach based on the rainfall intensity-duration thresholds. Still, margins of improvement remain, as the quality and reliability of input data affects the performance of the prediction.

With regards to the second topic, we compare the 1D (TRIGRS) and 3D (SCOOPS

3D) slope stability models. We find that overall, the 3D approach gives better results than the 1D method in terms of model performance, demonstrating that the 3D approach is able to better describe the landslide triggering mechanisms through the assumption of more realistic slip surface geometries. In particular, thanks to the use of the multi-objective optimization to set a more reliable model parameterization, a greater gain of performance is obtained moving from the 1D to the 3D simulation, in comparison to other literature studies, where no optimization has been applied.

Finally, concerning the analysis of the post-failure dynamics, the code SPHERA v.9.0.0 (RSE SpA), a free research software (FOSS) based on the SPH ("Smoothed Particle Hydrodynamics") method, is used (Amicarelli et al. 2020b). Indeed, SPHERA include a scheme for dense granular flows (Amicarelli et al. 2017) that can be applied to simulate fast landslides undergoing large deformation and behaving like dense granular flows. SPHERA has been validated on a rainfall induced fast shallow landslide; a rough estimate has been provided of the impact force exerted by the leading edge of the earth-flow on the downstream structures. More specifically, the effects of both maximum viscosity and limiting viscosity are inspected, to explore the trade-off between computational time and accuracy. Then, the final landslide profile after the deposition is compared with available survey data for model validation and, finally, the influence of geotechnical input parameters on landslides front celerity and impact force is analyzed. Overall, good model accuracy is found and obtained results are consistent with the theoretical expectations.

Overall, the findings of the thesis can be useful for improving the spatio-temporal prediction of rainfall-induced landslides, which can be an aid in landslide risk mitigation.

Keywords

Rainfall-induced landslides; triggering; propagation; soil moisture; thresholds; 1D model; 3D model; SPH; reanalysis.

Chapter 1

Introduction

Abstract

In this chapter, a general overview concerning the main research field, namely the modeling and simulation of rainfall-induced landslides, is reported with the aim to clarify how each covered issue was investigated and the common thread running through all explored aspects of the present thesis.

The aims of the research are, then, specifically reported together with the outline of the dissertation.

1.1 Overview

Landslides represent a critical natural hazard in many mountain and hilly regions worldwide, provoking casualties and property damages. Natural disasters contribute to slope failures, e.g., see earthquakes, volcanoes, floods, anthropogenic factors, and, above all, extreme rainfall which plays a key role in the landslide initiation mechanism, since water infiltration is responsible for decreasing resisting forces acting on the slope. Therefore, in order to reduce the landslide hazard, accurate prediction of landslide occurrences, and monitoring and early warning systems constitute vitally important tools that need to be developed and improved.

Since landslides hazards have considerable spatial implications related to the initiation of the hazard and the areas affected by landslides (van Westen et al., 2008), landslide initiation analysis and runout modeling are the essential components of hazard assessment (Chae et al., 2017).

As a result, many efforts have been devoted to the development of techniques and methodologies useful for the space-time prediction of rainfall-induced landslides. Besides the prediction of this kind of phenomenon in terms of slope stability analysis, the appropriate modeling of the interaction between soil and water also plays a crucial role for a reliable prediction of post-failure dynamics. Indeed, the comprehension of the hydrological processes controlling shallow landslides initiation, i.e., the rainfall conditions that trigger landslides, is important in landslide risk mitigation both because it constitutes a condition to develop early warning models able to give warnings about the potential triggering of landslides in an area, and because it enables the mapping of landslide hazard at the catchment scale.

Models for determining the rainfall conditions that trigger landslides can be broadly divided into two categories, namely empirical and physically-based models. The former are defined as the triggering conditions above which, when

reached or exceeded, landslides are expected. Traditionally, landslide triggering thresholds are expressed in terms of not more than two or three precipitation variables, mostly rainfall event depth, and duration and are derived according to historical data of rainfall characteristics and landslide occurrences. The most widely-adopted curves are derived as lower bound curves assuming a power-law form like the following, $I = \alpha D^\beta$, where D is the rainfall duration, and I is the mean rainfall intensity given by the ratio between cumulative rainfall and the considered time interval. The latter simulate the hydrological and geotechnical processes responsible for the trigger and are composed of a hydrological model to determine the soil response to rainfall in terms of pore pressure changes, and a slope stability model to estimate the induced change in the ratio of resisting to driving forces acting on potential sliding masses. The propensity to adopt the empirical approach or the physically-based one is mostly based on the data availability for the area of interest, namely the rainfall time series, the observed landslide occurrences inventory, and the geomechanical soil parameters. A limitation of the empirical methods, for instance, is that records of landslides and triggering rainfall events are necessarily required, so, in the regions where these datasets are not available, process-based methods could be adopted (Marin, 2020). However, it has to be recognized that empirical models may be more useful (e.g., as early warning system) due to the little information on hillslope hydraulic and geotechnical properties that they in principle require, and for their easy application, even if they do not provide information on the magnitude and the locations of the landslide initiation. Physically-based models, instead, can be implemented at the catchment scale and, although they are highly expensive from a computational point of view and require several physical parameters as input, yet they are potentially able to take into account different additional factors predisposing landslide triggering, as well as provide a probabilistic assessment of landslide risk mapping.

Over the last decades, the attempt to implement both empirical and physically-based models using the antecedent soil wetness conditions to account for more

complex hydrological conditions is becoming increasingly promising (Rosi et al., 2021; Wicki et al., 2020; Ponziani et al., 2012; Abraham et al., 2021; Bezak et al., 2021; Zhao et al., 2019a). This led to a recent approach that relies not only on rainfall but, also, on subsurface hydrological measurements (e.g., soil moisture content) defining, with regard to the empirical models, the concept of hydro-meteorological threshold (Bogaard and Greco, 2018; Mirus et al., 2018b, 2018a; Segoni et al., 2018c; Thomas et al., 2018; Wicki et al., 2020), which may be better represent the cause-trigger concept. The term hydro-meteorological is explanatory of the fact that these types of thresholds combine a meteorological variable (rainfall depth) with a hydrological one, reflecting the water storage at the catchment or local scale (Gain et al., 2021).

On the side of the post-failure dynamics, when a potential source of landslide is identified, a runout analysis is crucial as part of a hazard assessment (Aaron et al., 2019), with the aim to estimate land-slide travel distances, flow depths, and velocities. A variety of numerical models have been proposed to simulate the motion of flow-like landslides ranging from simple empirical-statistical methods that rely on statistical geometric correlations to advanced three-dimensional analytical methods that rely on process-based modeling (McDougall, 2017).

Numerical models, including both continuum and discontinuum models, fall into the second category. Within this subcategory, hybrid “semi-empirical” numerical models that rely on parameter calibration are more common than pure mechanistic models that rely on independent material property estimates. The most practical empirical methods are based on simple geometric correlations such as the correlation between landslide volume and the angle of reach (i.e., the angle of the line connecting the crest of the source with the toe of the deposit) (Scheidegger 1973; Li 1983; Nicoletti and Sorriso-Valvo 1991; Corominas 1996; Hunter and Fell 2003), or the correlation between landslide volume and the area covered by the deposit (Li 1983; Hungr 1990; Iverson et al. 1998; Griswold 2004). Thus, statistical results can be used to establish limits of confidence for prediction

that can then be used for quantitative risk assessment. On the other hand, numerical models seem able to simulate the flow-like landslide behavior and can be used for runout prediction and hazard zonation. However, these models depend on the appropriate calibration of the input parameters to the model, which turns out to be difficult when only geometrical information is available and the boundary conditions are complex or not completely known (Crosta et al., 2003).

1.2 Aim of the research

The main aim of the present thesis is to improve the modeling and simulation of rainfall-induced landslides investigating both prediction and post-failure dynamics. Since a variety of models exist for simulating these phenomena, it is important to assess these models and reduce their uncertainties.

In particular, the research is focused on the following specific objectives:

- i. Integration of soil moisture data in rainfall-induced landslides modeling to improve the predictive performance;
- ii. Investigation of the potential rainfall-induced landslide modeling improvements using 3D slope stability analysis and optimization algorithms at the catchment scale;
- iii. Post-failure dynamics to provide a more reliable representation of the landslide dynamics and impact force.

1.3 Outline of the dissertation

The present thesis is structured in the form of a paper-based thesis and comprises the collection of the inter-related articles produced over the Ph.D. course.

Overall, the dissertation is divided into seven chapters, including the present introduction.

Chapter 2 presents an overview of the literature review concerning the main addressed themes covered in this thesis, namely the principal methods for modeling and simulation of rainfall-induced landslides. Specifically, given the thesis' structure, which consists of a succession of articles in the following

chapters, an inevitable overlapping between the introductions presented in these latter chapters and that presented in the literature review chapter can occur.

Chapter 3 gives an overview concerning the main hydraulic soil parameters together with soil moisture information, with particular attention to the reanalysis soil moisture dataset.

Chapters from 4 to 6 correspond to the research developed concerning each specific objective mentioned in the previous section and published in international journal or in preparation. In more detail, they are listed below.

Chapter 4 presents the study concerning the integration of soil moisture data for the identification of hydro-meteorological thresholds to improve their predictive performance. The article addressing that issue is in preparation at the present moment and it is presented as follow:

Identification of regional landslide triggering thresholds using multivariate statistical analysis and reanalysis soil moisture

Palazzolo, N.; Peres, D.J.; Creaco, E.; Cancelliere, A.

Chapter 5 presents the study concerning the investigation of the potential rainfall-induced landslide modeling improvements using 3D slope stability analysis and optimization algorithms at the catchment scale. The article addressing that issue is published as follow:

Improving Spatial Landslide Prediction with 3D Slope Stability Analysis and Genetic Algorithm Optimization: Application to the Oltrepò Pavese

Palazzolo, N., Peres, D.J., Bordoni, M., Meisina, C.; Creaco, E.; Cancelliere, A. (2021) *Water*, 2021, 13, 801.

Chapter 6 presents the study concerning the analysis of the post-failure dynamics to provide a more reliable representation of the landslide dynamics and impact force. The article addressing that issue is published as follow:

Post-failure dynamics of rainfall-induced landslide in Oltrepò Pavese

Manenti, S.; Amicarelli, A.; Palazzolo, N.; Bordoni, M.; Creaco, E.; Meisina, C. (2020) *Water*, 2020, 12.

General conclusions and future developments are delineated in *Chapter 7*.

Chapter 2

Literature review

Abstract

This chapter aims to present a comprehensive picture of the state of art of methods and models for the prediction of shallow landslides, particularly shallow landslides induced by rainfall.

After an initial framework concerning the main features of landslide phenomena and their correlation with extreme rainfall events, the present chapter focuses on the prediction models recognized by the scientific literature.

Models for determining the rainfall conditions that trigger landslides can be broadly divided into two categories, namely rainfall triggering thresholds and numerical physically based models.

The fundamentals of both approaches will be elucidated in the following sections.

2.1 Landslides triggered by rainfall

Landslides play a significant contribution in the evolution of the landscape, and constitute a high-priority natural hazard in many mountain and hilly regions worldwide causing human casualties and property damages.

Although the use of the general term “landslide” for all types of mass-transport deposits has created quite a few conceptual and nomenclatural issues (Shanmugam and Wang, 2015), that term is widely adopted to denote a broad range of ground movements, including rock-falls, deep failure of slopes, and shallow debris flows, occurring, under the influence of gravity, on the surface of rupture in which much of the material often moves as a coherent or semicoherent mass with little internal deformation (Highland and Bobrowsky, 2008).

The landslide classification system also is a relevant matter. Indeed, over the last few decades, many landslide classification systems have been developed and proposed (Li and Mo, 2019), however, the system of landslide classification devised by D.J. Varnes (Varnes, 1978; Cruden and Varnes, 1996) has become the most widely used system worldwide (Chacón et al., 2006).

According to Varnes (Varnes, 1978), the type of movement and the type of the material involved are the features upon which the landslide categorization is based. In brief, material in a landslide mass is either rock or soil (or both); the latter is recognized as earth if mainly composed of sand-sized or finer particles and debris if composed of coarser fragments (Highland and Bobrowsky, 2008).

At the same time, in relation to the internal mechanics of how the landslide mass is displaced, there are five kinematically distinct categories of landslide, namely fall, topple, slide, spread, or flow. It seems clear that every landslide can be described through the use of the combination of two terms that easily remind respectively material and movement (that is, rockfall, debris flow, and so on). Figure 2.1 shows some types of common landslides classified according to the Varnes categorization.

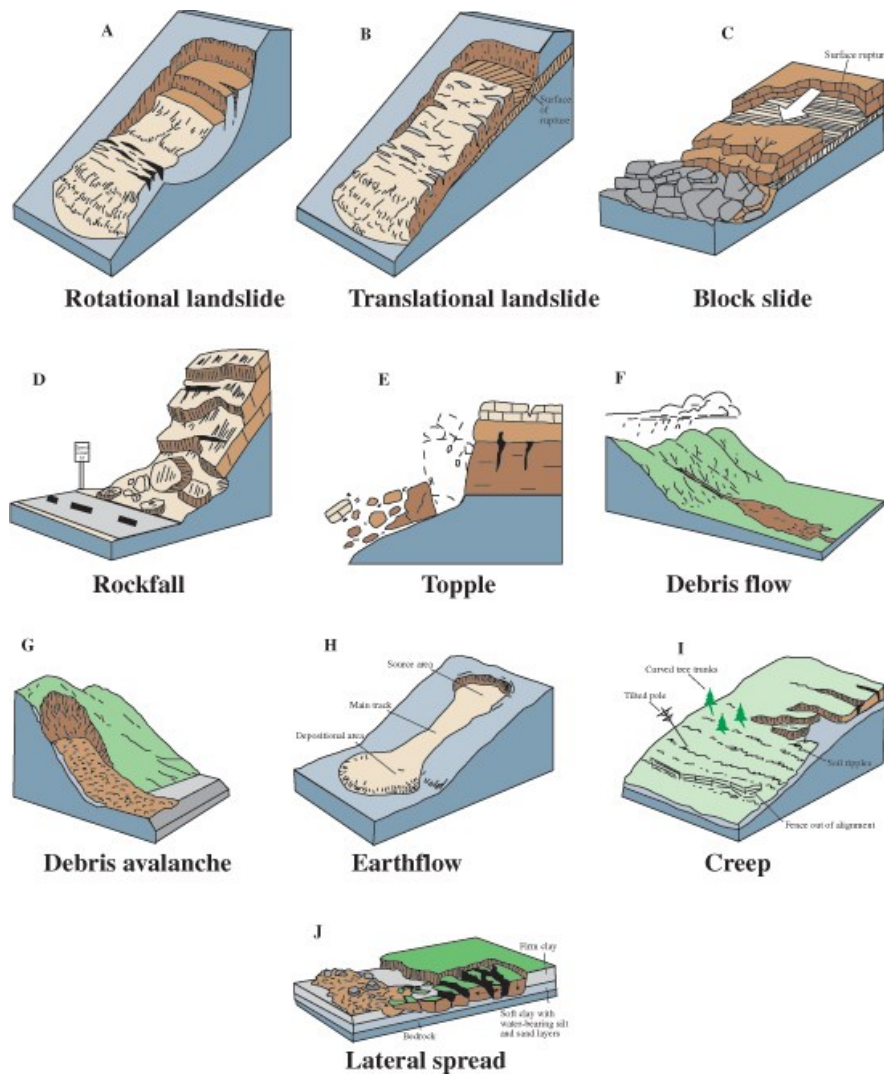


Figure 2.1 Simple illustration representing some common landslide types (Highland and Bobrowsky, 2008)

Every landslide is caused by disturbances in the natural stability of a slope that increase the effect of down-slope forces, thus reducing the strength of its earth materials. To be more accurate, it is more appropriate to discuss causal factors than real causes. Let us begin, for instance, with the ground conditions (weak strength, sensitive fabric, degree of weathering and fracturing), they are influential criteria but are not causes (Popescu, 1994). To these factors, environmental criteria of stress, natural or anthropogenic processes must be

added since they effectively change the static ground conditions sufficiently to cause the slope system to fail (Popescu 1984).

In view of these considerations, although there are multiple types of causes of landslides, the three most common triggering mechanism of landslides around the world are the seismic and volcanic activities and the water (Von Huene et al., 2016; Reshad Md. Ekram Ali et al., 2016). The latter case is the issue that will be discussed and deepened in the present dissertation.

What is meant by landslides induced by water is the triggering due to the slope saturation brought on by intense rainfall, snowmelt and, changes in ground-water levels. Indeed, landslides are influenced by piezometric levels, which in turn are a function of various hydrologic variables like rainfall and soil properties (Finlay et al., 1997). In reason of that, the comprehension of the link between rainfall and initiation of landslide is essential (Hong et al., 2005; Guzzetti et al., 2007a, 2008a).

The majority of rainfall-induced landslides are shallow (less than a few meters deep), small and move rapidly. Usually, this type of landslide transforms into debris flows, namely granular masses fast-moving composed of water, soil, and sediments that enter stream channels along down steep slopes.

The most customary assumption is that the landslide body becomes saturated from below when rainfall infiltration starts (Lumb, 1975) and the soil loses its strength, causing shallow seated failure (Zhang et al., 2011). However, slope saturation is not always that simple phenomenon (Polemio and Petrucci, 2000).

A conceptual model representing the initiation mechanism of a rain-induced debris flow in showed by Shen et al. (2018) and reported in Figure 2.2 where three different initiation mechanism are highlighted (transformation from landslide, surface erosion, and dam breaching).

After a slope failure occurs during a rainstorm, the stirred earth material moves into channels transforming into debris flows or landslide dams. At this stage, the

surface runoff may break the landslide dam formed earlier and, simultaneously, it may cause bed erosion initiating some hillslope debris flows (Shen et al., 2018; Chen et al., 2012). The most hazardous scenario takes place when some of the isolate debris flows converge into the main channel of the drainage basin generating a single devastating flow.

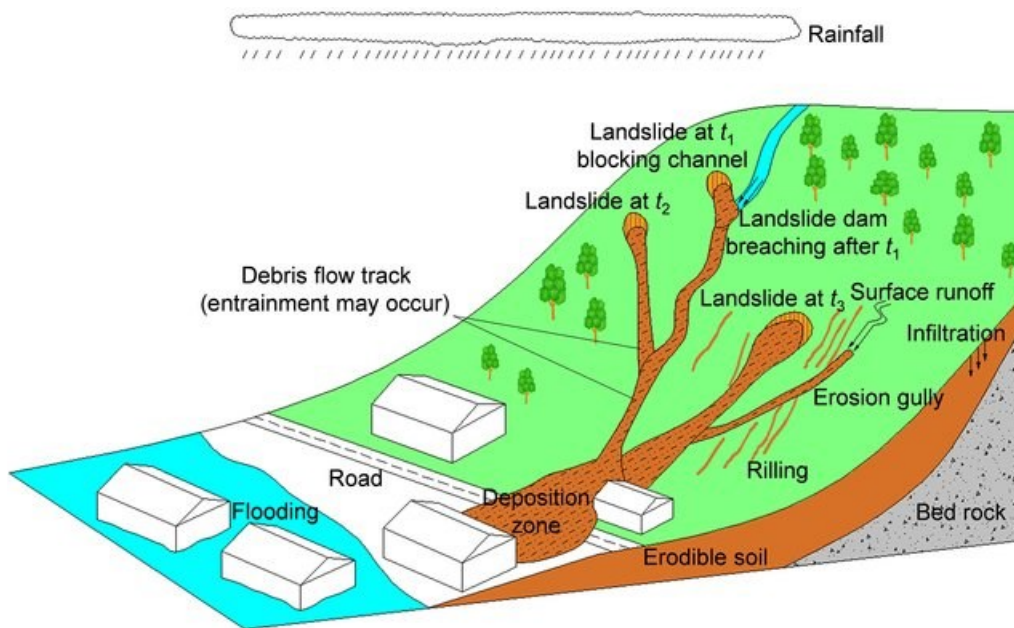


Figure 2.2 Conceptual examples of some typical triggering mechanism of debris flow by Shen et al. (2018)

It is commonly agreed that the hydraulic response to rainfall for a homogeneous infinite slope consists of two phases that are the infiltration process and the groundwater rising. The first one is nothing else than the propagation of the wetting front, while the second one starts after the rainwater infiltrates and reaches the deep soil-bedrock interface (Ran et al., 2018a; Li et al., 2013).

The groundwater rising is certainly a gradual process over time. Due to the extremely low saturation of bedrock, the groundwater table may rise slowly during the rainfall event or always stay in the bedrock. The fact remains that, during that time frame, the interface soil-bedrock, having two different saturated hydrologic conductivity, gives out a place for water accumulation in unsaturated

conditions and a shallow landslide may occur at exactly that moment (Ran et al., 2018b). Added to this are the loss of matric suction above the bottom of the wetting front and the increasing positive pore water pressure (Collins and Znidarcic, 2004; Ng et al., 2001; Rahardjo et al., 2007; Cho and Lee, 2002).

In the light of the above considerations, it is comprehensible how the rainfall characteristics, such as intensity and duration, are equally impactful as well the diverse geotechnical and geomechanical soil properties and that is the reason why many efforts have been devoted to the development of techniques and methodologies useful for determining the rainfall conditions that are more likely to trigger shallow landslides.

2.2 Empirical models

As set out in the previous section, rainfall is one of the primary trigger of landslides, and the prediction of rainfall-induced landslides relies largely on the definition of rainfall thresholds, which are the rainfall conditions the exceedance of which is likely to trigger landslide (Segoni et al., 2018a; Piciullo et al., 2018; Bordoni et al., 2019; Caine, 1980; Guzzetti et al., 2008b, 2007b; Aleotti, 2004a). Usually, rainfall thresholds are defined on empirical (historical, statistical) bases even if, due to the empirical nature of this approach (Cannon et al., 2008; Dahal and Hasegawa, 2008; Giannecchini et al., 2012; Leonarduzzi et al., 2017a; Peruccacci et al., 2012a), the quality and reliability of input data can affect the reliability of the prediction (Hong et al., 2006; Nikolopoulos et al., 2014a; Peres et al., 2018; Marra, 2019).

In literature, rainfall thresholds are usually grouped in three broad categories according to the variables used for their definition: (1) thresholds that combine precipitation measurements referred to a certain rainfall event; (2) thresholds defined according to the antecedent conditions (Terlien, 1998; Crozier, 1999; Glade et al., 2000; Aleotti, 2004a; Abraham et al., 2021); and (3) other thresholds

like as the hydrological ones (Reichenbach et al., 1998; Jakob and Weatherly, 2003; Zhao et al., 2019b).

Within the wide category of the thresholds established using precipitation measurements from individual or multiple rainfall events, a further classification includes: (i) intensity-duration thresholds (ID); (ii) thresholds based on the total event rainfall (E); (iii) rainfall event- duration thresholds (ED), and rainfall event-intensity thresholds (EI) (Guzzetti et al., 2007a).

In practice, rainfall thresholds are expressed by mathematical laws (e.g., power law, linear or bilinear function) and are usually obtained by drawing lower-bound lines to rainfall conditions that resulted in landslides plotted in Cartesian, semi-logarithmic, or logarithmic which result in curves that delimit a portion of the Cartesian plane containing the hydrological conditions (e.g., rainfall intensity-duration) related to known slope failures.

One of the first groundbreakers in the rainfall threshold field is certainly Neil Caine (Caine, 1980) who attempted to establish a general minimum level below which landslides do not occur, independently of local morphological, lithological properties, and of regional rainfall pattern and history. Caine listed 73 rainfall duration and intensity conditions that have resulted in shallow landslides and debris flows worldwide and, based on this data, proposed a global rainfall intensity-duration (I-D) threshold taking the following form (Eq. 2.1):

$$I = 14.82 \times D^{-0.39} \quad 0.167 < D < 500 \quad (2.1)$$

where D [h] is rainfall duration, and I [mm/h] is rainfall intensity.

Besides Caine (1980), global thresholds have been proposed also by Innes (1983), Clarizia et al., Crosta and Frattini, Cannon and Gartner and by Guzzetti et al. (2007b). Figure 2.3 shows some of these rainfall intensity- duration (ID) thresholds referred to some cases studies (Guzzetti et al., 2007b) and adapted by Bogaard and Greco (2018).

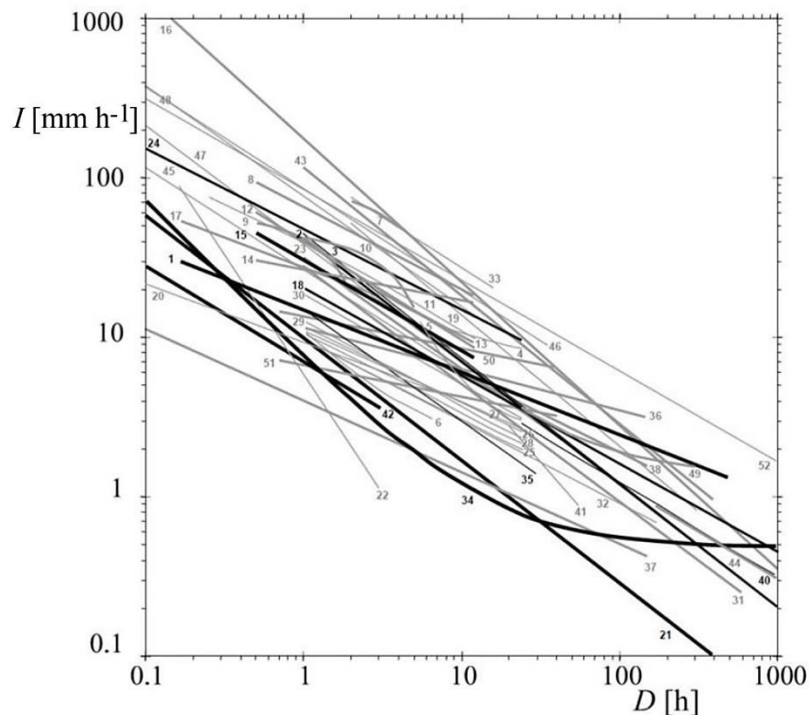


Figure 2.3 Rainfall intensity-duration (ID) thresholds. Numbers refer to case studies investigated by Guzzetti et al. (2007). Very thick lines are global thresholds and thin lines are local thresholds. Black lines are referred to central and eastern Europe, whereas the grey ones are referred to other regions or areas (Bogaard and Greco, 2018).

On the basis of the rainfall conditions that have resulted in landslides at various sites or regions worldwide and, according to similar meteorological, climatic and geomorphological settings, different ID thresholds were proposed at the local, regional, and global scale, over time. Regional and local thresholds may work well enough in the area where they were developed and that is why they may be used as a tool for landslide early warning systems (Papa et al., 2013; Mirus et al., 2018b; Segoni et al., 2018a). Nevertheless, it is not always possible to define a local or regional threshold due to the lack or inconsistency of data, so they could be replaced by global thresholds, which, however, may result in more false positives, namely the predictions of landslides that actually do not occur.

A strategy to overcome the abovementioned limitations and to make different thresholds comparable was the definition of the standardized thresholds. Indeed, within the broad category of the thresholds that use precipitation measurements

for a specific rainfall event, besides the most widespread intensity-duration (ID) threshold, a few authors attempted to establish thresholds for the initiation of landslides based on the total amount of precipitation during the landslide triggering event and defining that amount as a percentage of the mean annual precipitation (MAP). In short, if the total precipitation during a rainfall event exceeds an established percentage of the mean annual precipitation (MAP), slope failures are likely to trigger or to trigger abundantly (Guidicini and Iwasa, 1977). Irrespective of the methodology by which empirical thresholds are established, in general, they have a limit of taking into account only the characteristics of rainfall events that causes landslides. For instance, if the ID and ED thresholds are considered, both rainfall variables do not directly reflect neither the hourly maximum rainfall (Lee et al., 2021) nor the amount of antecedent rainfall that is crucial to the landslide occurrence mechanism due to the increase of pore water pressure and the deterioration of slope stability (Crozier, 1999; Glade et al., 2000; Iverson, 2000b; Segoni et al., 2018b).

As a result, the attempt to define rainfall thresholds based on antecedent rainfall or other proxies to account for more complex hydrological conditions is becoming increasingly interesting (Rosi et al., 2021; Wicki et al., 2020; Ponziani et al., 2012).

In this regard, a recent focus has been given to procedures for landslides prediction that take into consideration the soil moisture information as a hydrological factor responsible for triggering (Zhao et al., 2019c; Abraham et al., 2021; Bezak et al., 2021). These studies highlight how the antecedent volumetric soil water content must be considered as a predisposing initial condition for triggering since different antecedent soil moisture conditions need different rainfall events to trigger landslides. Simply, a dry soil moisture antecedent condition requires a high-intensity rainfall or prolonged rainfall to increase the soil water content and, consequently, to initiate a landslide; while antecedent

conditions close to saturation can trigger landslides even if small rainfall occurs (Zhao et al., 2019b). Thus, it seems clear that to reduce the incorrect prediction (e.g., false alarms and missed alarms), the landslide warning thresholds should be adjusted according to the antecedent soil moisture condition.

2.3 Physically-based models

Physically-based models combine a mechanical model for landslides triggering and a hydrological model for rainwater infiltration. This can provide an insight of triggering processes of shallow landslides at the basin scale, also accounting for the spatial variability of the involved parameters. Indeed, while the empirical approach is extensively used at the regional scales (Aleotti, 2004a; Cannon et al., 2011; Martelloni et al., 2012; Rosi et al., 2012; Lagomarsino et al., 2013), the physically-based one is more applied at slope or catchment scales (Baum et al., 2002; Baum and Godt, 2010; Simoni et al., 2008; Arnone et al., 2011; Salciarini et al., 2017; Park et al., 2013; Montgomery and Dietrich, 1994; Rossi et al., 2013; Pack et al., 2001; Lu and Godt, 2008), in view of the extreme heterogeneity and variability of hydrological and geotechnical parameters at regional scale and the poor knowledge of their spatial distribution (Mercogliano et al., 2013; Tofani et al., 2017). The analysis at the catchment scale, actually, requires a detailed description of the domain for individual landslides, thus the computational burden can become prohibitive if the domain extends over kilometers and the pore water pressure profile needs to be determined with a resolution of centimeters (Balzano et al., 2019). Therefore, physically-based models at the catchment scale are generally simplified to scale down the problem to 2D or 1D conditions, as confirmed by the majority of the slope failure models based on the 1D infinite slope assumption (Simoni et al., 2008; Godt et al., 2008; Aristizábal et al., 2015). Overall, these models require soil properties as input parameters in order to calculate the safety factor on an infinite slope that is involved in the

infiltration process. Such models include LISA (Hammond et al. 1992), SINMAP (Pack et al. 1999), and for transient flow, SHALSTAB (Montgomery and Dietrich, 1994), CHASM (Anderson and Lloyd, 1991), TRIGRS (Iverson, 2000a; Baum et al., 2002) and, SUSHI (Capparelli and Versace, 2014). The latter, specifically, takes into account the temporal and spatial distributions of moisture content in the subsurface, in order to evaluate the different contributions such as the downslope and vertical components of flow in the hillslope caused by unsteady rainfall (Capparelli and Versace, 2014). The factor of safety FS is function of the soil-water pressure and, consequently, the hydrological model allowing the computation of pore pressure from rainfall input, is an essential part of such physically-based models. Indeed, an increase in pressures provides a decrease in the slope stability that is usually expressed as one formula for the safety factor FS , namely the ratio between the shear strength and the shear stress. In accordance with most of the studies, $FS = 1$ is assumed as limiting equilibrium stadium for landslides triggering (Peres et al., 2018; Baum and Godt, 2010; Rosso et al., 2006; Iverson, 2000b; Peres and Cancelliere, 2018b), therefore the failure is predicted when $FS < 1$, and stability holds when $FS \geq 1$. The great majority of landslide models use infinite slope stability analysis (Lepore et al., 2013; Yao et al., 2019a; Salvatici et al., 2018; Zieher et al., 2017a; Raia et al., 2014a; Strauch et al., 2019), according to which landslides are assumed to be infinitely long and with small depth of the potential failure surfaces z_w compared with their length and width, and therefore, these models are most appropriate for the analysis of shallow landslides with planar failure surfaces. Moreover, the infinite slope assumption provides the failure is always located at the bottom of the soil, that represents the connection layer with the underling bedrock (Fig. 2.4).

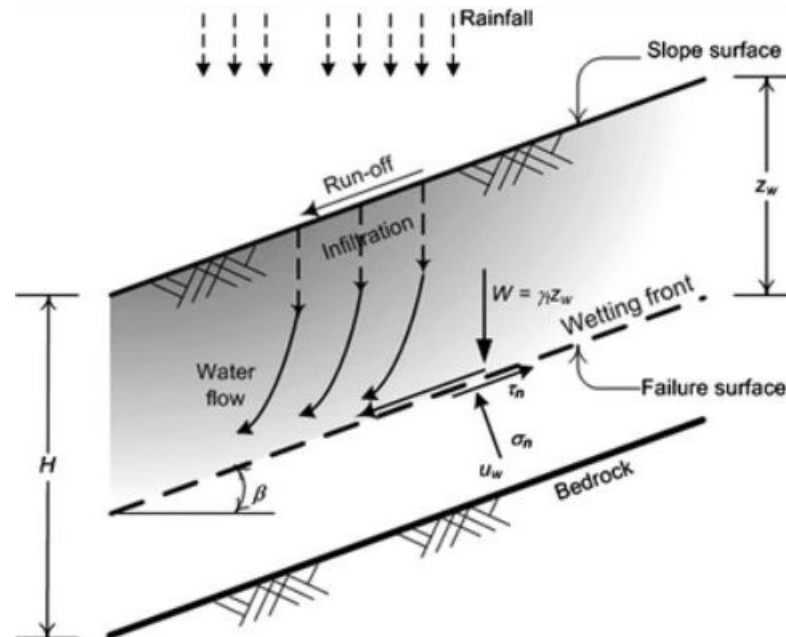


Figure 2.4 Infinite slope model to analyze rain infiltration induced shallow failure (Muntohar and Liao, 2009)

However, if so, the failure of each cell is assumed to be independent of the other ones in the catchment, which are thus quite unrealistic.

Hence, there is an increasing scientific interest towards the development of models that implement three-dimensional slope stability analysis (Milledge et al., 2014; Lu et al., 2014; Bar et al., 2020; Jeremić, 2000).

Almost all the 3D limit equilibrium methods (LEMs) were extended from 2D slice methods. The first 3D slope-stability method to calculate the Factor of Safety (FOS) was given by Anagnosti (1969). A similar procedure of determining the 3D FOS was done by Cheng and Yip (2007). Huang et al., (2002); Hungr (1987); Hungr et al. (1989); Sun et al. (2012); Ugai (1988), also extended the 2D LEMs to develop the 3D methods for determining the FOS. The various 2D LEMs include Fellenius method (1936), simplified Janbu method (Janbu, 1954), Bishop's method (1955), generalized Janbu method (Janbu, 1957), and Morgenstern and Price's method (1965). The assumptions of each of these 3D methods followed the corresponding assumptions of its 2D origin, but the slip surface was assumed different for different slopes. Some researchers assumed it to be a rotational

surface of circular cross-section and some others assumed cylindrical cross-section. The FOS obtained by the 3D methods was found to be higher than the 2D methods (Chakraborty and Goswami, 2016).

SCOOPS 3D (software to analyze 3D slope stability throughout a digital landscape) (Reid et al., 2015) belongs to the 3D models category and uses a three-dimensional (3D) approach to assess the stability of many potential landslides within a user-defined size range and considering landslide triggering as a cascade of failures of interconnected soil columns (Fig. 2.5).

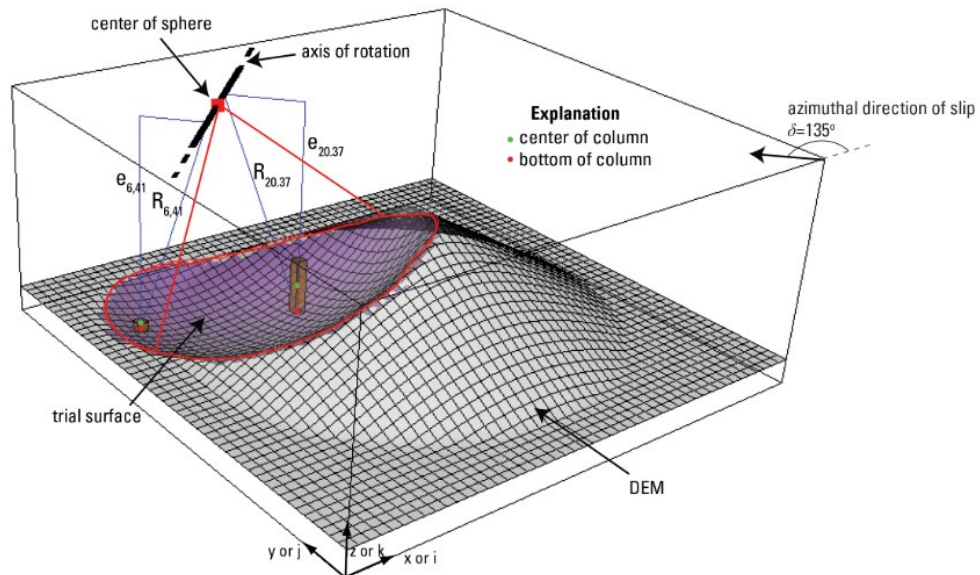


Figure 2.5 Diagram showing a 3D perspective view of a cone-shaped digital elevation model (DEM) and one potential failure (trial) surface. The potential failure mass (removed from this diagram) is composed of an ensemble of columns defined by the DEM grid with the center of the spherical trial surface and the axis of rotation located above the DEM (Reid et al., 2015).

All these methods, broadly, are based on the assumption according to which the failure mass is divided into a number of columns with vertical interfaces and use the conditions for static equilibrium to find the factor of safety. Assumption must be introduced to render the problem statically determined and to facilitate the numerical procedures (Chen et al., 2003).

The selection of the slope stability method, thus, remain a critical issue since the

accuracy of the analysis results mainly depends on the mechanism of the failure. However, even if most of the analysis are performed using 2D slope stability analysis due to its simplicity and lower operational cost, 3D analysis is more reliable to represent the actual geometry condition (Masagus Ahmad Azizi et al, 2020).

2.4 Runout analysis

Landslide runout analysis is used to simulate the movement of past landslides and to predict the motion of potential future landslides. For that reason landslide runout analysis represents a crucial aspect both in landslide risk assessment (Willenberg et al., 2009; Froese et al., 2012; Jakob et al., 2013), and in the design of mitigation structures, especially when it comes to extremely rapid, flow-like landslides occur (Mancarella and Hungr, 2010; Ashwood, 2014).

Run-up heights and impact loads on such structures can be modelled directly or estimated indirectly based on estimated flow depths and velocities at specific points of interest (Hübl et al., 2009; Kwan, 2012).

A variety of numerical models have been proposed to simulate the motion of flow-like landslides ranging from simple empirical-statistical methods that rely on statistical geometric correlations to advanced three-dimensional analytical methods that rely on process-based modeling (McDougall, 2017).

Numerical models, including both continuum and discontinuum models, fall into the second category. Within this subcategory, hybrid “semi-empirical” numerical models that rely on some form of parameter calibration are more common than pure mechanistic models that rely on independent material property estimates. The most practical empirical methods are based on simple geometric correlations such as the correlation between landslide volume and the angle of reach (i.e. the angle of the line connecting the crest of the source with the toe of the deposit) (Scheidegger, 1973; Li Tianchi, 1983; Nicoletti and Sorriso-

Valvo, 1991; Corominas, 1996; Hunter and Fell, 2003), or the correlation between landslide volume and the area covered by the deposit (Li 1983; Hungr 1990; Iverson et al. 1998; Griswold 2004). Thus, statistical results can be used to establish limits of confidence for prediction which can then be used for quantitative risk assessment. On the other hand, numerical models seem able to simulate the flow-like landslide behavior and can be used to the runout prediction and hazard zonation. However, these models depend on the appropriate calibration of the input parameters to the model, which turns out to be difficult when only geometrical information is available and the boundary conditions are complex or not completely known (Crosta et al., 2003). Overall, limited guidance is provided in order to carry out runout analysis, since there are no universal constitutive laws governing landslides that are straightforward to incorporate into numerical models, resulting in more incentives to adopt an empirical approach (Pastor et al., 2012). Besides the issue concerning the optimal approach to adopt for a reliable runout analysis, another debated aspect is related to the mechanisms of long runout behavior, which includes pore pressure response (Iverson, 2012; Hungr and Evans, 2004; Legros, 2006; Iverson et al., 2011), but could also involve more peculiar aspects, including lubrication by snow or ice (Delaney and Evans, 2014); fluidization by trapped air, vapor or dust (Manzanal et al., 2016); frictional weakening by flash heating (Lucas et al., 2014), and forces generated by dynamic rock fragmentation (Bowman et al., 2012; Davies et al., 2012). All such theories are very challenging to test since the physical properties involved in the process are very hard to measure at the field scale and, consequently, they are arduous to replicate within the analysis. If numerical approach is considered, more recent advances are attempting to use meshless methods, such as the Smoothed Particle Hydrodynamics (SPH) method, as a more natural way of modeling the propagation stage of landslides in a consistent manner (Manenti et al., 2016; Pastor et al., 2014) . This is because SPH

method is a mesh-free, Lagrangian particle method, which gives better performance than conventional numerical methods in treating free surfaces, moving interfaces, and large deformations (Hu et al., 2015). In that context, the code SPHERA v.9.0.0 (RSE SpA), a free research software (FOSS) based on the SPH (“Smoothed Particle Hydrodynamics”) method which represents a mesh-less Computational Fluid Dynamics technique for free surface and multi-phase flows, seems to be promising (Amicarelli et al. 2020b). Indeed, SPHERA include a scheme for dense granular flows (Amicarelli et al. 2017) that can be applied to simulate fast landslides undergoing large deformation and behaving like dense granular flows.

Chapter 3

Soil moisture information for improving landslide prediction

Abstract

This chapter aims to give an overview concerning soil moisture information since it represents one of the predisposing factors in the initiation of landslide mechanisms, and it can be a useful source for improving landslide prediction. After a general background regarding the main soil hydraulic properties influencing landslides, particular attention is given to the soil moisture measure, and especially to the reanalysis soil moisture dataset. Indeed, just such data are used in the last part of the study conducted in the present thesis. In more detail, the ERA5-Land reanalysis dataset is described together with the motivations that led to its use.

3.1. Main hydraulic soil factors influencing landslides

Soil hydraulic and geotechnical properties exert a major control on landslide initiation. As soils make up the upper part of the unsaturated zone, they are subjected to fluctuations in water and, precisely the unsaturated zone can be considered as the most dynamic region of the subsurface, as changes occur at increasingly smaller time and spatial scales when moving from the groundwater toward the soil surface (Hopmans, 2011). The relative rates of the processes spatially and temporally involving this region, determine the transient level of groundwater in different portions of the hillslope and thus the potential for slope failure during rainstorms, snowmelt, or prolonged periods of water accretion. The most important physical properties of soils that affect slope stability are those that govern the rate of water movement into and through the hillslope, as well as the water holding capacity. Thus, knowledge of these soil hydraulic properties is of key importance for simulation and modeling of subsurface water movement. Some of the main soil hydraulic properties are summarized and briefly explained in Table 3-I.

Table 3- I Main soil hydraulic properties (Indoria et al., 2020)

Soil Hydraulic Property	Description
Infiltration (I)	The infiltration rate is defined as the time rate at which water percolates into the soil or quantitatively as the volume of water entering the soil per unit area in time
Saturated hydraulic conductivity (K_{sat})	Saturated hydraulic conductivity is a quantitative measure of a saturated soil's ability to transmit water when subjected to a hydraulic gradient. It can be thought of as the ease with which pores of a saturated soil permit water movement
Soil water retention	Soil water retention is the ability of a soil to retain water within soil pores when exposed to various pressure and/or suction that occur within the soil profile

Defining θ the volumetric water content as the degree of saturation S ranging between zero (dry soil) and the saturated water content (θ_s) (which is equal to the porosity if the soil were completely saturated), the soil water retention function determines the relation between the volume of water retained by the soil, expressed by θ , and the matric suction forces of soil, namely the difference between pore air pressures and pore-water pressure (Dane and Hopmans, 2002). These suction forces, also known as the soil water characteristic function, describe the increase of θ and the size of water filled pores with an increase in matric forces. Therefore, since matric forces are regulated by pore-size distribution, specific surface area, and interactions at the solid liquid interfaces, the soil water retention curve is very soil specific and highly non-linear. It has been found and described by Haines (1930) that the volumetric moisture content in soil in relation with a particular suction or tension force is different depending upon the soil is wetting or the soil is drying and termed as *hysteresis*. This implies that some soil may have different water contents at the same suction value in the wetting and drying process. The reliability in the determination of the soil water retention curve is of great interest in the field of unsaturated soils, since it related to significant change in the unsaturated coefficient of permeability, shear strength of soils and particle size distribution curve (Nasta et al., 2009). Overall, several laboratory and field techniques to measure the soil retention curve are available, such as the Van Genuchten (1980) and Brooks and Corey (1964) models, described by Kosugi et al., (2002). Figure 3.1 shows an example of measured and fitted soil retention data for two different soils (Tuli and Hopmans, 2004).

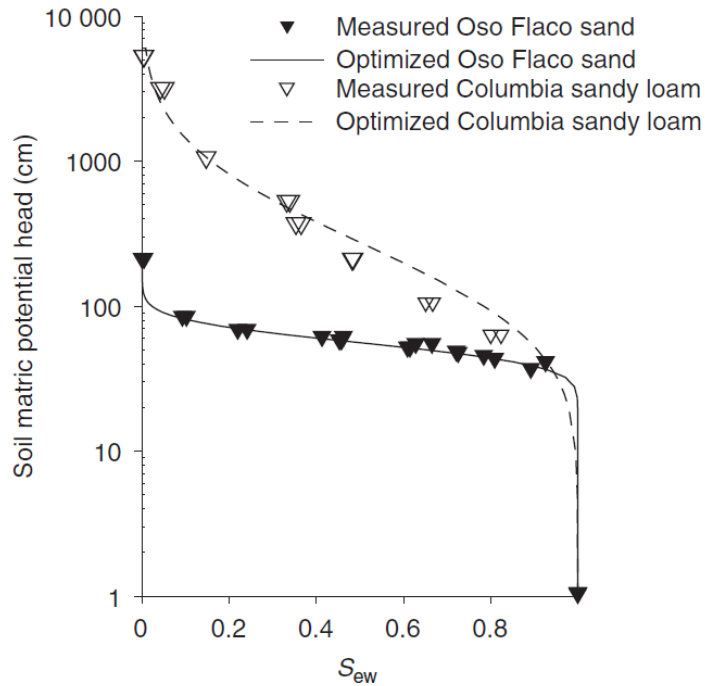


Figure 3.1 Soil-water retention data and optimized curves for the Oso Flaco fine sand and Columbia sandy loam soil (Tuli and Hopmans, 2004).

The second fundamental soil hydraulic property characterizing the unsaturated soil water flow, at the micro-scale, is the hydraulic conductivity K , which can be thought of, in physical terms, as the ease with which fluids may flow through porous media. It is defined by the Darcy–Buckingham equation, which relates the soil water flux density to the total driving force for flow, with K being the proportionality factor. The value of K varies non-linearly with volumetric moisture content for a wide range of soil textures, from near zero for dry conditions to a maximum at saturation (K_{sat}). Models aimed at estimation for unsaturated hydraulic conductivity are based on pore-size distribution, pore geometry, and connectivity, and require integration of soil water retention functions, by means which analytical expressions for the unsaturated hydraulic conductivity can be obtained. The experimental determination of unsaturated hydraulic conductivity is elaborate and time consuming (Ramli et al., 2021). A variety of methods are described in Dane and Topp (2020), and, among these, the

Gardner (1950) numerical model can be considered one of the most established. Gardner's method was the first analytical method of calculating the hydraulic conductivity of unsaturated porous media based on the measurement of transient outflow under suction step in the pressure plate apparatus (Stanic et al., 2020). In light of this brief excursus, it is clear how the hydraulic soil conductivity has a strong influence also on the infiltration rate, i.e., the actual flux of water into the soil. Indeed, the infiltration rate tends to asymptotically approach the saturated hydraulic conductivity (the maximum water transmission rate of the soil) after long periods of infiltration, though entrapped air in the soil never results in perfectly saturated flow in the vadose zone. As for the previous hydraulic soil properties, even for the infiltration process several quantitative descriptions exist. However, the relation proposed by Horton (1931) remains one of the original empirical descriptions widely used, due to its simplicity and ease application:

$$f = f_c + (f_0 - f_c)e^{-kt} \quad (3.1)$$

where f is the infiltration capacity at time t , f_c is the infiltration capacity at $t \rightarrow \infty$, f_0 is the infiltration capacity at $t \rightarrow 0$, k is an empirical constant that attempts to capture the combined influences of all the physical and site properties including changes in micro-pores as the soil becomes wetter, and t is the time from the beginning of rainstorm. Therefore, the infiltration capacity exponentially decreases due to wetting conditions occasioned by the storm onset and, given that it is of key importance for the hillslope hydrology, it is challenging to directly relate infiltration characteristics to slope stability (Sidle and Ochiai, 2006). Indeed, while at the micro-scale reducing recharge into sub-soil should stabilize hillslopes by reducing the increasing pore pressure during a storm, it occurs that much unstable terrains are characterized by tension cracks, especially close to potential triggering zones (Julian and Anthony, 1996), thus providing

preferential pathways for any overland flow that that does not infiltrate into the soil (Sidle and Ochiai, 2006).

3.2. In situ soil moisture measurements

Generally, soil moisture is defined as the water that is held in the spaces between soil particles. When it is referred to the upper 10 cm of soil, we talk about surface soil moisture, whereas the root zone soil moisture is considered to be in the upper 200 cm of soil. Compared to other components of the hydrologic cycle, the volume of soil moisture is small; nonetheless, it is of fundamental importance to many hydrological, and not only, processes since it is valuable to wide range of government agencies and private companies concerned with weather and climate, flood control, soil erosion and slope failure (Ahmad and Bastiaanssen, 2003; Vischel et al., 2008; Mattia et al., 2009; Kong et al., 2011). The high spatial and temporal variability of soil moisture caused by the heterogeneity of soil texture, topography, vegetation, and climate in the natural environment makes soil moisture difficult to measure (Kong et al., 2011). Indeed, even though it is widely recognized the importance of soil moisture data availability, widespread and constant quantifications of soil moisture is negligible and there is still a deficiency of conclusive methods of soil moisture measurements worldwide (Zwartendijk et al., 2017). The standard method of soil water content measurement requires that a physical soil sample is weighted before and after being heated inside an oven. The mass of lost water during the drying process represents a direct measure of the soil water content θ_v [m^3/m^3]. However, even though direct measurement of soil water content is time consuming, inconvenient, costly and often destructive of a field study area, this method is able to provide accurate and reliable measures and represents the standard method according which all others are compared and calibrated (Busscher, 2009). Several alternatives were investigated over time with the aim to measure the soil water content and to avoid the drawbacks due to the direct sampling, also to

make it possible to obtain continuous series of soil moisture measurements over time. For this reason, indirect measurement methods have been devised, such as sensors that respond to surrogate soil properties (e.g., electromagnetic properties) that can be read automatically and are less destructive of field. In this regard, the TDR (Time Domain Reflectometer) sensors measure the soil water content based on the travel time of high frequency electromagnetic pulse through the soil that is used to estimate the permittivity (dielectric constant) of the material. The TDR probes are inserted directly into the soil for in situ measurements at the desired soil depth and they can be attached to a data logger for ongoing measurements. As shown by Topp et al. (1980), an easy relationship for conversion of dielectric water constant to volumetric water content can be applied and it is independent of soil texture, porosity, and salt content. A summarizing table reporting the surrogate measures used by different θ_v sensors is reported in the follow.

Table 3-II Surrogate measures used by different θ_v sensors (Busscher, 2009)

Method	Surrogate Measurement	Explanation
Neutron moisture meter	Count of slow neutrons around a source of fast neutrons	A radioactive source emits fast neutrons (5 MeV), which lose energy as they collide with other atoms, in particular hydrogen. The surrogate is the concentration of slow neutrons. Since the only rapidly changing source of hydrogen in the soil is water, θ_v can be calibrated vs. the count of slow neutrons.
Thermal sensors	Heat conductivity or heat capacity of the soil	A pulse of heat is generated and the subsequent rise or fall in temperature of adjacent soil is measured over time. Soil is a poor conductor of heat, and water a good one, so the amount of heat or rate of heat transmission is closely related to θ_v .

Table 3-II (continue) Surrogate measures used by different θ_v sensors (Busscher, 2009)

Method	Surrogate Measurement	Explanation
Time domain reflectometer (TDR)	Travel time of an electromagnetic pulse	A fast rise time electromagnetic pulse is injected into a waveguide inserted into or buried in the soil. The time required for the pulse to travel along the metal rods of the waveguide is determined by the bulk electrical permittivity of the soil. The θ_v is a major factor influencing the bulk permittivity (BEC). True TDR involves capture of a waveform and analysis to find the travel time of the highest frequency part of the pulse.
Campbell FDR	Repetition time for a fast rise time electromagnetic pulse	See TDR sensors; same, except reliance on reflected pulse reaching a set voltage rather than waveform analysis causes the method to be more influenced by BEC and temperature.
Capacitive sensors	Frequency of an oscillating circuit	which is a capacitor that is arranged so that the soil becomes part of the dielectric medium affected by the electromagnetic field between the capacitor's electrodes. The θ_v influences the electrical permittivity of the soil, which in turn affects the capacitance, causing the frequency of oscillation to shift.
Conductivity sensors (e.g., granular matrix sensors and gypsum blocks)	Electrical conductivity of a porous medium in contact with the soil	An alternating current voltage is placed on two electrodes in a porous material in contact with the soil, and the amount of current is a measure of the conductivity and amount of water in the porous material between the electrodes. These are used for estimation of soil water tension (suction), not θ_v .
Tensiometers	Matric and gravitational soil water potential components	Capillary forces retaining water in the soil pores are connected through the soil water to water in a porous cup connected to a tube filled with water. This generates a negative pressure within the tube, which can be measured with a vacuum gauge.

In light of that brief background and recognizing that a need exists for continuous measurements of surface soil moisture with global coverage, innovative measurement approaches are increasingly starting to catch on, namely the remote sensing of soil moisture and the reanalysis models. These aspects will be deepened in the following sections.

3.3. Remote sensing soil moisture data

Research in soil moisture remote sensing began in the mid 1970's shortly after the surge in satellite development. Indeed, soil moisture data can be collected by satellites measuring microwaves reflected or emitted by Earth's surface and the intensity of measured signal depends on the amount of water in soil. As already stated, satellite-derived soil moisture data benefit from the near real-time observational capability at the global scale, but, on the other hand, suffers from the uncertainty associated and the coarse spatial resolution. Indeed, while the ground-based measurements are a source of information, the soil moisture observations at a large spatial scale are limited due to the heterogeneous nature of soil moisture in space and time, as a consequence of different climate, weather, topography, vegetation, and soil type (Crow et al., 2012). Nevertheless, recent research demonstrates that remotely sensed data can be a useful tool to improve landslides prediction models (Stähli et al., 2015; Brocca et al., 2016; Segoni et al., 2018b; Thomas et al., 2019). Provided that satellite soil moisture data have surely a lower accuracy than in situ observations (Al-Yaari et al., 2014), remote sensing soil moisture data achieved a promising level of reliability, as demonstrated in many validation studies comparing satellite data with ground observations and hydrological modeling (Wagner et al., 2013; Peng et al., 2015; Ford and Quiring, 2019). Currently, several microwave- based soil moisture products are available on the global scale. In particular, the Soil Moisture and Ocean Salinity (SMOS) mission (Kerr et al., 2010), and the Soil Moisture Active Passive (SMAP) mission

(Entekhabi et al., 2015), placed in orbit their satellites with the specific aim of measuring soil moisture, whereas other satellites include on board sensors providing soil moisture measurements. That is the case of the Advanced Scatterometer (ASCAT) on satellites MetOp-A and MetOp-B (Wagner et al., 2013), and the Advanced Microwave Scanning Radiometers, on satellites Aqua and Global Change Observation Mission-Water1 (Kawanishi et al., 2003). Besides the mentioned soil moisture products retrieved from a single satellite, there is the ESA CCI (ESA Climate Change Initiative) which provides a merged long-term (40 years) soil moisture dataset as a result of a merging multiple microwave-based soil moisture products (Dorigo et al., 2017; Gruber et al., 2017, 2019) and with the aim to extend the typically short temporal coverage of single-sensor soil moisture products. The ESA CCI Soil Moisture products are distributed every 10 days by the Copernicus Climate Change Service. These recent soil moisture global dataset provide the data at a coarse spatial resolution ranging between 25-50 km (Brocca et al., 2017) but, there are some current and future satellite missions that are able to generate high-resolution (0-1 km) soil moisture products (i.e. ESA Sentinel-1 European Radar Observatory, the Satélite Argentino de Observación COn Microondas (SAOCOM) mission, the NASA-ISRO Synthetic Aperture Radar (NISAR), the Radar Observing System for Europe L (ROSE-L), and the Tandem-L satellites) (Peng et al., 2021), and innovative approaches aiming at the downscaling of coarse-resolution soil moisture products, using proxy observations are under study (Peng et al., 2017; Sabaghy et al., 2018). Nevertheless, a major constraint remains, that is that the soil moisture data provided by satellite is representative only of the upper few centimeters of soil (Collow et al., 2012; Kerr, 2007), hence the question arises whether these data can actually be used or not, to improve landslide hazard analysis. Indeed, shallow landslides are typically 1-2 meters depth (Fiorillo et al., 2001), which is much thicker than the soil depth currently directly measured by remote sensing

techniques (Marino et al., 2020). Overall, there is a growing interest in these microwave-based soil moisture products and the challenge is now to derive more reliable accuracy estimates.

3.4. Reanalysis soil moisture data

How it has been highlighted in previous section, the use of passive and active microwave imagers to observe soil moisture over large scales is surely helpful in understanding the spatial and temporal variability of soil moisture anomalies, but its consistency over space and time is limited to several factors, i.e. the satellite lifetime (approximately 5 years), the low temporal resolution at which data are available (about 2-5 days depending the latitude and satellite orbit), and the vertical resolution since the observation are typically related to the top soil layers (1-5 cm) (Hagan et al., 2020). This encouraged an increasing interest in Land Surface Models (LSMs) accounting for several climate variables (i.e., soil moisture, surface fluxes, and run-off) at a global scale and, more importantly, at a continuous time scale. Essentially, these models are based on mathematical models obtained from an understanding of climate and its regularities (Koster et al., 2009), but the assimilation from both ground and remotely sensed information is recently embedded into LMSs (Han et al., 2015). Existing global climate organizations constantly update their models and systems with the aim to improve understanding and reduce uncertainties of these models, enhancing the quality of the Land Surface Variables (LSVs) involved into land-atmosphere processes. In this context, Land data assimilation systems (LDASs) deserve particular attention as they combine LSMs with satellite observations in order to produce reanalysis of LSVs (Tall et al., 2019). Reanalysis combines past short-range weather forecasts with observations through data assimilation. Earth system data assimilation combines the latest observations with a short-range forecast constrained by previous observations to obtain the best possible estimate of the current state of the Earth system. That estimate, called the analysis, is used

as the initial conditions on which weather forecast are based. The quality of forecast crucially depends on the accuracy of the analysis. If analyses are produced for extend periods reaching back decades, but using one and the same assimilation system, they become a *reanalysis* of past weather and climate (Fig. 3.2).

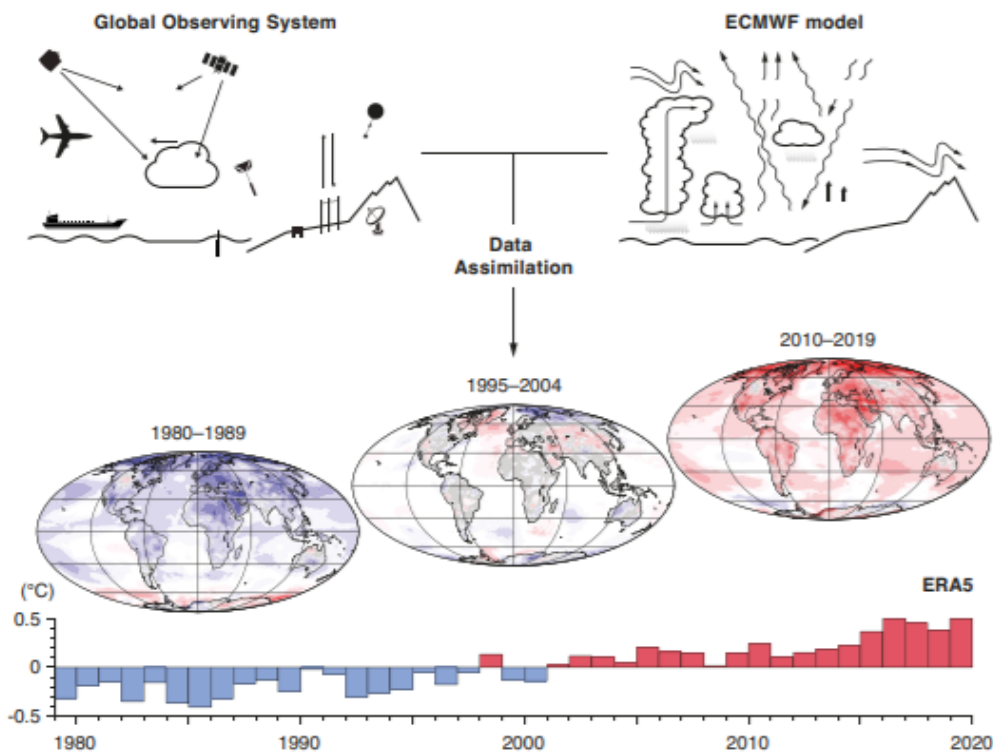


Figure 3.2 Sketch showing how Data Assimilation works to generate reanalysis data (ECMWF model).

To date, reanalysis data provide the most complete picture currently possible of past weather and climate and they are generally freely available on dedicated platforms of the web, released in regular grid formats, with a delay of few months from present (Pelosi et al., 2020). Many advancements have been reached in land surface modeling fields and their applications thanks to the generation of long-term (1979-onwards) global atmospheric reanalysis (Balsamo et al., 2015, 2018). In line with these improvements, NASA's (National Aeronautics and Space Administration) Modern Era Retrospective analysis for Research

Application (Rienecker et al., 2011; Gelaro et al., 2017), and ECMWF's (European Centre for Medium-Range Weather Forecasts) Interim reanalysis (Dee et al., 2011) are the most investigated (Tall et al., 2019), as well as the NCEP/NCAR (National Center for Environmental Prediction/National Center for Atmospheric Research) Reanalysis (Kalnay et al., 1996) Project supported by the National Oceanic and Atmospheric Administration's (NOAA) Office of Global Programs, and the latest reanalysis product from the fifth-generation reanalysis product by the ECMWF (ERA5) (Hersbach et al., 2020). All these reanalysis projects provide soil moisture estimates at different horizontal resolution and at different soil depths as well as at different temporal resolutions and with distinct update frequency. In consideration of the aims pursued in the present dissertation, it was considered more suitable to use the ERA5 fifth-generation reanalysis product by the ECMWF, and in more detail, the ERA5-Land soil moisture dataset. Indeed, in 2019 ERA5 reanalysis data were released, under the auspices of the Copernicus Climate Change Service. ERA5 is the fifth generation of ECMWF global reanalysis, succeeding ERA-Interim and covering the entire globe from 1979 at a spatial resolution of about 31 km. In the same year, Copernicus Climate Change Service has also released ERA5-Land, produced by replaying the land component of the ERA5 climate reanalysis, but with a horizontal resolution of 9 km (Pelosi et al., 2020). An overview of the main characteristics of the ERA products is reported in Table 3-III.

Table 3-III Overview of the main characteristics of ERA-Interim, ERA5, and ERA5-Land (Muñoz-Sabater et al., 2021)

	ERA-Interim	ERA5	ERA5-Land
Period publicly available*	1979–Aug 2019	1950 onwards	1981 onwards (1950–1980, in 2021)
Spatial resolution	79 km/60 levels	31 km/137 levels	9 km
Land surface model	IFS (+ TESSEL)	IFS (+ CHTESSEL)	CHTESSEL
Model cycle (year)	Cy31r2 (2006)	Cy41r2 (2016)	Cy45r1 (2018)
Output frequency	6-hourly (analyses) 3-hourly (forecasts)	Hourly	Hourly
Uncertainty estimate	None	Based on a 10-member 4D-Var ensemble at 63 km	As for ERA5
Availability behind real time	n/a	2–3 months (final product) 5 d (preliminary product)	2–3 months (final product) 5 d (preliminary product, in 2021)

ERA5-Land uses as input to control the simulated land fields ERA5 atmospheric variables, such as air temperature and air humidity. This is called the atmospheric forcing. Without the constraint of the atmospheric forcing, the model-based estimates can rapidly deviate from reality. Therefore, while observations are not directly used in the production of ERA5-Land, they have an indirect influence through the atmospheric forcing used to run the simulation. In addition, the input air temperature, air humidity and pressure used to run ERA5-Land are corrected to account for the altitude difference between the grid of the forcing and the higher resolution grid of ERA5-Land (Muñoz-Sabater et al., 2021). The land surface component of ERA5 and, consequently of ERA5-Land, is the Hydrology Tiled ECMWF Scheme for Surface Exchanges over Land (H-TESSSEL, (Balsamo et al., 2009, 2011). The H-TESSSEL soil model schematizes the vertical movement of liquid water in the soil unsaturated zone relying on the Richards (1931) equation, where a volumetric sink term to simulate root extraction dynamics has been introduced. The required soil hydraulic parameters are stated through the Soil-Water Characteristic Curve (SWCC) using the Van Genuchten (1980) equation. Based on a tiled approach representing different sub-grid surface types for vegetation, bare soil, snow and open water, H-TESSSEL has four soil layers with depths of 7 cm, 28 cm, 100 cm and 289 cm (Zeng et al., 2021), and

provides the output at an hourly scale. Furthermore, hydraulic soil characterization, in HTESEL exploits a soil dataset including soil water characteristic curve (SWCC) and hydraulic conductivity function (HCF) parameters for six soil textures (i.e., coarse, medium, medium-fine, fine, and very fine) (Reder and Rianna, 2021), where the dominant soil texture classes is retrieved from the FAO Digital soil map of the world dataset as soil texture for each grid point (FAO, 2003). Indeed, the surface runoff generation changes according to a variable infiltration capacity based on soil type and local topography (Figure 3.3).

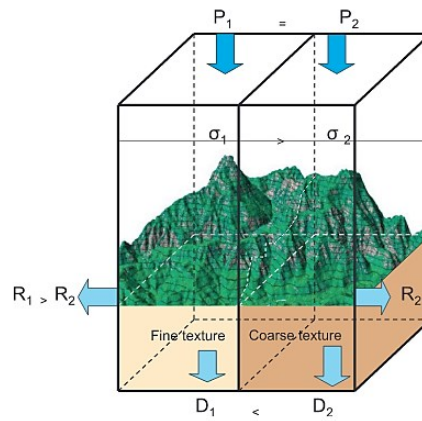


Figure 3.3 Spatial structure added in HTESEL (for a given precipitation $P_1=P_2$ the scheme distributes the water as surface runoff and drainage with functional dependencies on orography and soil texture respectively) (Balsamo et al., 2009) (<https://confluence.ecmwf.int/display/OIFS/>)

In addition to in situ observations, ERA5 is the first ECMWF reanalysis to include remotely sensed observations of soil moisture. It significantly improved the simulations of soil moisture and surface fluxes by using satellite data such as AMI on ERS-1, -2 and MetOp-A/-B ASCAT (Zeng et al., 2021).

Lastly, should be considered that the ERA5 database has been validated with in situ soil moisture networks worldwide (Beck et al., 2021), and that its temporal and spatial resolution, together with the period covered time as well as the fixed grid used for data distribution at any enables an easy access and a more accurate use of information on land states.

Chapter 4

Identification of regional landslide triggering thresholds using multivariate statistical analysis and reanalysis soil moisture data

Palazzolo, N., Peres, D.J., Creaco, E., Cancelliere, A.

Abstract

In recent times several efforts have been addressed to what extent may soil moisture estimations improve the performance of landslide early warning systems (LEWSs). Only few studies quantify the possible improvement of the performance of LEWSs through the identification of hydro-meteorological thresholds, being these systems mainly based on the traditional precipitation thresholds. In this study, we propose a methodology for developing regional hydro-meteorological landslide triggering thresholds coupling mean rainfall intensity and soil moisture information. This last information is derived from the ERA5-Land reanalysis, which provides soil moisture at four depth levels and at the hourly resolution. In order to reduce the dimensionality of the soil moisture information, so to derive 2D thresholds, a Principal Component Analysis (PCA) is performed, which allows minimization of information loss and maximization of the total variance explained by each principal component. Concerning the rainfall data, instead, we tested both observed and ERA5-Land reanalysis hourly data. We then derive thresholds by a multi-step procedure as follows. First, a non-parametric threshold is derived from an optimization procedure based on Artificial Neural Networks (ANN) and maximization of the ROC True Skill Statistic (TSS) index. Then, a parametric equation is used to simplify the non-

parametric threshold derived at the first step. The proposed hydro meteorological thresholds were tested in the Sicily region, prone to landslide risk. Overall, the results show that the triggering thresholds defined as parametric equations of observed rainfall intensity and of the first principal component of soil moisture have better performance compared to the traditional rainfall duration-intensity approach, which has been assumed as a reference case, as the ROC True Skill Statistic increases from 0.50 to 0.67. On the other side, when using reanalysis precipitation, improvements seem not significant. The obtained results represent a step forward to the improvement of landslide threshold identification.

Keywords: ERA5 Land; Hydro-meteorological thresholds; Early warning systems; Sicily; Principal component analysis

4.1. Introduction

The incidence of landslides, usually triggered by heavy rainfalls, is constantly increasing due to landscape modifications, i.e. urbanization, deforestation, land-changes and the abandonment of rural areas (Roccati et al., 2019). Their impact can be really extensive if damages to man-made structures, damages to land, loss of natural resources and loss of life are considered. Furthermore, in the last decades, an increasing number of studies focused on the potential effects of climate change on landslides phenomena (Peres and Cancelliere, 2018b), pointing out that there are a lot of aspects still unclear, such as the abundance, activity, frequency and return period of landslides in response to the projected climate change (Gariano and Guzzetti, 2016; Peres and Cancelliere, 2018b). This implies to a key role of landslide monitoring and warning systems as the principal components of most landslide mitigation measures (Eberhardt et al., 2012). Indeed, after recent catastrophic landslides worldwide, landslide monitoring and especially early warning, have gained enormous interest (Chae et al., 2017; Highland and Bobrowsky, 2008).

Landslides early warning systems (LEWSs) use data generated from previous landslides and rainfall to predict possible slope movements, serving as mitigation tool tackling the severe consequences and damages to properties and population (Roccati et al., 2020). In general, even if landslide early warning systems vary widely in approaches, and scale, empirical rainfall thresholds in combination with rainfall measurements and forecasts remain the most frequently applied approach for the majority of regional LEWSs (Thiebes and Glade, 2016). In the literature, several methods have been proposed aimed to the identification rainfall thresholds to landslides initiation (Guzzetti et al., 2007a, 2008a; Segoni et al., 2018b; Aleotti, 2004b), especially when investigation is focused on the development of early warning systems. Empirical rainfall thresholds are usually obtained by drawing lower-bound lines to the rainfall conditions that resulted in

landslides, plotted in Cartesian, semi-logarithmic, or logarithmic coordinates. When information on rainfall conditions that did not trigger failures is also available, thresholds are determined as the best classifiers of rainfall conditions that resulted and did not result in landslides (Berti et al., 2012; Staley et al., 2013; Peres and Cancelliere, 2014; Postance et al., 2018; Marino et al., 2020; Peres and Cancelliere, 2021). Commonly, these rainfall exceedance thresholds empirically relate the occurrence of landslides to rainfall event characteristics such as intensity, duration, total amounts, or a combination thereof (Wicki et al., 2020). However, in many settings the antecedent soil wetness conditions influence the variability in rainfall triggering amounts, becoming a predisposing factor that plays a major role in landslide initiation (Palau et al., 2021; Conrad et al., 2021). This led to a more recent approach that relies not only on rainfall but, also, on subsurface hydrological measurements (e.g. soil moisture content), thus defining the concept of hydro-meteorological threshold (Mirus et al., 2018b, a; Thomas et al., 2018; Segoni et al., 2018c; Wicki et al., 2020; Bogaard and Greco, 2018), that may better represent the cause-trigger concept. The term hydro-meteorological is explanatory of the fact that these types of thresholds should combine a meteorological variable (rainfall depth) with a hydrological one, reflecting the water storage at the catchment or local scale (Gain et al., 2021).

In this regard, several attempts aimed at introducing, directly or with models, the effects of soil moisture information in the empirical thresholds for improving landslides prediction have been made (Crozier, 1999; Zhao et al., 2019b; Brocca et al., 2016; Segoni et al., 2018c; Ponziani et al., 2012). For instance, Marino et al. (2020) performed an explorative investigation to figure out whether soil moisture information can improve shallow landslide forecasting using the hydro-meteorological threshold approach. They worked on real-world landslides using a synthetic time series of rainfall and a stochastic rainfall model coupled with a physically based infiltration model to generate the soil cover response, and showed that soil moisture information introduced within hydro-meteorological

thresholds can significantly reduce the false alarm ratio of LEWS, while keeping at least unvaried the number of missed alarms. Along this path, Reder and Rianna (2021) addressed to what extent may soil moisture estimations be useful to define a proxy for antecedent slope wetness conditions. Indeed, they used the soil moisture data derived from the ERA5-Land reanalysis as a support for LEWS, and more specifically as an initial filter for a pre-screening of the effective saturation degree. They showed that the filter yielded by the ERA5 soil model is able to strengthen the regional warning system and that the ERA5 reanalysis provides estimations consistent with those retrieved by using more complex and detailed physically based models.

In light of these advances, we go one step further into proposing a methodology for developing regional hydro-meteorological landslide triggering thresholds coupling observed rainfall intensity and soil moisture information derived from the ERA5-Land reanalysis (Hersbach et al., 2020) and testing their performance on a real case study. Specifically, a dataset collecting observed landslides events and observed rainfall events over the period 2010-2018 is created and the soil moisture data provided by the ERA5-Land reanalysis are used. Since ERA5-Land soil moisture information is provided at four depth levels, a Principal Component Analysis (PCA) (Rao and Burke, 1997) is carried out. PCA is a multivariate statistical analysis tool that allows reduction of the dimensionality of the soil moisture information and avoidance of information loss by combining soil moisture information from multiple depths in one variable. Thus, the methodology allows derivation of 2D thresholds with a rainfall characteristic in one axis, and the combined soil moisture variable in the other. To identify the proposed hydro-meteorological thresholds, a raw hyper-parametric threshold, based on Artificial Neural Networks (ANN) based optimization tool, is, firstly, defined. Then, in order to reduce the number of threshold parameters, a simplification of the raw threshold is performed by a simple parametric equation

having few parameters. This feature constitutes an important strength since it allows their easy application.

The paper is organized as follows. First the proposed methodology and the procedure for dataset creation are presented in the “Materials and Methods” section, focusing on the multi-step leading to the threshold identification. Then the “study area” section describes the relevant features of the study area, namely the Sicily region (southern Italy). Next, the comparison between the performance obtained with the proposed thresholds and those of the traditional ID approach is presented in “Results and Discussion” section. Finally, conclusions are drawn in the last section.

4.2. Materials and method

4.2.1. Dataset creation

The creation and configuration of the dataset is, certainly, a crucially significant step, which involves the manipulation of different type of data (i.e. observed landslides, rainfall events and, reanalysis data of soil moisture), and it is schematically reported in Figure 4.1.

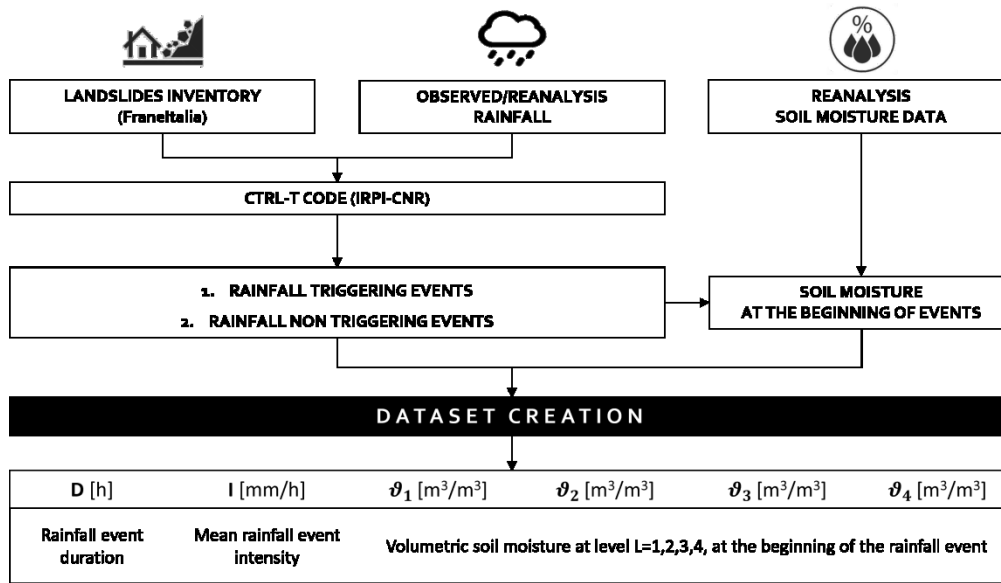


Figure 4.1 Schematization of the procedure followed for the dataset creation.

As the first step, we have recovered the information regarding the observed landslides from the *FraneItalia* project (Calvello and Pecoraro, 2018), a comprehensive spatio-temporal database of recent landslides affecting the Italian territory from 2010 onward. The catalog includes both fatal landslide events and events that did not produce physical harm to people. The main classification of the landslide events involves two categories, namely *i*) single landslide events (SLE), for records only reporting one landslide; *ii*) areal landslide events (ALE), for records referring to multiple landslides triggered by the same cause in the same geographic area. Both SLEs and ALEs are classified according to three consequence classes with the aim to record whether the event produced casualties or missing people (C1, very severe), injured people and evacuations (C2, severe), or did not cause any physical harm to people (C3, minor). Further information on catalogued landslide events includes: data on the location of the event, day of occurrence of the landslide (s), source (s) of information, and number of landslides in case of areal events. Additional information may include: onset and duration of the landslide event, landslide characteristics, phase of activity, details on the consequences. Thanks to such an accurate level of

detail, it was possible to filter only the landslide events triggered by rainfall, which are precisely those to take into consideration in our study.

The CTRL-T (Calculation of Thresholds for Rainfall-induced Landslides-Tool) code (Melillo et al., 2018) has been used, at this point, as a tool for the identification of the rainfall events that are more likely to be responsible for the observed slope failures. Specifically, CTRL-T automatically and objectively reconstructs rainfall events and the triggering conditions responsible for the failure using a set of adjustable parameters to account for different morphological and climatic settings. Briefly, the tool consists of three main distinct modules with a specific purpose. The first one operates the reconstruction of rainfall events in term of duration (D , in hours) and, cumulated event rainfall (E , in mm) using continuous hourly rainfall time series and setting several climate and spatial parameters such as, the warm period in a year (C_w); the cold period in a year (C_c); the resolution of the rain gauge (G_s); time periods used to remove irrelevant amount of rain and to reconstruct rainfall events (P_1 , P_2 , P_4); irrelevant rainfall sub-events that had to be excluded in the calculation of the final events (P_3); radius of the buffer to assign each landslide to the closest rain gauge (R_B). Rainfall event parameters were calibrated adopting the monthly soil water balance model and evapotranspiration analysis. The second block, instead, performs selection of the rain gauge representative for the landslide. The maximum allowed distance between a landslide and a rain gauge is limited by the circumferential area with radius equal to R_B . Single or multiple rainfall conditions (MRC) that are most likely responsible for the slope failures are, then, identified. Each MRC is assigned a weight to select the representative rain gauge and the rainfall conditions associated with the landslide. The weight is proportional to the inverse square distance between the rain gauge and the landslide (d^{-2}), the cumulated rainfall (E_L), and the rainfall mean intensity ($E_L D_L^{-1}$):

$$w = f(d, E_L, D_L) = d^{-2} E_L^2 D_L^{-1} \quad (4.1)$$

Among MRCs, MPRC (maximum probability rainfall conditions), is the subset of the (D_L, E_L) with the highest weights and, precisely these reconstructed rainfall conditions are assumed as the triggering events.

As shown in Figure 4.1, the last step for the dataset creation has consisted in the association of soil moisture data to the beginning of each rainfall event, both triggering and no triggering ones. Once again, the ERA5-Land reanalysis dataset has been used. Indeed, it provides the volume of water ϑ [m^3/m^3] at 4 distinct soil depth (i.e., 0-7 cm; 7-28 cm; 28-100 cm, and 100-289 cm). As the reanalysis total precipitation, the ERA5-Land soil moisture data are provided as a grid data with a horizontal resolution of $0.1^\circ \times 0.1^\circ$. Thus, we adopted a criterion of maximum nearness between the rain gauge coordinates which recorded the rainfall event, and the coordinates of the closest cell associated with the soil moisture values. Thereby, the dataset in the form shown in Figure 4.1, has been created twice, with the only difference that in the first case the measured rainfall has been used while, in the second one, the total precipitation provided by the ERA5-Land reanalysis project.

4.2.2. Principal components analysis

The Principal Components Analysis (PCA) is a multivariate technique that analyzes a data table in which observations are described by several inter-correlated quantitative dependent variables in order to extract the important information from the table and, to represent it as a set of new orthogonal variables called principal components (Abdi and Williams, 2010). Specifically, the original data are projected into a new coordinate system where the first axis, called the first principal axis, corresponds to the direction along which the data vary the most; the second axis, called the second principal axis, corresponds to the direction along which the data vary the most after the first direction, and so

on. The first principal component is the projection of the original data to the first principal axis and captures the greatest amount of the variance in the data. The second principal component is the projection of the original data to the second principal axis and explains the greatest amount of the variance in the data that is not captured by the first principal component. Each subsequent principal component explains the greatest amount of variance possible under the constraint that it is orthogonal to the preceding principal components, until all the data matrix is decomposed. Formally, mathematical solution of PCA problem ends up being equivalent to finding the eigenvalues and eigenvectors of the covariance matrix. Indeed, an eigenvector corresponds to the direction with the greatest variance in the data and, it has a corresponding eigenvalue. An eigenvalue is a number that indicates the amount of variance in the data along its corresponding eigenvector. Therefore, the eigenvector with the highest eigenvalue will be the first principal component; the eigenvector with the second highest eigenvalue will be the second principal component, and so on. Once estimated, the principal components are used to create a new coordinate space where the data can be projected into (Kherif and Latypova, 2019). Practically, in our study, θ (Eq. 4.2) represents the soil moisture data table for which to compute the principal components, specified as an n-by-p matrix. Rows correspond the total amount of the considered rainfall events (i.e. observations), and the number of columns to the 4 levels at which the initial soil moisture data are provided (i.e. variables).

$$\boldsymbol{\theta} = \begin{bmatrix} \vartheta_{11} & \vartheta_{12} & \vartheta_{13} & \vartheta_{14} \\ \vartheta_{21} & \vartheta_{22} & \vartheta_{23} & \vartheta_{24} \\ \vdots & \vdots & \vdots & \vdots \\ \vartheta_{n1} & \vartheta_{n2} & \vartheta_{n3} & \vartheta_{n4} \end{bmatrix} \quad (4.2)$$

A represents, instead, the principal components' loadings (i.e., coefficients) table, specified as an p-by-p matrix. The rows of matrix A are called the eigenvectors, and these specify the orientation of the principal components relative to the original variables.

$$\mathbf{A} = \begin{bmatrix} a_{11} & a_{12} & a_{13} & a_{14} \\ a_{21} & a_{22} & a_{23} & a_{24} \\ a_{31} & a_{32} & a_{33} & a_{34} \\ a_{41} & a_{42} & a_{43} & a_{44} \end{bmatrix} \quad (4.3)$$

Thus, the principal components (S_i) for the generic i_{th} row, are given by a linear combination of the variables θ and A , namely:

$$S_{i1} = a_{11}\vartheta_{i1} + a_{12}\vartheta_{i2} + a_{13}\vartheta_{i3} + a_{14}\vartheta_{i4} \quad (4.4)$$

$$S_{i2} = a_{21}\vartheta_{i1} + a_{22}\vartheta_{i2} + a_{23}\vartheta_{i3} + a_{24}\vartheta_{i4} \quad (4.5)$$

$$S_{i3} = a_{31}\vartheta_{i1} + a_{32}\vartheta_{i2} + a_{33}\vartheta_{i3} + a_{34}\vartheta_{i4} \quad (4.6)$$

$$S_{i4} = a_{41}\vartheta_{i1} + a_{42}\vartheta_{i2} + a_{43}\vartheta_{i3} + a_{44}\vartheta_{i4} \quad (4.7)$$

with $i = 1, \dots, n$.

In matrix notation, the transformation of the original variables to the principal components is written as,

$$\mathbf{S} = \boldsymbol{\theta}\mathbf{A} \quad (4.8)$$

4.2.3. Thresholds identification

The methodology adopted in this work aims to define regional thresholds for early warning landslides risk using the soil moisture information and, to compare the obtained performance vs. the traditional approach based on the rainfall intensity-duration power-law thresholds (ID). A schematization of the methodology is illustrated in Figure 4.2. We started by analyzing the reference case of the rainfall intensity-duration threshold, the most common type of thresholds proposed and adopted in the literature (Segoni et al., 2018a; Guzzetti et al., 2007c; Brunetti et al., 2010). The ID threshold assumes the form $I = \alpha D^{-\beta}$, where I [mm/h] represents the rainfall intensity, i.e., the average precipitation rate over the considered period; D [h] represents the duration of the rainfall event; α is the scaling parameter, and β is the shape parameter. In general, the determination of thresholds can be seen as a binary classification problem, where

triggering rainfall events are separated from non-triggering rainfall events. Once the rainfall events have been reconstructed, according to the methodology explained for the dataset creation, and the main variables have been calculated (i.e., mean rainfall intensity and duration), an optimization tool (i.e., the MATLAB® Particle Swarm optimization toolbox) has been performed with the aim to search the best possible α and β curve parameters able to maximize an objective function based on the confusion matrix or the Receiver-Operating Characteristics (ROCs). The confusion matrix is expressed in terms of the count of true positives (TP), true negatives (TN), false positives (FP) and false negatives (FN) (Peirce, 1884) (Table 4-I).

Table 4-I Confusion matrix for ROC analysis.

		Observed landslide	
		Landslide (P)	No landslide (N)
Predicted Landslide	Landslide: FS<1	TP	FP
	No landslide: FS≥1	FN	TN

As a function of the variables reported in Table 4-I, the three reference standard ROC indices – namely, True Positive Rate, False Positive Rate and True Skill Statistic – are listed below (Eqs. 4.9, 4.10, 4.11):

$$TPR = \frac{TP}{(TP + FN)} \quad (4.9)$$

$$FPR = \frac{FP}{(TN + FP)} \quad (4.10)$$

$$TSS = TPR - FPR \quad (4.11)$$

The highest performances correspond to $TSS = 1$, when, relatively to a given rainfall event, the model produces no false or missing predictions, and this TSS function (Eq. 4.11) has been maximized for the α and β curve parameters search.

The methodology for the identification of the proposed hydro-meteorological thresholds, using the soil moisture information, is illustrated in Figure 4.2. The starting point is the ERA5-Land dataset of soil moisture, which, as described in the above section, provides hourly values of soil moisture at 4 different level depths (i.e., 0-7 cm; 7-28 cm; 28-100 cm, and 100-289 cm). Thus, a Principal Component Analysis (PCA) is performed, with the aim to linearly reduce the dimensionality of the dataset and find the strongest features of the samples. At this stage, if the percentage of variance explained by the first principal component σ_1 is less than the desired value σ^* , then the data table are split based on further principal components until to reach σ^* value. Otherwise, if the percentage of variance explained by the first principal component σ_1 is greater than the desired value σ^* , then it can be inputted right away to the next step, namely the ANN-based optimization tool, implemented within the Neural Net Pattern Recognition tool in MATLAB. Artificial neural network models (ANNs) are widely used as a black-box model and, they have the ability to model linear and non-linear systems without the need to make assumptions implicitly as in most traditional statistical approaches (Al-Shamisi et al., 2013; Haykin, 2004). It can be thought up like an adaptive system that learns by using interconnected nodes or neurons in a layered structure that resembles a human brain, and, since it can learn from data, it can be trained to recognize patterns, classify data, and forecast future events. In this study, we perform a feedforward neural network, that consists of an input layer, a hidden layer and an output one. In each layer there are several nodes (i.e., neurons), and the nodes in each layer use the outputs of all nodes in the previous layer as inputs, such that all neurons interconnect with each other through the different layers. Each neuron is typically assigned a weight that is adjusted during the learning process and decreases or increases in the weight change the strength of that neuron's signal. As the training, validation and test dataset, we assumed the proportions 60%, 20%, 20%, respectively, selected randomly from the entire dataset. Finally,

according to Distefano et al. (2021), the ANNs have been trained through the scaled conjugate gradient backpropagation algorithm, while cross-entropy was assumed as the performance function for training. Thereby, it was possible to obtain a classification of the triggering and no triggering events on the basis of the mean rainfall intensity and the principal components of soil moisture data, and, even here, the True Skill Statistic (TSS) (Eq. 4.11) has been used to assess the ANN ability to correctly classify the events. The optimal classification given by the ANN-based optimization tool, is then used as indication to come up with the identification of a hyper-parametric threshold (raw threshold). Specifically, the ANN output configuration which has yielded the best TSS is reconstructed as a binary set up and, then, it was used to simulate the net adopting the discretized soil moisture value and varying the rainfall intensity throughout its range. This allowed to assemble the triggering threshold point-by-point, by detecting the switching points (from zero to one). Finally, the raw threshold thus obtained is simplified through a parametric equation assuming the following form:

$$y = \begin{cases} y_0, & x < x_0 \\ \frac{y_1 - y_0}{x_1 - x_0} (x - x_0) + y_0, & x_0 \leq x \leq x_1 \\ y_1, & x > x_1 \end{cases} \quad (4.12)$$

where, x_0, x_1, y_0 and y_1 are the optimal threshold's parameters, defined through a trial-and-error procedure aimed to obtain a $TSS_{par} \geq TSS_{raw}$ that does not guarantee, therefore, to reach the optimal TSS_{opt} . The choice to use Eq. 4.12 is the result of several attempts, not reported in the study for the sake of brevity, which led to finding out that such a curve is able to better approximate the raw one.

A schematic description of the methodology is reported in Figure 4.2.

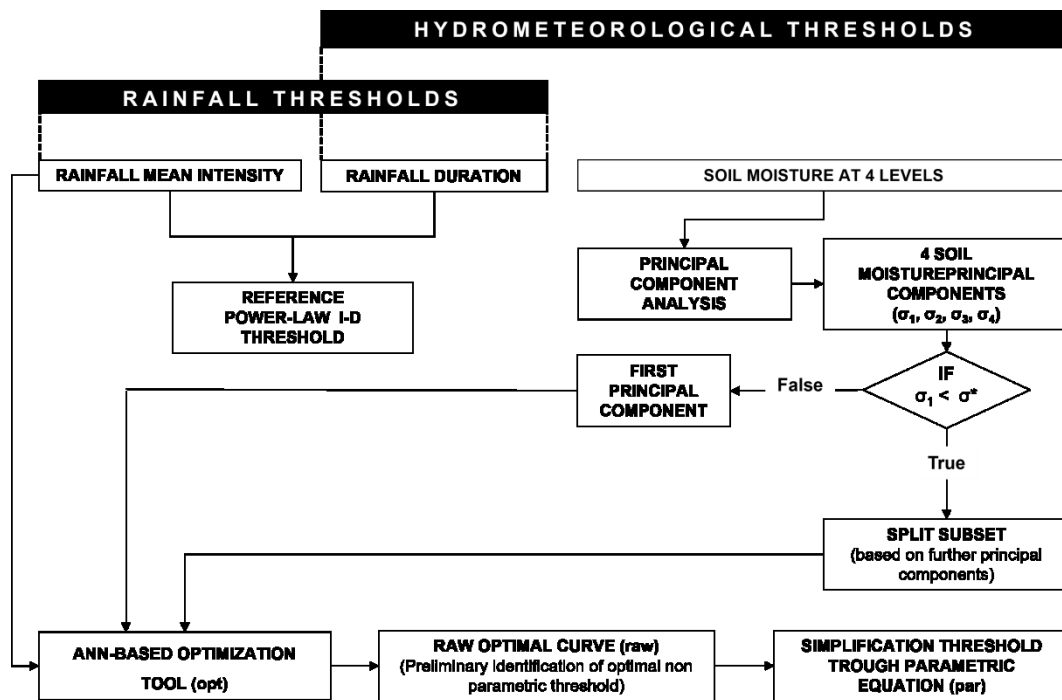


Figure 4.2 Description of the methodology.

4.3. Study area

The study area selected for our study is the island of Sicily (southern Italy, 37.75N-14.25 E) which, with an area of ~25,700 km², is the largest island of the Mediterranean Sea. A hilly morphology (62%) dominates the landscape in the island, while the rest is characterized by a mountainous and flat morphology among which the widest is around Catania, in the eastern part of the island. The terrain average elevation is about 400 meters, ranging from sea level to 3320 meters at Mount Etna, the highest active volcano in Europe. From a geological point of view, the Sicily Island is the result of the convergence between the European and the African plates in the Neogene. The island is characterized by a complex geological and lithological setting which, added to a variety of human actions (including e.g., land use changes, forest management, and forest fires) have produced different soils in Sicily (Venturella, 2004). The climate is warm-temperate, with hot and dry summers, especially on the southern coasts, and higher and more frequent precipitation during the colder winter months, in the

mountainous internal areas (Pumo et al., 2019). Mean annual precipitation ranges between 700 and 800 mm, and the majority of the rainfall events occurs in autumn and winter, rather than in the summer. The eastern side of the island is affected by severe storms. The largest precipitations are recorded on the eastern slopes of Mount Etna and along the Peloritani Mountains, with highest values on the Ionian side (Gariano et al., 2015). On the other side, the southern part of the island is characterized by lower rainfalls than the regional average since its exposition to hot and dry winds from Africa and its lower elevations (Alecci and Rossi, 2007). Figure 4.3 shows the geographical context within which Sicily is located. In more detail, the rain gauges locations for the period 2009-2018 (Distefano et al., 2021) are represented, as well as, the observed landslide locations. In more detail, 207 landslide events were retrieved from 2010 to 2018 and, for each of them, longitude-latitude coordinates (WGS84 datum), together with the initiation time, are retrieved.

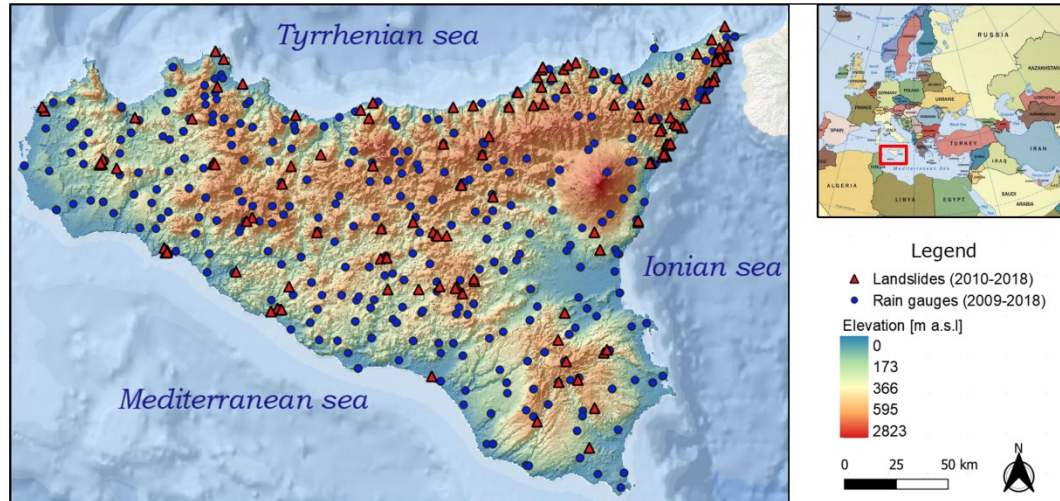


Figure 4.3 Elevation map of the study area (Sicily region), showing the location of the landslide occurrences (Calvello and Pecoraro, 2018) and of the rain gauges, over the period 2010-2018 (Distefano et al., 2021).

The analysis aimed at the identification of the hydro-meteorological thresholds has been carried out on two datasets. As illustrated in Section 4.1, on one side, the observed rainfall is used as an input parameter to the proposed multi-step

methodology; on the other side, the ERA5-Land reanalysis precipitation is used. Therefore, on one side, we referred to the three main Sicilian measuring networks, managed by the regional water observatory (Osservatorio delle Acque, OdA), the SIAS (Sicilian Agro-meteorological Information Service), and by the Regional Civil Protection Department (DRPC), respectively. Overall, a time series for the period 2009-2018, of the hourly precipitation has been reconstructed. On the other side, the total precipitation provided by ERA5-Land reanalysis project was also considered, with the aim to apply in parallel the same proposed methodology and compare the results obtained using, indeed, the observed and the reanalysis. The ERA5-Land project provides the total rainfall [m] as accumulated liquid and frozen water, including rain and snow. As reported by the Copernicus Climate Change Service, total precipitation is the sum of large-scale precipitation and convective precipitation and it can be easily thought as the depth the water would have if it were spread evenly over the grid box. Indeed, these data are provided as gridded data with a horizontal resolution of $0.1^\circ \times 0.1^\circ$, thus we assumed that the center coordinates of each grid cell are similar to those of an hypothetical rain gauge. Here too, a time series for the period 2009-2018, of the hourly precipitation has been reconstructed, paying attention to the fact that the reanalysis total precipitation is provided as the accumulated rainfall from the beginning of the forecast time to the end of the forecast step. Obviously, when this reanalysis variable is considered, it should be considered that it represents averages over a model grid box and model time step, rather than a local measurement referred to a particular point in space and time.

4.4. Results and discussion

4.4.1. Principal component analysis

The preliminary step, required when the principal component analysis is performed, is to center the data on the mean values of each variable, namely by

subtracting the mean of a variable from all values of that variable. This step allows that the cloud of data is centered on the origin of the principal components, but it does not affect the spatial relationships of the data, nor the explained variance along the variables. At this stage, it was possible to proceed with the Principal Component Analysis, whose loadings values, representing the orientation of the principal components relative to the original variables, are represented by the matrix A, as follows:

$$A = \begin{bmatrix} 0.65 & -0.54 & 0.37 & -0.38 \\ 0.58 & -0.04 & -0.29 & 0.76 \\ 0.47 & 0.63 & -0.39 & -0.48 \\ 0.15 & 0.55 & 0.79 & 0.23 \end{bmatrix} \quad (4.13)$$

The loadings values within a particular row of matrix A, are intended as the weights a_{ij} (Eq. 4.3), and the larger they are, the more they contribute to a particular principal component. The sign of a loading indicates whether a variable and a principal component are positively or negatively correlated. Here, although overall slightly large loadings correspond to the first principal component, none of the four variables has a strong relationship with a particular principal component. According to Eqs. 4.4, 4.5, 4.6, and 4.7, the four principal components of soil moisture are defined as follow:

$$S_{i1} = 0.65\vartheta_{i1} + 0.58\vartheta_{i2} + 0.47\vartheta_{i3} + 0.15\vartheta_{i4} \quad (4.14)$$

$$S_{i2} = -0.54\vartheta_{i1} - 0.04\vartheta_{i2} + 0.63\vartheta_{i3} + 0.55\vartheta_{i4} \quad (4.15)$$

$$S_{i3} = 0.37\vartheta_{i1} - 0.29\vartheta_{i2} - 0.39\vartheta_{i3} + 0.79\vartheta_{i4} \quad (4.16)$$

$$S_{i4} = -0.38\vartheta_{i1} + 0.76\vartheta_{i2} - 0.48\vartheta_{i3} + 0.23\vartheta_{i4} \quad (4.17)$$

Figure 4.4 shows, instead, the scree plot representing the total percentage of variance explained by each of the four principal components. The chart reveals

the decreasing rate at which variance is explained by additional principal components.

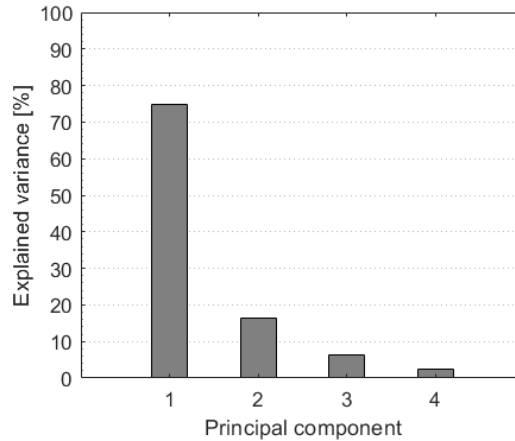


Figure 4.4 Total variance explained by each principal component.

Because dimensionality reduction is a goal of principal components analysis, several criteria can be considered for determining how many principal components should be examined and how many should be ignored (Rencher, 1998). Just to list a few: *i*) ignore principal components at the point at which the next principal component offers little increase in the total explained variation; *ii*) ignore the last principal component whose explained variation are all roughly equal; *iii*) include all principal components up to a predetermined total explained variation σ^* . In our study, this last criterion has been used, by setting $\sigma^* = 90\%$, when the split subset, based on further components, is considered. As shown by Figure 4.4, to reach σ^* , the first and the second principal components are examined, while the last two are ignored.

4.4.2. Analysis using observed rainfall

The first step, as mentioned in the methodology section, has been to apply CTRL-T software for reconstructing rainfall events from the observed rainfall series. CTRL-T tool reconstructed 144 landslide events out of the 207 inputted ones. The landslides for which the rainfall conditions were not identified or with relevant

uncertainties, were discarded. First, we have derived the *ID* threshold. Specifically, the *ID* threshold was identified as a power law approach and then by the proposed optimization methodology (Figures 4.5 and 4.6).

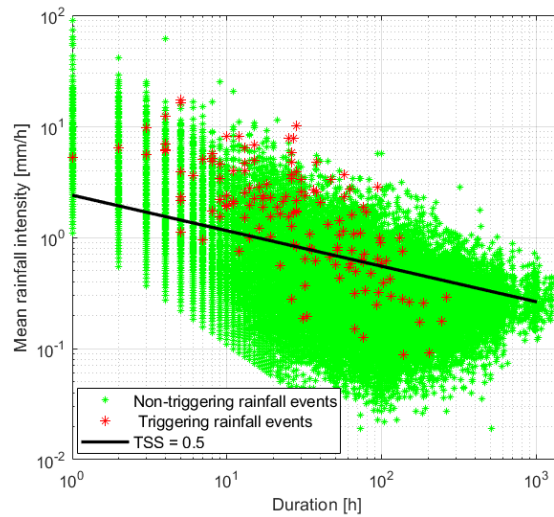


Figure 4.5 Traditional power-law threshold on the log-log plane between observed mean rainfall intensity (*I*) and duration (*D*).

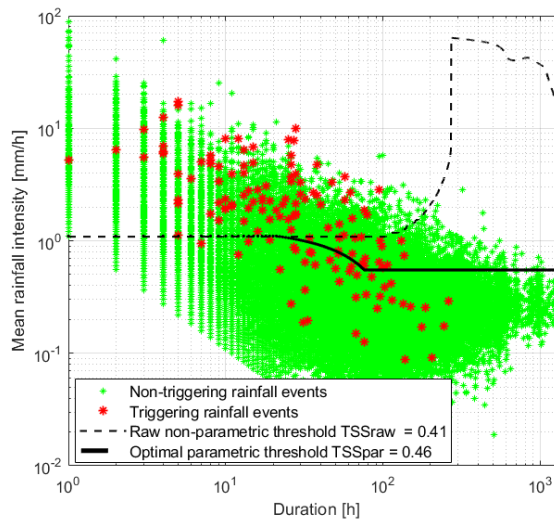


Figure 4.6 Optimal parametric threshold (black line) on the log-log plane between observed mean rainfall intensity (*I*) and duration (*D*). The raw non-parametric threshold (dash black line) is also shown.

As can be noted, moving from the power law *ID* threshold to the optimal parametric one, a slight decrease of the True Skill Statistic index can be observed, from 0.5 to 0.46, respectively, even if the optimal TSS value, at the end of the

ANN-based optimization tool, is the greatest ($TSS_{opt} = 0.54$). Indeed, switching from the ANN-based tool to the parametrization procedure, necessarily implies a slight decline in performance. This performance, furthermore, is in line with results obtained by Distefano et al. (2021), who have gained a $TSS_{opt} = 0.59$ for the same study area. In our study, the TSS_{opt} value resulting from the ANN-based optimization is taken as reference against which the proposed hydro-meteorological thresholds are compared, with the aim to assess possible improvements. In this regard, we investigated three possible alternatives for the hydro-meteorological thresholds:

- a. Rainfall intensity and soil moisture at each four depth levels (e.g., 0-7 cm, 7-28 cm, 28-100 cm, 100-289 cm);
- b. Rainfall intensity and first principal component of soil moisture;
- c. Rainfall intensity and first principal component of soil moisture, conditioned to given classes of the second principal component of soil moisture.

For each type of threshold, the methodology explained in the previous section has been applied, and the results are discussed in the following.

Table 4-II summarizes the TSS values in correspondence of the analyzed thresholds, together with the values of parameters (Eq. 4.12) estimated for the optimal parametric thresholds. In more detail, the TSS_{opt} value resulted from the ANN-based optimization tool is reported, along with the TSS_{raw} (i.e. TSS of the raw non-parametric threshold), the TSS_{par} (i.e. TSS of the optimal parametric threshold), and the TSS_{pl} (i.e. TSS of the ID threshold using the traditional power-law approach).

Chapter 4 – Identification of regional landslide triggering thresholds using multivariate statistical analysis and reanalysis soil moisture data

Table 4-II Summarizing table of the TSS values in correspondence of each analyzed scenario when the observed rainfall is used, and parameters (x_0, y_0, x_1, y_1) estimated for the optimal parametric thresholds.

Threshold	TSS _{pl}	TSS _{opt}	TSS _{raw}	TSS _{par}	x ₀	y ₀	x ₁	y ₁
⊙⊙	0.50	0.54	0.41	0.46	21.0	1.10	76.0	0.55
⊙⊙1	[-]	0.71	0.63	0.65	0.20	17.8	0.38	0.07
⊙⊙2	[-]	0.68	0.52	0.54	0.30	28.6	0.35	0.09
⊙⊙3	[-]	0.60	0.60	0.58	0.20	4.5	0.37	0.08
$I\theta_4$	[-]	0.52	0.46	0.44	0.24	4.30	0.31	0.10
IS_1	[-]	0.70	0.61	0.67	0.04	4.40	0.20	0.02
$IS_1 (S_{2,min} < S_2 < 0.6S_{2,max})$	[-]	0.64	0.55	0.60	0.02	4.40	0.11	0.12
$IS_1 (0.6S_{2,max} < S_2 < S_{2,max})$	[-]	0.79	0.72	0.71	0.12	9.13	0.20	0.08
IS_1 (both S_2 classes)	[-]	[-]	0.61	0.64	[-]	[-]	[-]	[-]

Figure 4.7 shows the obtained thresholds when the mean rainfall intensity and the soil moisture at each of the four depth levels are considered, respectively. The dash black line is the raw threshold resulting from the ANN-based optimization, and it constitutes the starting point around which the parametric threshold is developed. Greater TSS values are obtained for the first three levels, with a TSS_{par} equal to 0.65, 0.54, and 0.58, respectively, while a slightly lower TSS_{par} equal to 0.44, is obtained with the fourth soil moisture level.

The best improvements in performance are, therefore, obtained for the upper layer of soil moisture with a $TSS_{par} = 0.65$ vs. $TSS_{opt} = 0.54$ for the ID threshold. Overall, generally, the parametrization of the optimal threshold is able to moderately improve the performance of the raw threshold or, at least, to equal it.

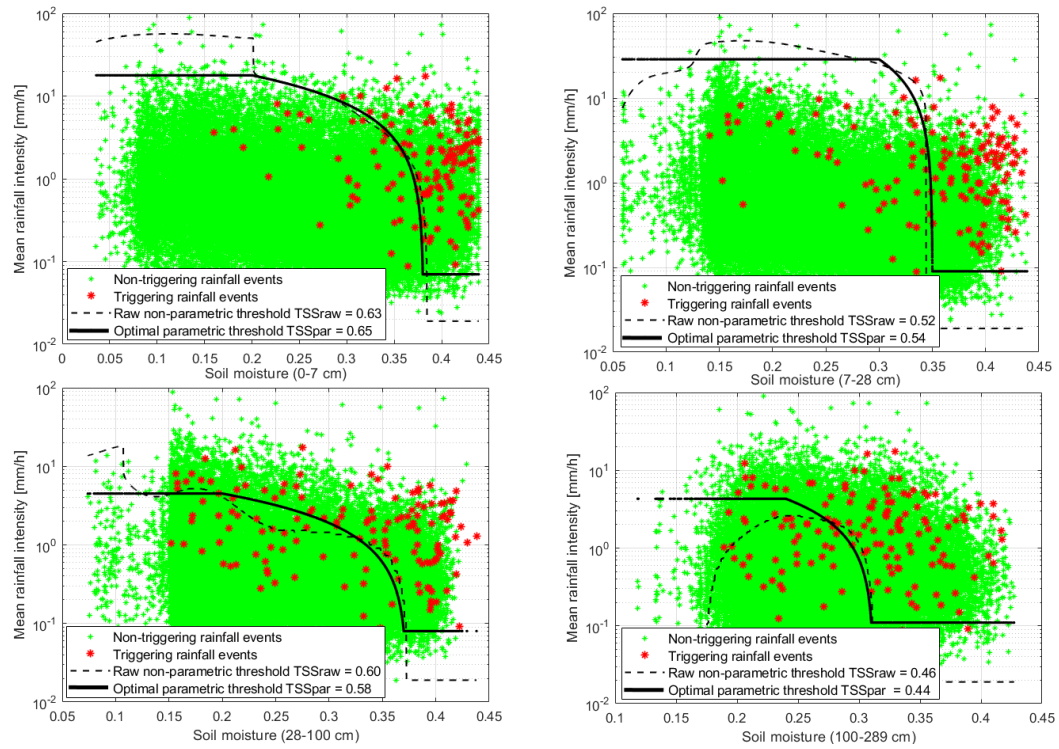


Figure 4.7 Panel showing the raw non-parametric thresholds and the corresponding optimal parametric thresholds on the semi-log plane between mean rainfall intensity and soil moisture at the four distinct depths.

As mentioned before, the second analysis concerns the identification of the optimal parametric thresholds when the rainfall intensity and first principal component of soil moisture are considered (Figure 4.8). In this case, a $TSS_{par} = 0.67$ is obtained, giving a slight improvement in comparison with the previous scenario and, certainly, with the *ID* approach. The scores of the first principal component of soil moisture are given by Eq. 4.14, and, overall, contain the 75% of the total variance of the data. The triggering rainfall events over threshold are, for the most, located into the right side of the graph, in correspondence to the highest values of the first principal components of soil moisture S_1 ranging from 0.2 and 0.3.

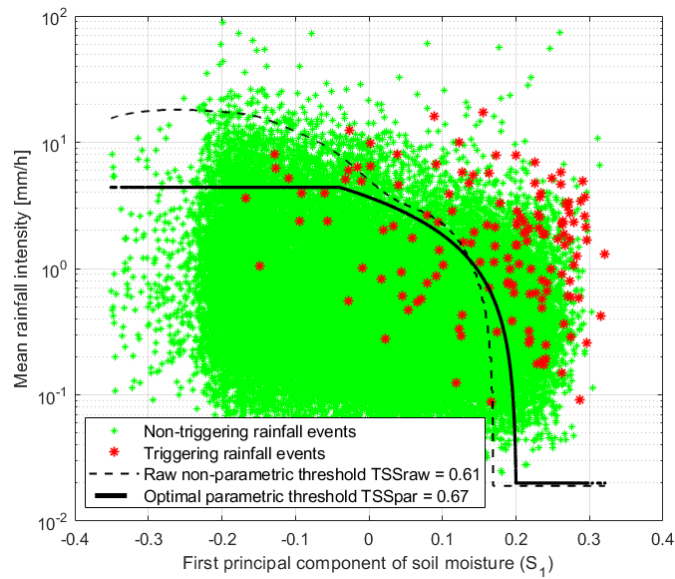


Figure 4.8 Optimal parametric threshold (black line) on the semi-log plane between observed mean rainfall intensity (I) and first principal component of soil moisture (S_1). The raw non-parametric threshold (dash black line) is also reported.

Then, we explored whether adding the information contained in the second principal component of soil moisture was likely to provide effective benefits in the prediction. In order to keep the thresholds simple, we did not carry out a fully 3D analysis. We have rather conditioned the IS_1 thresholds to given classes of S_2 . The first one contains the 60% of data within the range $S_{2,min} < S_2 < 0.6 S_{2,max}$, the second one the remaining 40% within the range $0.6 S_{2,max} < S_2 < S_{2,max}$. The creation of these subsets allowed us to have an equal number of observed landslides in both classes and, moreover, to reach the σ^* value of the total variance amounting to 91.3%. Although a third variable was added, this procedure made it possible for us to come up, once again, with the identification of 2D thresholds. Results are shown in Figure 4.9. As can be seen, the best performance is obtained when the second class of the second principal component of soil moisture (S_2) is considered in the analysis, featuring a $TSS_{par} = 0.71$ for the optimal parametric threshold. However, in this scenario, the True Skill Statistic index has to be assessed as a weighted average of the TSS of both classes, through the following Eq. 6.18:

$$TSS_{all} = ((TPR_1P_2) + (TPR_2P_1)/(P_1 + P_2)) + -((FPR_1N_2) + (FPR_2N_1)/(N_1 + N_2)) \quad (4.18)$$

where, TPR is the True Positive rate (Eq. 4.9), FPR is the False Positive Rate (Eq. 4.10), $P = TP + FP$ represents the number of observed landslides, and $N = FP + TN$ represents the number of non-landslides. The subscripts 1 and 2 refer to the threshold for first and second class of the second principal component of soil moisture, respectively. Using Eq. 4.18, a weighted TSS_{par} equal to 0.64 is found. Thus, a near value to that obtained for the IS_1 threshold.

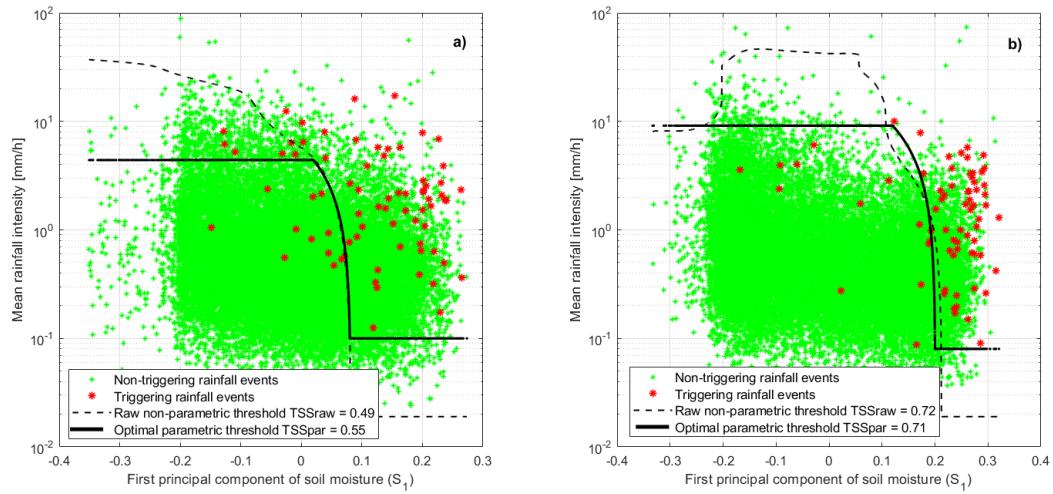


Figure 4.9 Optimal parametric threshold (black line) on the semi-log plane between the observed mean rainfall intensity (I) and the first principal component of soil moisture (S_1). (a) Shows the case when the first class of the second principal component of soil moisture is considered; (b) Shows the case when the second class of the second principal component of soil moisture is considered. The raw non-parametric thresholds (dash black line) are also reported in both cases.

Overall, the proposed hydro-meteorological thresholds are able to better predict the landslide occurrences, if compared with the performance of the traditional ID approach. Indeed, each investigated threshold resulted in TSS_{par} values of the optimal parametric thresholds up to 0.67, confirming that adding soil moisture information into the identification of landslide triggering thresholds, can improve significantly their predictive performance. Furthermore, note that these results are consistent with the those obtained through numerical simulations based on synthetic data series by Marino et al. (2020). Specifically, when considering the comparison between the ID thresholds' performance and the

hydro-meteorological ones, Marino et al. (2020) gained an increase, in terms of True Skill Statistic, equal to about 0.2, at best, that is approximately equal as that obtained in our study.

4.4.3. Analysis using ERA5-Land rainfall

This section presents the results obtained when the ERA5-Land reanalysis rainfall is used as an input parameter to the proposed multi-step methodology, following the same order as the previous section. This once, the CTRL-T software reconstructed a greater number of landslides, namely 160 landslide events out of the 207 inputted ones. This can be probably attributed to the different type of measure, being the reanalysis rainfall, a gridded data evenly distributed in the study area, unlike the less spread measurements of the rain gauges. First of all, the rainfall characteristics (i.e., mean rainfall intensity (I) and duration (D)) have been used to carry out the optimal ID threshold, within the log-log plane. The ID thresholds derived through both the power law approach and the proposed optimization methodology are shown in Figures 4.10 and 4.11, respectively.

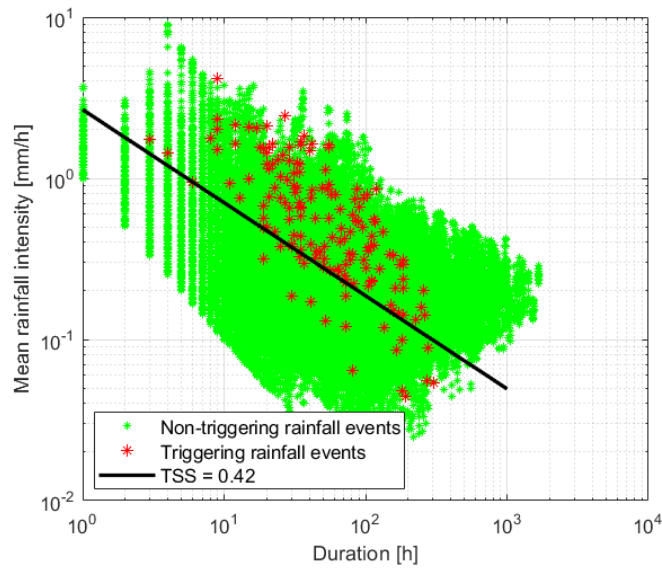


Figure 4.10 Traditional power-law threshold on the log-log plane between ERA5-Land mean rainfall intensity (I) and duration (D).

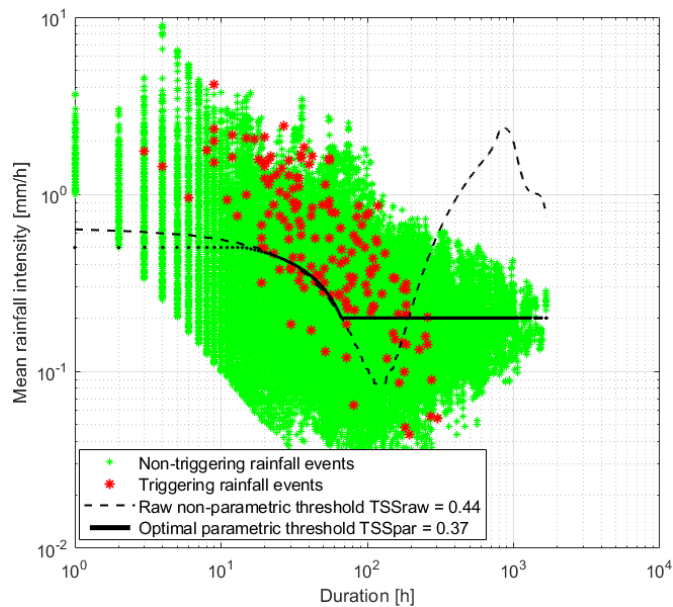


Figure 4.11 Optimal parametric threshold (black line) on the log-log plane between ERA5-Land mean rainfall intensity (I) and duration (D). The raw non-parametric threshold (dash black line) is also shown.

As can be noted, moving from the observed rainfall to the reanalysis rainfall as an input data, the True Skill Statistic index of the ID threshold drops slightly, as well as, moving from the power law ID threshold to the optimal parametric one. Indeed, as can be noted, even the TSS_{opt} assessed through the ANN-based optimization is lower than one obtained when the observed rainfall is used (i.e.,

$TSS_{opt} = 0.54$). Also here, the three previously types of thresholds were investigated (see Section 4.4.2 at letters a, b, and c), and the results are discussed in the following. Figure 4.12 shows the obtained thresholds when the mean rainfall intensity and the soil moisture at each of four depth levels are considered, respectively. The dash black line is the raw threshold resulted from the ANN-based optimization, and it has been used as guidance for the developing of the parametrization threshold procedure.

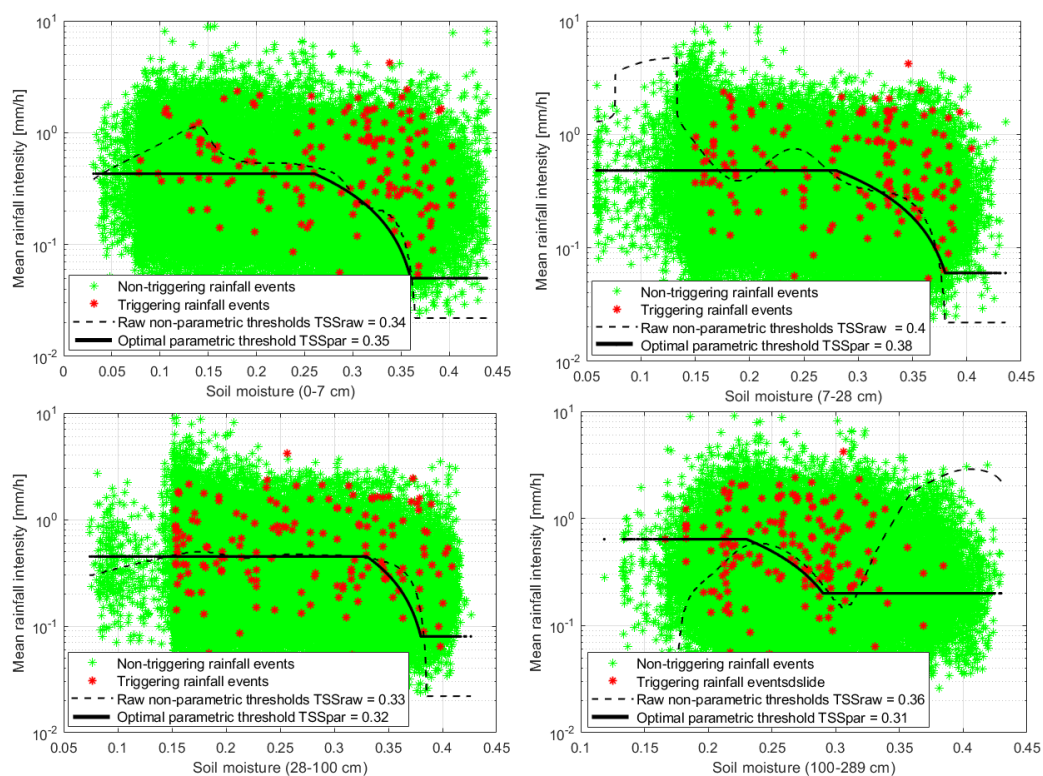


Figure 4.12 Panel showing the raw non-parametric thresholds and the corresponding optimal parametric thresholds on the semi-log plane between ERA5-Land mean rainfall intensity (I) and soil moisture at the four distinct depths.

Figure 4.12 shows as a slight decline in performance is confirmed when the reanalysis precipitation is inputted in the proposed procedure. For none of these cases, the TSS_{par} values are able to reach the ID performance, getting stuck at most to a $TSS = 0.38$, when the second layer of soil moisture is considered (i.e., 7-28 cm depth). Indeed, the rainfall triggering events (i.e., red markers in Figure 4.12) are more scattered and the thresholds' ability to provide a correct

classification of the landslide events is not very effective. Then, the analysis concerning the identification of the optimal parametric thresholds when the rainfall intensity and first principal component of soil moisture are considered, has been analyzed (Figure 4.13).

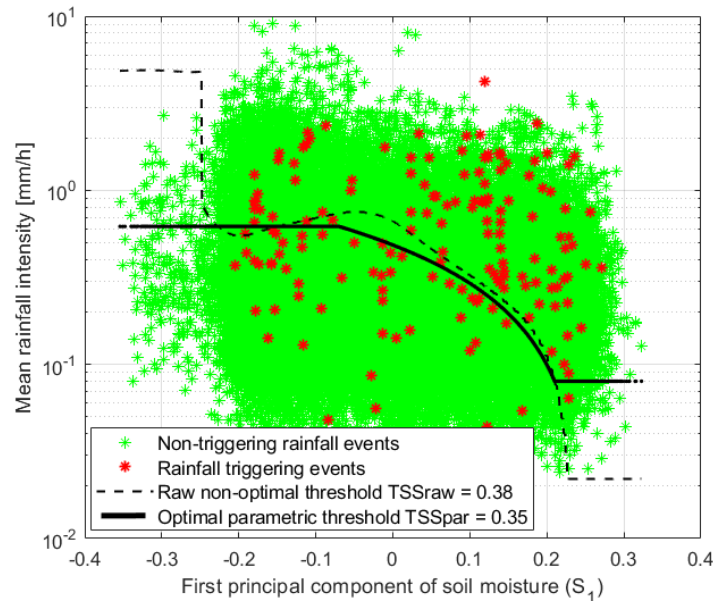


Figure 4.13 Optimal parametric threshold (black line) on the semi-log plane between ERA5-Land mean rainfall intensity (I) and first principal component of soil moisture (S_1). The raw non-parametric threshold (dash black line) is also shown.

In this case, a $TSS_{opt} = 0.35$ is obtained through the optimal parametric threshold, stopping still below the ID performance $TSS_{opt} = 0.44$. Furthermore, unlike when the observed precipitation is considered, here, the triggering rainfall events over threshold are mostly spread within the whole point cloud, and no longer in correspondence to the highest values of the first principal components of soil moisture S_1 .

Lastly, the information contained in the second principal component of soil moisture was added in the analysis, with the aim to explore whether or not it can provide effective benefits in the prediction (Figure 4.14). Once again, we split the second principal component of soil moisture (S_2) into two classes, even if, now, it has been split right down in the middle to have an equal number of observed landslides in both classes, and to reach again the σ^* value of the total variance

amounting to 91.3%. Using Eq. 4.18 a weighted TSS equal to 0.42 is found (Table 4-III). As can be seen in Figure 4.14, although the obtained performance is better than those obtained when the mean rainfall intensity and first principal component of soil moisture are considered, the IS_1 threshold conditioned to a given class of S_2 seems to not bring any effective improvement in the landslides prediction. Indeed, a TSS_{par} value equal to 0.42 is obtained vs. $TSS_{opt} = 0.44$ obtained for the ID approach.

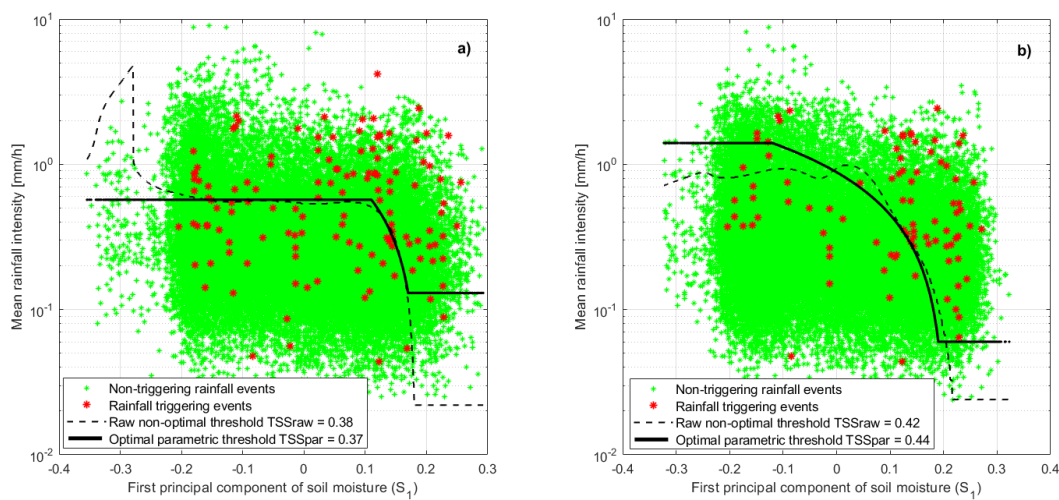


Figure 4. 14 Optimal parametric threshold (black line) on the semi-log plane between ERA5-Land mean rainfall intensity (I) and first principal component of soil moisture (S_1). (a) Shows the case when the first class of the second principal component of soil moisture (S_2) is considered; (b) Shows the case when the second class of the second principal component of soil moisture (S_2) is considered. The raw non-parametric thresholds (dash black line) are also shown in both cases.

In order to give an overview of the obtained results, Table 4-III summarizes the TSS values in correspondence of the analyzed scenarios, together with the values of parameters (Eq. 4.12) estimated for the optimal parametric thresholds. Here, the TSS_{opt} value resulted from the ANN-based optimization tool is also reported, along with the TSS_{raw} (i.e. TSS of the raw non-parametric threshold), the TSS_{par} (i.e. TSS of the optimal parametric threshold), and the TSS_{pl} (i.e. TSS of the i.e. ID threshold using the traditional power-law approach).

Table 4-III Summarizing table of the TSS values in correspondence of each analyzed scenario when the ERA5-Land rainfall is used, and parameters (x_0, y_0, x_1, y_1) estimated for the optimal parametric thresholds.

Threshold	TSS _{pt}	TSS _{opt}	TSS _{raw}	TSS _{par}	x_0	y_0	x_1	y_1
<i>ID</i>	0.42	0.44	0.44	0.37	14.4	0.5	66.5	0.20
<i>Iϑ_1</i>	[-]	0.42	0.34	0.35	0.26	0.43	0.36	0.05
<i>Iϑ_2</i>	[-]	0.43	0.40	0.38	0.28	0.48	0.38	0.06
<i>Iϑ_3</i>	[-]	0.38	0.33	0.32	0.33	0.45	0.38	0.08
<i>Iϑ_4</i>	[-]	0.41	0.36	0.31	0.23	0.64	0.29	0.2
<i>IS₁</i>	[-]	0.40	0.38	0.35	-0.07	0.62	0.21	0.08
<i>IS₁ ($S_{2,min} < S_2 < 0.6S_{2,max}$)</i>	[-]	0.41	0.38	0.37	0.11	0.57	0.15	0.13
<i>IS₁ ($0.6S_{2,max} < S_2 < S_{2,max}$)</i>	[-]	0.47	0.42	0.44	-0.12	1.4	0.19	0.06
<i>IS₁ (both S_2 classes)</i>	[-]	[-]	0.36	0.42	[-]	[-]	[-]	[-]

Overall, using the reanalysis rainfall, the proposed hydro-meteorological thresholds do not improve the prediction of landslides occurrences, quite the opposite of what happens when the observed rainfall is used. Therefore, it is clear how the quality of the rainfall data has a decisive influence in the thresholds' ability to correctly predict landslide events. In this regard, several studies have shown that ERA5 reanalysis precipitation estimates have uncertainties that, for the most part, result in an overestimation (Jiang et al., 2021; Amjad et al., 2020; Xu et al., 2019), and that the accuracy of the precipitation product is strongly correlated with the topographic distribution, climate divisions (Jiang et al., 2021; Jiao et al., 2021), and with the errors of models and observations in the data assimilation system (Nie et al., 1955). Thus, it is hard to completely replace observed measurements with reanalysis system information to gain the true state of the atmosphere (Bengtsson et al., 2004) since the shortcomings of the reanalysis may lead to biased precipitation estimates over different regions (Beck et al., 2020; Belo-Pereira et al., 2011; Jiang et al., 2021).

4.5. Conclusions

In this study, we have proposed a multi-step procedure aimed at the identification of hydro-meteorological thresholds using multivariate statistical analysis and ERA5-Land reanalysis soil moisture information. Specifically, a non-parametric threshold is, firstly, derived from an optimization procedure based on Artificial Neural Networks (ANN) and maximization of the ROC True Skill Statistic (TSS) index. Then, a parametric equation is used to simplify the non-parametric threshold derived at the first step. This procedure has been tested twice; once using the observed rainfall as an input parameter, and once using the ERA5-Land reanalysis rainfall. In comparison to the performance of the *ID* threshold, that has been taken as reference, the proposed optimal parametric thresholds are able to better classify the landslide occurrences when the observed rainfall is inputted into the ANN-based optimization tool. In this case, a significant improvement has been found, since TSS_{par} values ranging from 0.64 to 0.67, according to the considered threshold, were found out, that are greater values than those obtained for the *ID* approach (i.e., $TSS_{pl} = 0.50$ and $TSS_{opt} = 0.54$). On the other side, a drop in performance is recorded when the reanalysis precipitation is used and lower TSS values are obtained in correspondence of all investigated scenarios. However, this is to be expected due the nature of the reanalysis rainfall data. In fact, although they are easily available in time and space, they have to be assumed as gridded averaged values and, furthermore, suffer in uncertainties correlated with topographic distribution, climate divisions and with the errors of models and observations in the data assimilation system. Overall, the obtained results represent a step forward to the improvements of landslide thresholds identification and are in line with the recent developments in literature. Furthermore, these results support as the soil moisture is a predisposing factor in the landslide initiation mechanism.

Chapter 5

Improving Spatial Landslide Prediction with 3D Slope Stability Analysis and Genetic Algorithm Optimization

Palazzolo, N., Peres, D.J., Bordoni, M., Meisina, C.; Creaco, E.; Cancelliere, A.

Abstract

In this study, we compare infinite slope and the three-dimensional stability analysis performed by SCOOPS 3D (software to analyze three-dimensional slope stability throughout a digital landscape). SCOOPS 3D is a model proposed by the U. S. Geological Survey (USGS), the potentialities of which have still not been investigated sufficiently. The comparison between infinite slope and 3D slope stability analysis is carried out using the same hydrological analysis, which is performed with TRIGRS (transient rainfall infiltration and grid-based regional slope-stability model)—another model proposed by USGS. The SCOOPS 3D model requires definition of a series of numerical parameters that can have a significant impact on its own performance, for a given set of physical properties. In the study, we calibrate these numerical parameters through a multi-objective optimization based on genetic algorithms to maximize the model predictability performance in terms of statistics of the receiver operating characteristics (ROC) confusion matrix. This comparison is carried out through an application on a real case study, a catchment in the Oltrepò Pavese (Italy), in which the areas of triggered landslides were accurately monitored during an extreme rainfall on 27–28 April 2009. Results show that the SCOOPS 3D model performs better than the 1D infinite slope stability analysis, as the ROC True Skill Statistic increases from 0.09 to 0.37. In comparison to other studies, we find the 1D model performs

worse, likely for the availability of less detailed geological data. On the other side, for the 3D model we find even better results than the two other studies present to date in the scientific literature. This is to be attributed to the optimization process we proposed, which allows to have a greater gain of performance passing from the 1D to the 3D simulation, in comparison to the above-mentioned studies, where no optimization has been applied. Thus, our study contributes to improving the performances of landslide models, which still remain subject to many uncertainty factors.

Keywords: TRIGRS; SCOOPS 3D; rainfall induced landslide; slope stability analysis; optimization.

5.1. Introduction

Shallow rainfall-induced landslides frequently cause human losses and substantial damages to infrastructures in many mountain and hilly regions worldwide (Froude and Petley, 2018). Landslides can have devastating effects on the downstream area, especially when they evolve into debris flow (Stancanelli et al., 2017; Peres and Cancelliere, 2018a; Manenti et al., 2020). As a result, many efforts have been devoted to the development of techniques and methodologies useful for the space-time prediction of rainfall-induced landslides.

Models for determining the rainfall conditions that trigger landslides can be broadly divided into two categories, namely rainfall triggering thresholds and numerical physically based models. The former are defined as the rainfall conditions the exceedance of which is likely to trigger landslides (Segoni et al., 2018a; Piciullo et al., 2018; Bordoni et al., 2019). Due to the empirical nature of this approach (Aleotti, 2004a; Cannon et al., 2008; Dahal and Hasegawa, 2008; Giannecchini et al., 2012; Guzzetti et al., 2007a, 2008a; Innes, 1983b; Leonarduzzi et al., 2017b; Peruccacci et al., 2012b), the quality and reliability of input data can affect the reliability of the prediction (Hong et al., 2006; Nikolopoulos et al., 2014b; Peres et al., 2018; Marra, 2019). The latter simulate the hydrological and geotechnical processes responsible for the trigger (Baum and Godt, 2010; Lepore et al., 2013; Segoni et al., 2009; Alvioli and Baum, 2016; Bordoni et al., 2015a), and can be used also for hazard mapping and thus for land planning purposes. However, their application may be hampered by the limited availability of data on soil properties (Bordoni et al., 2017; Valentino et al., 2011). These models are composed of two parts: a hydrological model to determine the soil response to rainfall in terms of pore pressure changes and a slope stability model to estimate the induced change in the ratio of resisting to driving forces acting on potential sliding masses (Rosso et al., 2006; Crosta and Frattini, 2003).

The great majority of landslide models used infinite slope stability analysis

(Baum and Godt, 2010; Peres and Cancelliere, 2016; Yao et al., 2019b; Salvatici et al., 2018; Zieher et al., 2017b; Raia et al., 2014b; Lepore et al., 2013; Chiu et al., 2019; Strauch et al., 2019), according to which the failure of each cell is assumed to be independent of the other ones in the catchment, resulting in unstable areas that have low connectivity, which are thus quite unrealistic. Hence, there is an increasing scientific interest towards the development of software that implements three-dimensional slope stability analysis (Lehmann and Or, 2012; Bellugi et al., 2015; Anagnostopoulos et al., 2015; Milledge et al., 2014; Lu et al., 2014; Dai et al., 2014; Fan et al., 2017). SCOOPS 3D (software to analyze 3D slope stability throughout a digital landscape) (Reid et al., 2015) belongs to the 3D models category and uses a three-dimensional (3D) approach to assess the stability of many potential landslides within a user-defined size range and considering landslide triggering as a cascade of failures of interconnected soil columns. When applied to the catchment scale, based on a digital terrain model (DTM), 3D slope stability analysis requires rather complex algorithms aimed at searching iteratively the unstable surfaces (landslides), which involve several numerical parameters. Setting these parameters in the optimal manner may be a tedious task and discourage the application of these models, or even induce performances which do not reflect their potentialities.

In this paper, we firstly aim to contribute to the investigation of the real advantages and disadvantages of 1D vs. 3D slope stability analysis at the catchment scale. Given the limitation mentioned above, we propose to use optimization techniques to define the numerical parameters of 3D slope stability models. In this context, we propose the use of genetic algorithms, a technique known for its efficiency and stability in finding global optimum solutions.

Specifically, we investigate the performance of two different models from the published literature, namely: TRIGRS (transient rainfall infiltration and grid-based regional slope-stability) (Alvioli and Baum, 2016; Baum et al., 2002), and

the above mentioned SCOOPS 3D (Reid et al., 2015). This methodology is applied on a river basin in the Oltrepò Pavese area (northern Italy), where several landslides were triggered after an extreme rainfall event (160 mm in 48 h) on 27–28 April 2009.

The last version of TRIGRS, i.e., v.2.1, provides as output a dedicated 3D format of pore water pressures suitable for the slope stability analysis in SCOOPS 3D (Alvioli and Baum, 2016). Besides, TRIGRS also performs a 1D stability analysis, based on infinite slope assumption, which can be compared to the results of the 3D analysis through SCOOPS 3D. In our work, TRIGRS is used for the hydrological analysis. Then, the resulting pore pressure field is used first as input to the infinite slope stability model embedded into TRIGRS model itself, and then as input to SCOOPS 3D for the geomechanical analysis.

Though the present is not the first application of SCOOPS 3D methodology to a real case study (Tran et al., 2018; He et al., 2021), here it is applied to a case study where a detailed knowledge of the occurred landslide geometries is available, due to a post-event processing of aerial images. The use of the multi-objective optimization and the availability of detailed spatial information on observed landslides enable a more in-depth assessment of the concerned models as compared to the two above-cited studies.

First the proposed methodology is presented in the “Materials and Methods” section, focusing on the models adopted in the models (TRIGRS, version 2.1 (Alvioli and Baum, 2016); SCOOPS 3D, version 1.1 (Reid et al., 2015)) and on the genetic algorithm NSGAI (Non-dominated Sorting Genetic Algorithm II) used in the optimization of SCOOPS 3D. Then the “Study Area” section describes the relevant features of the study area. Next, a comparison of the performance of the 1D and 3D approaches is presented in “Results and Discussion” section. Finally, conclusions are drawn in the last section.

5.2. Materials and methods

The methodology adopted in this work aims to compare the performance of a 3D model vs. a 1D model in the prediction of landslide areas as a result of an intense rainfall event. This comparison requires a hydrological analysis to be performed as a preliminary step. In this work, this is done through the hydrological module of TRIGRS program, which uses a linearization of the 1D vertical infiltration Richards equation (see Section 5.2.1). Taking as input the pressure head fields of the hydrological analysis, the geomechanical analysis is performed using the infinite slope model implemented within TRIGRS (see Section 5.2.2) and the SCOOPS 3D model (see Section 5.2.3). While using the software SCOOPS 3D, a novel parameterization method based on the use of multi-objective optimization is proposed (see Section 5.2.4) in order to improve its prediction capability.

To test the performance of TRIGRS and SCOOPS 3D in terms of landslide prediction against observations in a real case study using the inventory of the occurred landslides geometries, the ROC analysis (Receiver Operating Characteristic) (Fawcett, 2006) is used. ROC curves show the full picture of the relationship between true-positive rate and false-positive rate across all possible threshold values (Liu et al., 2005), namely, in this case, the link between the probability to obtain a true-positive result in the class of the observed landslides and the probability to obtain a false-positive result in the class of not occurred landslides (Capparelli, 2012).

In more detail the performance of the models can be assessed through indices based on the confusion matrix or the receiver-operating characteristics (ROCs), that is, in terms of the count of true positives (TP), true negatives (TN), false positives (FP) and false negatives (FN) (e.g., (Marino et al., 2020)) (Table 4-I) in each cell of the domain.

Table 5-I Confusion matrix for ROC analysis.

		Observed landslide	
		Landslide (P)	No landslide (N)
Predicted Landslide	Landslide: FS<1	TP	FP
	No landslide: FS≥1	FN	TN

As a function of the variables reported in Table 4-I, the three reference standard ROC indices, namely, true positive rate, false positive rate and true skill statistic, are listed below (Eqs. 5.1,5.2, 5.3):

$$TPR = \frac{TP}{(TP + FN)} \quad (5.1)$$

$$FPR = \frac{FP}{(TN + FP)} \quad (5.2)$$

$$TSS = \frac{TP}{TP + FN} - \frac{FP}{TN + FP} \quad (5.3)$$

The highest performances correspond to FPR=0 and TPR=1, when, relatively to a given rainfall event, all observed landslide cells are equal to all unstable cells predicted by the model, i.e., model produces no false or missing predictions. A description of the methodology is presented in Figure 5.1. Additional remarks concerning the simulation framework are reported in subsection 5.3 “Simulation framework”.

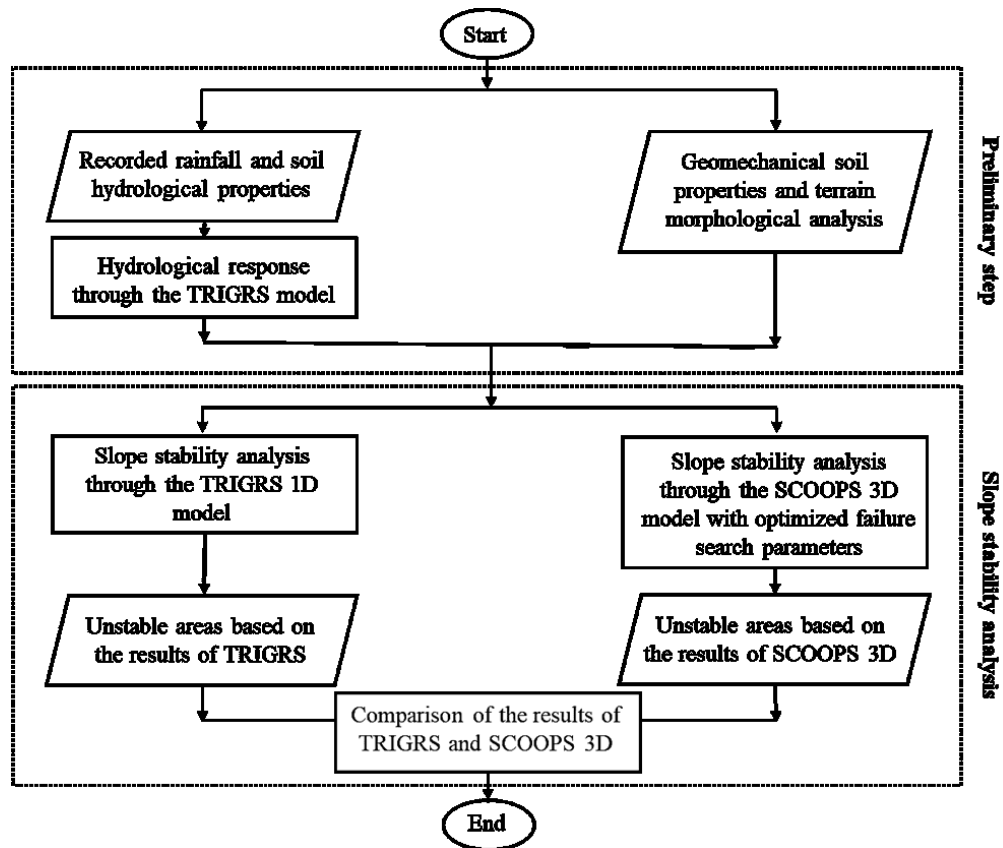


Figure 5.1 Description of the methodology.

5.2.1. Pressure Head Computation by TRIGRS Model (The Transient Infiltration and Grid-Based Regional Slope-Stability Model – v.2.1)

TRIGRS (Transient Rainfall Infiltration and Grid-Based Regional Slope-stability Model) is a research computational model developed by U. S. Geological Survey (USGS) to describe the timing and distribution of rainfall-induced shallow landslides (Rex L. Baum, William Z. Savage, 2008).

This is an event-based spatially-distributed model to assess the pore water pressures on a cell-by-cell basis and to outline variations in Factor of Safety (FS) resulting from extreme rainfall events that have durations ranging from hours to few days. Different outputs of the model can be displayed in a geographical information system (GIS) (Rex L. Baum, William Z. Savage, 2008) and can be

saved at multiple times during the simulation.

The software is founded on analytical solutions for Richards' one-dimensional (1D) partial differential equation representing the vertical subsurface flow in vertically isotropic and homogeneous material.

Version 1.0 of TRIGRS (Baum et al., 2002) was based on the hydrological model of Iverson (Iverson, 2000b) for a finite basal boundary bedrock depth by Savage et al. (Savage et al., 2003) whereas the version 2.0 and the version 2.1, which is used here, are based on less restrictive hypotheses than the previous version, i.e. an analytical solution to the Richards' vertical infiltration equation with a Gardner (Gardner, 1958) retention curve. A scheme for a simulated hillslope cell is shown in Figure 5.2, representing the soil profile as a system consisting of two layers with a saturated zone beneath the water table that is overlain by a capillary fringe in addition to an unsaturated zone extending to the ground surface (Rex L. Baum, William Z. Savage, 2008).

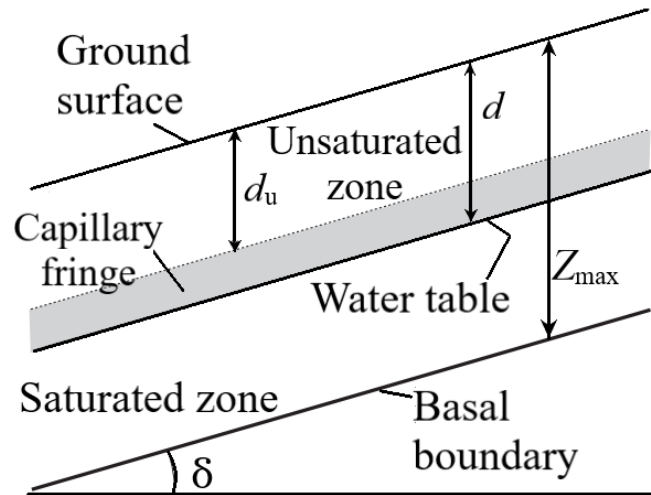


Figure 5.2 One-cell sketch for the TRIGRS model (Rex L. Baum, William Z. Savage, 2008)

For the simulation of the vertically rainfall infiltration at the ground surface through the unsaturated zone, the one-dimensional Richards equation is applied as follow:

$$\frac{\partial \theta}{\partial t} = \frac{\partial}{\partial Z} \left[K(\psi) \left(\frac{1}{\cos^2 \delta} \frac{\partial \psi}{\partial Z} - 1 \right) \right] \quad (5.4)$$

where Z is the vertical downward coordinate, t is the time, $\theta(Z, t)$ is the soil water content, $\psi(Z, t)$ is the pore pressure, $K(\psi)$ is the hydraulic conductivity and δ is the ground slope surface. According to Srivastava and Yeh (Srivastava and Yeh, 1991), Eq. (5.4) can be linearized using the exponential soil water retention curve proposed by Gardner (1958) described by the following equations:

$$K(\psi) = K_s e^{\alpha(\psi - \psi_0)} \quad (5.5)$$

$$\theta = \theta_r + (\theta_s - \theta_r) e^{\alpha(\psi - \psi_0)} \quad (5.6)$$

where K_s is the saturated hydraulic conductivity, α is the inverse height of the capillary rise, $-\psi_0 = 1/\alpha$ is the vertical height of the capillary fringe above the water table, θ_r and θ_s are the residual and saturated water contents, respectively. Using Eq. (5.5) and the computation of $K(Z, t)$ based on a generalized form of the solution of Srivastava and Yeh (1991), the pressure head in the unsaturated zone $\psi(Z, t)$ is obtained

$$\psi(Z, t) = \frac{\cos \delta}{\alpha_1} \ln \left[\frac{K(Z, t)}{K_s} \right] + \psi_0 \quad (5.7)$$

where δ is the ground surface slope and $\alpha_1 = \alpha \cos^2 \delta$.

Infiltration, runoff and flow routing

The infiltration at each cell of the domain, I , is evaluated as the sum of the precipitation rate P plus the runoff rate from the upslope cells, R_u , as long as the infiltration does not exceed the hydraulic conductivity K_s :

$$I = P + R_u \quad \text{if } P + R_u \leq K_s \quad (5.8)$$

$$I = K_s \quad \text{if } P + R_u \geq K_s \quad (5.9)$$

When the precipitation and the supplied runoff from adjacent cells exceed infiltrability, runoff R_d appears and is diverted flowing down to adjacent downslope cells. The distribution among the downslope cells is computed as follow:

$$R_d = P + R_u - K_s \quad \text{if } P + R_u - K_s \geq 0 \quad (5.10)$$

$$R_d = 0 \quad \text{if } P + R_u - K_s < 0 \quad (5.11)$$

Further details on the TRIGRS governing equations have been reported by Alvioli and Baum (2016); Baum and Savage (2008).

5.2.2. Slope Stability Analysis by TRIGRS Model (The Transient Rainfall Infiltration and Grid-Based Regional Slope-Stability Model – v.2.1)

Following Iverson (2000a), the slope stability analysis in TRIGRS is assessed under the infinite slope assumption, assuming failure plans parallel to the ground surface (Taylor Donald W., 1948). The factor of safety FS is computed on cell-by-cell basis for an arbitrary depth Z with the following formula:

$$S(Z, t) = \frac{\tan\phi'}{\tan\delta} + \frac{c' - \psi(Z, t)\gamma_w \tan\phi'}{\gamma_s Z \sin\delta \cos\delta} \quad (5.12)$$

where ϕ' is the soil friction angle for effective stress; c' is the soil cohesion for effective stress; γ_s and γ_w are the soil unit weight and the unit weight of groundwater, respectively; $\psi(Z, t)$ is the pressure head as a function of time t and of depth Z ; δ is the slope angle. Therefore, pressure head affects slope stability and, as shown by Eq. (5.12), an increase in pressures provides a decrease in the safety factor FS. In accordance with most of the studies, FS=1 is assumed as limiting equilibrium stadium for landslides triggering (Iverson, 2000b; Rosso et al., 2006; Baum and Godt, 2010; Peres et al., 2018; Peres and Cancelliere, 2018b), therefore the failure is predicted when FS<1 and stability holds where FS≥1.

It should be pointed out that TRIGRS, as it works on cell-by-cell basis, needs GIS software for preparing the necessary input gridded data in ASCII format. This allows investigating several scenarios by varying the geotechnical and hydraulic

parameters which could be assumed homogeneous in the whole study area or not.

5.2.3. Slope Stability Analysis by SCOOPS 3D Model (Software to Analyze Three-Dimensional Slope- Stability throughout a Digital Landscape)

SCOOPS 3D is a research computational model developed by U. S. Geological Survey (USGS) (Reid et al., 2015) which uses a three-dimensional method of columns approach for analyzing slope stability throughout a digital landscape (digital elevation model, DEM). This model utilizes a considerable number of spheres to cut the terrain in order to generate several intersections, corresponding to various potential slip surfaces (Fig. 4.3.3-1). For each potential slip surface, SCOOPS 3D applies the 3D limit equilibrium method (LEMs) to assess the slope stability. The use of spatially distributed spheres (Fig. 5.3) as predefined potential slip surfaces allows considering the three-dimensional characteristics of topography. These spatially distributed spheres can be user-defined by a series of model parameters.

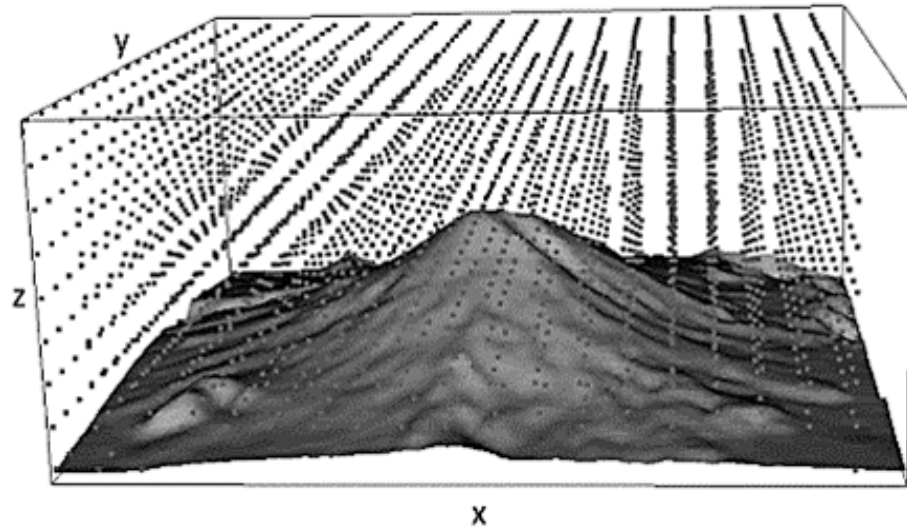


Figure 5.3 Diagram showing a 3D search lattice above a DEM. Each dot represents the center of multiple spherical trial surfaces (Reid et al., 2015).

SCOOPS 3D inspects the DEM for potential failure based on well-defined size criteria and a user-defined search grid assuming several soil layers with different properties and several groundwater inputs (dry, piezometric surface, pore-pressure ratio etc.). For a given trial surface, the three-dimensional factor of safety, FS_{3D} , is computed using two limit equilibrium methods: the Fellenius Ordinary method (1936) and Bishop's simplified method (1955). Being cell-by-cell computation method, each cell within the domain is analyzed by different trial surfaces until the lowest value of FS_{3D} is found. This means that, for each intersection, the FS_{3D} is uniformly distributed along the trial surface and the final slip surface for an individual landslide consists of many portions of spheres which represent the minimum stability for every cell. At the end of the research procedure, SCOOPS 3D generates a new terrain map with all the materials above the potential slip surface removed. Although the slope stability is related to the hillside deformations, only the balance of the involved forces is analyzed considering a rigid mass potentially sliding regardless of deformations and displacements. In general, all limit-equilibrium methods define the factor of safety as the ratio of the average shear resistance (strength), s , to the shear stress

τ , required to maintain limit equilibrium along a predefined trial surface:

$$F_{S3D} = \frac{S}{\tau} \quad (5.13)$$

As usual, in Eq. 5.13, the slope is considered unstable when $F_{S3D} < 1$.

Bishop's simplified method (1955) is the most conventional and diffused one since it provides reliable F_{S3D} results that are close to more recent and rigorous LEMs (Spencer, 1967; Hungr, 1987; Lam and Fredlund, 1993; Reid et al., 2015). It is based on the assumption according to which all forces acting on vertical faces of each column can be neglected in the equilibrium equations. In SCOOPS 3D, the same assumption is made for columns according to the method proposed by Hungr (1987) and the shear resistance, τ , acting on a potential slip surface in defined by Coulomb-Terzaghi law (Brien and Reid, 2007)

$$\tau = c' + (\sigma_n - u)\tan\varphi' \quad (5.14)$$

where c' is the soil cohesion, φ' is the angle of internal friction, σ_n is the total normal stress acting on the failure surface and u is the pore water pressure acting on the shear surface. So, the three-dimensional factor of safety is computed summing, for all columns within the potential failure surface, the F_{S3D} with the following formula:

$$F_{S3D} = \frac{\sum R_{i,j} [c_{i,j}A_{h_{i,j}} + (W_{i,j} - u_{i,j}A_{h_{i,j}})\tan\varphi_{i,j}] / m_{\alpha_{i,j}}}{\sum W_{i,j}(R_{i,j}\sin\alpha_{i,j} + k_{eq}e_{i,j})} \quad (5.15)$$

where, for the i,j column in a potential failure mass, $A_{h_{i,j}}$ is the horizontal area of the trial slip surface, $R_{i,j}$ is the distance from the axis of rotation to the center of trial slip area, $W_{i,j}$ is the weight, $u_{i,j}$ is the pore-water pressure, $c_{i,j}$ is the cohesion of the trial slip surface and finally $\varphi_{i,j}$ is the angle of internal friction on trial slip surface; $m_{\alpha_{i,j}}$ is a term for part of the computation of normal force acting on the

trial slip surface of the i,j column in a potential failure mass, used in Bishop's simplified method of analysis; k_{eq} and $e_{i,j}$ are terms related to the option to simulate earthquake or seismic loading effects (equal to 0 in this study). More details and a complete description of the SCOOPS 3D model are reported by Reid et al. (2015).

5.2.4. SCOOPS 3D Search Grid Configuration and Optimization by NSGAI Genetic algorithm

As explained in the previous section, SCOOPS 3D model utilizes a considerable number of spatially distributed spheres (defined by model parameters) to generate a number of trial surfaces. The set-up of the search grid is a crucial step in order to optimize the computational speed and to ensure high performance of the model, thus it needs to be systematically and efficiently configured. The following parameters require to be set for the SCOOPS 3D simulations:

- The radius increments Δ_r used to explore trial surfaces. The value of Δ_r is used to increase the radius of the spheres that create a series of trial surfaces ranging in size between the user specified minimum and maximum area of the potential slip surfaces. When the potential failure mass exceeds the maximum area or intersect a DEM boundary, the generation of the spheres with radius increment Δ_r is stopped.
- The minimum and the maximum elevation, $Z_{s,min}$ and $Z_{s,max}$, of the search-lattice nodes with respect to the DEM elevation. The elevation of the first search-lattice node is calculated as the sum of $Z_{s,min}$ and a multiple of $Z_{srchres}$ (a user defined parameter usually equal to the DEM resolution). So that, the lattice node being used is always above the DEM.
- The minimum and the maximum horizontal surface area limits, a_{min} and a_{max} , for potential failure masses. The area of a potential failure mass must fall in this range for a trial surface to be considered valid.

At the moment, no well-established procedures exist in the scientific literature for the parameterization of SCOOPS 3D. As an example, Tran et al. (2018) analyzed several ranges of the concerned parameters until no change was found on the predicted F_{S3D} map. Here, the search for the optimal parameters was thus carried out by using a multi-objective approach, namely the NSGAI multi-objective genetic algorithm (Deb et al., 2002).

Genetic algorithms are a heuristic search and optimization method inspired by natural evolution. The basic concept is that evolution will find an optimal solution for the analyzed problem after a number of successive generations, similar to natural evolution. Any genetic algorithm includes the following elements: the chromosome encoding (string representations of the decisional variables in each solution), the fitness function (computation evaluating the quality of the chromosome as a solution), selection (designed to use fitness to guide the evolution of chromosomes), recombination (recombination of selected chromosomes through crossover and mutation processes to form members of the offspring population) and the evolution scheme (iteration of the scheme until the stopping criteria are reached) (McCall, 2005). Due to its random nature, the genetic algorithm improves the chances of finding a global solution and proves to be very efficient and stable in searching for global optimum solutions (Bajpai and Kumar, 2010).

The NSGAI (Deb et al., 2002) is the second generation evolutionary multi-objective optimization genetic algorithm that improves the previous NSGA thanks to its novel features, namely: a more efficient non-domination sorting algorithm, no sharing parameter (i.e., the niche radius), and an implicitly elitist selection method that greatly aids in solving high order problems (i.e., problems with more than 2 objectives) (Reed et al., 2003). NSGAI is one of the most popular multi-objective optimization algorithms and, unlike the single objective optimization approach, it simultaneously optimizes various objective functions

(Yusoff et al., 2011). In NSGAI, a population of individuals featuring a number of genes equal to the number of decisional variables is considered. Like for the evolution of living organisms, the population of individuals evolves through processes of mutation and crossover, until they converge, in a certain number of generations, to the set of final solutions. This set will take the shape of a Pareto front or Pareto band, in the case of two or more than two objective functions. The diversity inside the Pareto front is ensured by means of the crowding distance, a parameter that encourages the spacing between the solutions in the front. NSGAI is an elitist algorithm, in that it prevents an undominated solution to be deleted from the front. Inside the Pareto front, indeed, no solution is better than any others, since all solutions are in the optimal trade-off between the two objective functions.

Thanks to the abovementioned features, the NSGAI genetic algorithm turns to be a suitable tool in order to thoroughly find the optimal search input parameters responsible for the failure surfaces search for SCOOPS 3D.

In more detail, the two objective functions considered for the present optimization problem are the True Positive Rate (Eq. (5.1)), and the False Positive Rate (Eq. (5.2)), to be maximized and minimized, respectively. The aforementioned SCOOPS 3D parameters Δ_r , $Z_{s,\min}$, $Z_{s,\max}$, a_{\min} and a_{\max} represent, on the other hand, the decision variables ranging between the minimum and the maximum constraints defined by the user.

Inside the Pareto front, the choice of the ultimate solution can be made using several criteria. As an example, the set of parameters that yields the expected performance in terms of one of the two objectives (either FPR or TPR) can be chosen. Otherwise, the set of parameters that yields the Pareto front solution closest to the theoretical performance of the best possible model (FPR=0 and TPR=1) can be chosen. Finally, another criterion lies in selecting the solution farthest up from the bisector line which corresponds to a totally random

prediction in a ROC plane.

In view of these considerations, a Matlab code was designed in order to implement the NSGAI optimization and to call and run SCOOPS 3D in a single routine. This avoided launching manually the model multiple times, with evident savings in terms of simulation time.

5.3. Simulation framework

The methodology described in the previous sections (Fig. 5.1) can be applied as follows for a generic case study, i.e., a certain catchment in which landslides occur during an intense rain event. In a preliminary step aimed at constructing the input of the slope stability analysis, on the one hand, the hydrological properties of the soil are evaluated together with the recorded rainfall data. On the other hand, the geomechanical soil properties are evaluated and the terrain morphological analysis is performed. Then, once the pore pressure field is computed through the TRIGRS model, the soil stability analysis is performed based on the following simulations:

- Simulation I: 1D slope stability analysis using the TRIGRS model;
- Simulation II: 3D slope stability analysis using the SCOOPS 3D model.

As for the first simulation, TRIGRS requires several hydrological soil properties (total unit weight of water γ_w , saturated hydraulic conductivity K_s , saturated hydraulic diffusivity D_0) and the soil water characteristic curve for wetting of the unsaturated soil (Gardner's parameter α , saturated volumetric water content θ_s , and residual volumetric water content θ_r). All the parameters of TRIGRS can be derived from in-situ measurements of the soil in the analyzed case study. In more detail, field surveys together with laboratory test results have enabled to derive the hydrogeological properties needed for the abovementioned simulations. The geotechnical characterization was based on standard soil analyses carried out according to the ASTM (American Society for Testing and

Materials) standards. The performed tests included an assessment of the physical parameters of the materials and triaxial tests which allowed the determination of the shear strength parameters. The hydrological properties in the study area, instead, were determined through a laboratory reconstruction of the soil water characteristic curve (SWCC) and the hydraulic conductivity function (HCF). These functions were reconstructed using undisturbed soil samples.

As for the second simulation, instead, in addition to the geotechnical and hydraulic properties, the hydrological data obtained from the TRIGRS model and the configuration of the search grid as a result of the optimization procedure through NSGAI genetic algorithm are required.

5.4. Study area

The study area is located in the Oltrepò Pavese, Lombardy region, northern Italy (Figure 5.4).

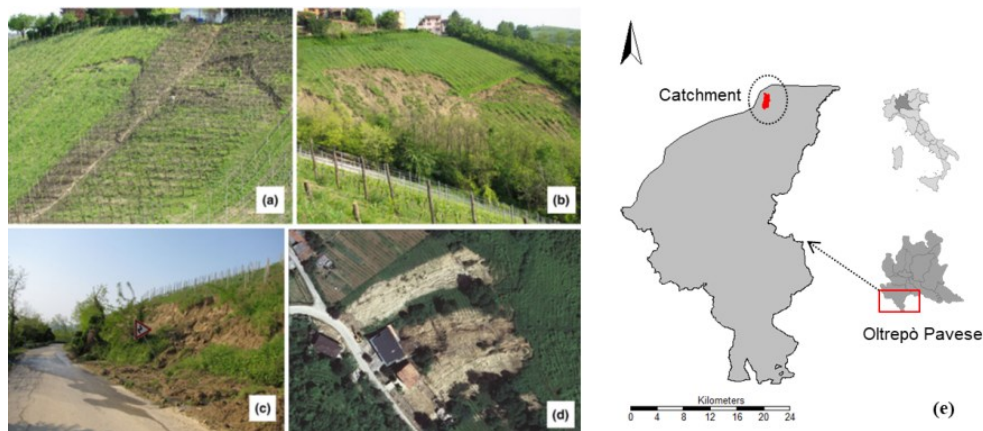


Figure 5.4 (a), (b), (c), (d) Examples of landslides in the study area (Valentino et al., 2014); (e) Catchment within Oltrepò Pavese region.

A catchment was selected with a surface area of about 2 km² where many shallow-seated landslides occurred due to rainfall on April 27–28, 2009 (Fig. 5.5(a)). Based on aerial photographs taken immediately after the event and subsequent field surveys, the shapes of the observed landslides were individuated and inventoried. Observed landslides featured very variable size,

ranging from about 15 m² to 6300 m² with an average value of 500 m². The distribution of terrain slope of the catchment is also shown in Figure 5.5(b).

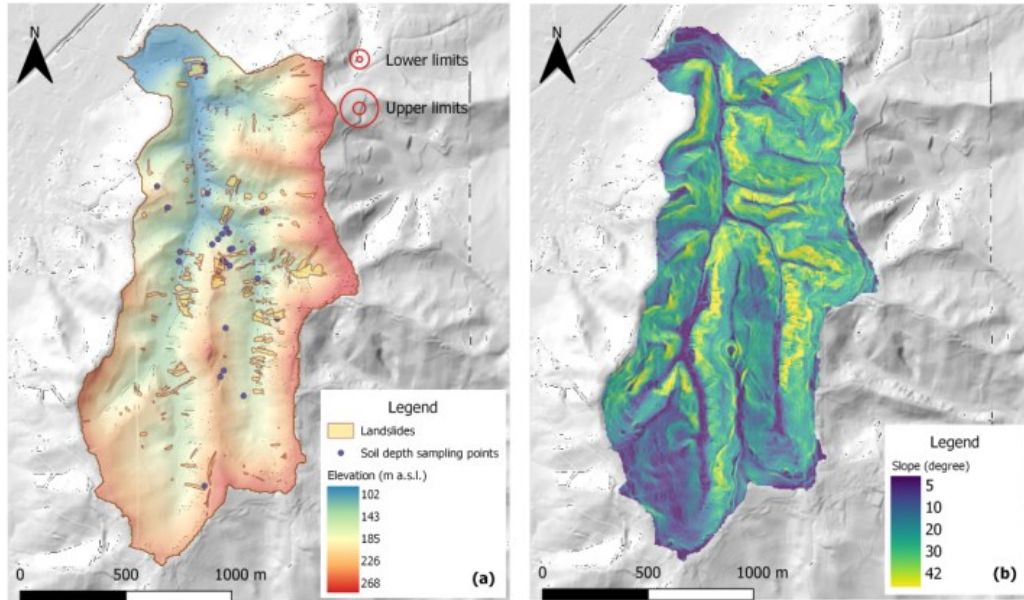


Figure 5.5 (a) Catchment topography with observed landslides triggered after the extreme rainfall on April 27-28, 2009 and location of soil thickness sampling points. Maximum and minimum areas (a_{min} , a_{max}) considered as lower and upper limits in the optimization process of the slip-surface search parameters for SCOOPS 3D are also represented; (b) Catchment slope.

One crucial step in the application of the TRIGRS model is the definition of the initial conditions, mainly the finite depth of the basal boundary (that is the covering soil above of the impermeable bedrock) and the depth of the water table, both referred to the ground surface. To this end, generally steady state initial conditions are assumed. Here, it was assumed that the water table had an upper limit located approximately 0.1 m above the bedrock, accordingly to the in situ measurements collected by a monitoring station installed in the study area after the event taken as reference (Bordoni et al., 2015c). In more detail, some probes were installed in the soil at different depth to measure some of the main hydrological features such as the soil water content and the soil water pressure. The thickness of the basal boundary, instead, can vary as a function of many different and interplaying factors, such as the underlying lithology, the slope

gradient, the hillslope curvature, the upslope contributing area, and other factors (Tesfa et al., 2009). Since many applications require the availability of soil thickness measures on a dense scale, several methods for estimating the spatial patterns of soil thickness have been proposed in the scientific literature (Salciarini et al., 2006; Tesfa et al., 2009; Pelletier and Rasmussen, 2009; Catani et al., 2010). In this application the empirical method proposed by Saulnier (1997) has been adopted according to which the effective soil depth is defined as a function of the slope angle within the catchment (Tran et al., 2018; Méndez-Barroso et al., 2016)

$$y_i = y_{\max} \left[1 - \frac{\tan(x_i) - \tan(x_{\min})}{\tan(x_{\max}) - \tan(x_{\min})} \left(1 - \frac{y_{\min}}{y_{\max}} \right) \right] \quad (5.16)$$

where y_{\min} and y_{\max} are, respectively, the minimum and the maximum values of effective soil depth, and x_i is the slope angle at point i . The minimum and the maximum values of soil thickness were derived from field data collected after the event investigated in this study (Zizioli et al., 2013) (Table 4-II).

The location of the measuring points concerning the soil thickness used for the computation of the distribution of the soil depth within the study area is also reported in Figure 5.5(a) and the correlation between measured soil thickness points and the estimated ones is shown in Figure 5.6.

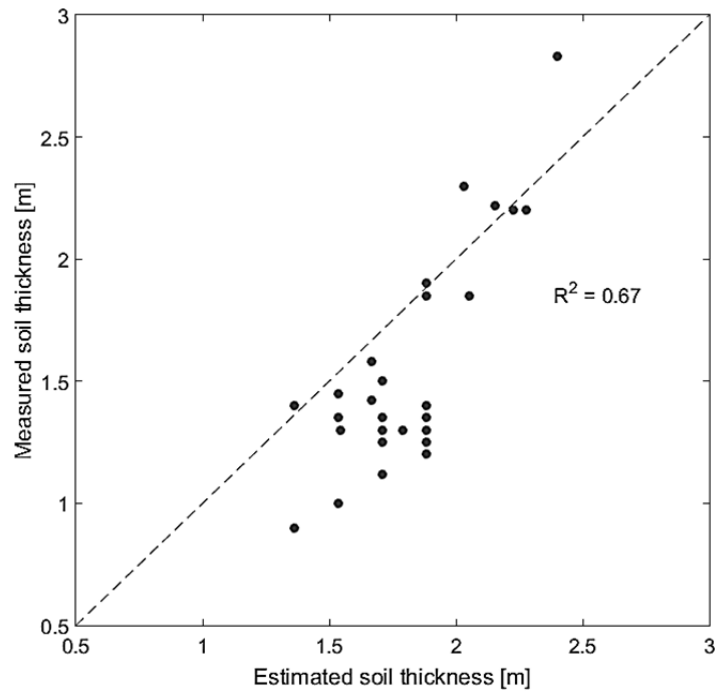


Figure 5.6 Measured vs. estimated soil thickness points.

During the mentioned landslide event dates, the Cigognola rain-gauge station recorded 160 mm of rain in 48 hours (20% of the annual average amount), with a peak intensity of 22 mm/h at 09:00 p.m. on 27 April. After this maximum intensity was reached, many shallow landslides were triggered, causing one fatality, several damages to agriculture, and road blockages (Zizioli et al., 2013).

The geotechnical and hydraulic properties in the study area are summarized in Table 4-II. For a more detailed description of the geological features of the study area, please refer to Bordoni et al. (2015c).

Table 5-II Geotechnical and hydraulic properties for the study area (Bordoni et al., 2015c; Zizioli et al., 2013).

γ_s	φ'	c'	θ_s	θ_r	α_G	K_s	D_0	y_{max}	y_{min}
[kN·m ⁻³]	[°]	[kPa]	[-]	[-]	[kPa ⁻¹]	[m·s ⁻¹]	[m·s ⁻¹]	[m]	[m]
18	26	3.8	0.46	0.08	0.014	$1.4 \cdot 10^{-5}$	$2.8 \cdot 10^{-4}$	2.4	0.5

Lastly, Table 5-III summarizes the minimum and maximum constraints concerning the decision variables used in the optimization process of the slip-surfaces search parameters for SCOOPS 3D. These values were set based on some

practical considerations available in SCOOPS 3D reference book (Reid et al., 2015).

Table 5-III Decision variables constraints used in the optimization process of the slip-surfaces search parameters for SCOOPS 3D.

	$z_{s,min}$	$z_{s,max}$	a_{min}	a_{max}	$\Delta_r, increment$
	[m]	[m]	[m ²]	[m ²]	[m]
Lower limit	100	300	500	6300	0.25
Upper limit	200	600	2500	25000	25

The results of the slope stability analysis in Simulations I and II were considered at the time step of the maximum rainfall intensity, namely, 9 p.m. on April 27, 2009, when the most devastating landslides were triggered (Valentino et al., 2014).

5.5. Results and discussion

Figure 5.7 shows the spatially-averaged max pressure head (panel (b)) and the amount of potential unstable cells (panel (c)) within the study catchment during the rainfall event (panel (a)) as a result of the 1D slope stability analysis (simulations by TRIGRS software v. 2.1). It can be noted that the number of cells corresponding to a factor of safety $FS_{ID} < 1$ increases with total rainfall.

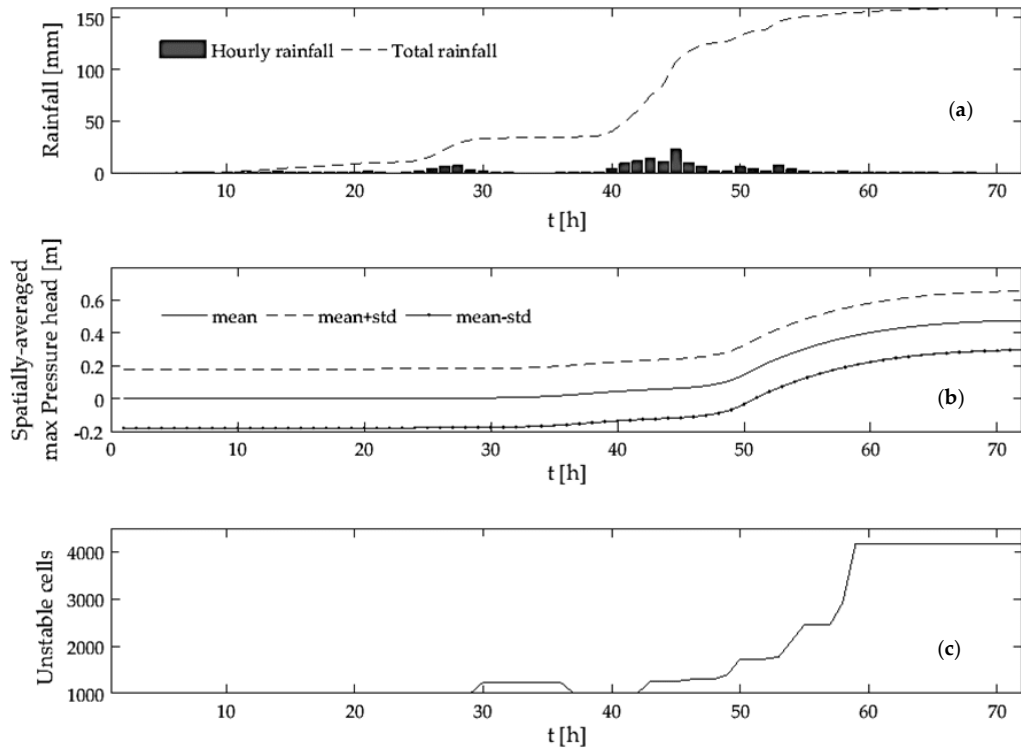


Figure 5.7 (a) Hourly rainfall series used in input for simulations; (b) simulated catchment-averaged pressure head series; (c) simulated potential unstable cells for the event of April 27-28, 2009 (1D analysis using TRIGRS v. 2.1)

Figure 5.8 shows, in terms of FPR and TPR, the results of the comparison between 1D and 3D slope stability analysis as output of the two main simulations carried out. As expected, the output of TRIGRS is made up of a single pair of values FPR and TPR. The output of SCOOPS 3D is, instead, made up of a Pareto front of optimal solutions in the trade-off between FPR and TPR.

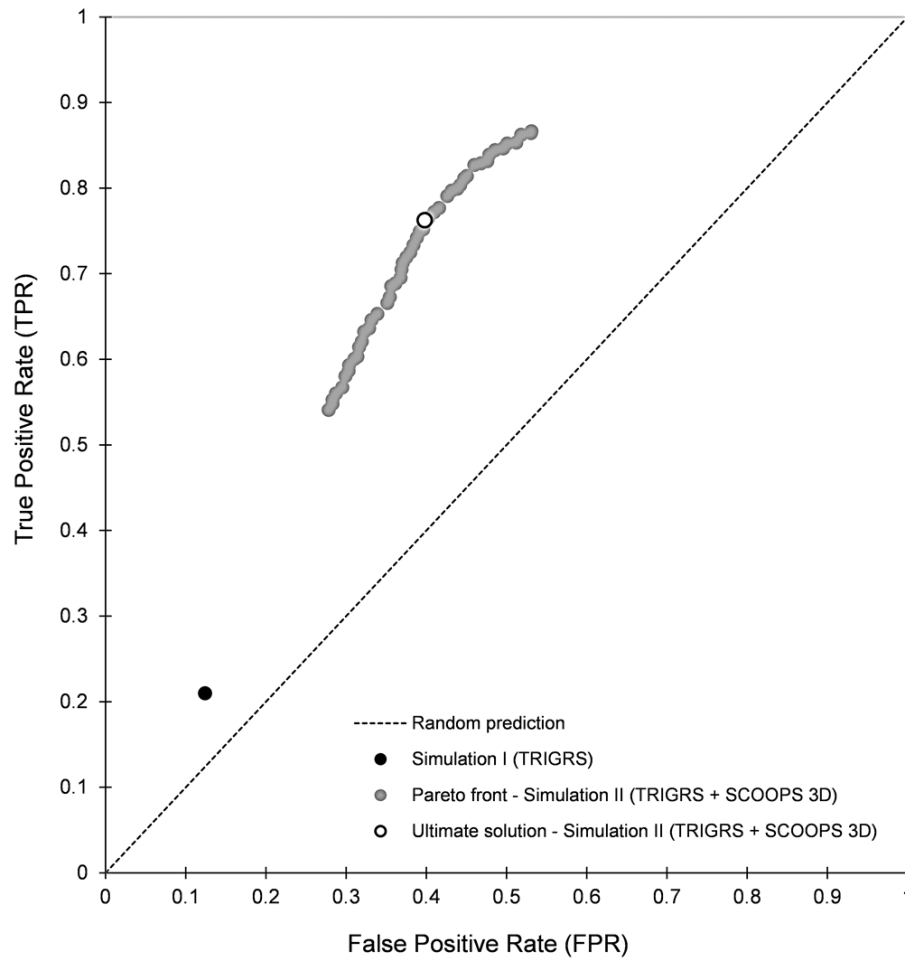


Figure 5.8 Comparison of the results of TRIGRS and SCOOPS 3D in the FPR-TPR space. Selection of the ultimate solution of SCOOPS 3D is also reported.

The figure shows that, in general, the 3D approach gives better results than the 1D method in terms of model performance, demonstrating that the 3D approach is able to better describe the landslide triggering mechanisms through the assumption of more realistic slip surface geometries. Although the point in the ROC plane corresponding to 1D analysis is higher than the line of no discrimination (random prediction), it lies significantly below the points corresponding to all 3D simulations, i.e., independently from the choice of the slip-surface searching parameters. The Pareto front representative of the simulation II features TPR values ranging between 0.54 and 0.87 and FPR values ranging between 0.28 and 0.53. In particular, if two extreme points are considered

within the ROC plane, namely a) $TPR=FPR=0$ (no unstable areas predicted by the model - most extreme underestimation of landslide area) and b) $TPR=FP =1$ (no stable areas predicted by the model - most extreme overestimation of landslide areas), as shown in Figure 5.8, the point representing the performance of the TRIGRS model is closer to the extreme condition a) than SCOOPS 3D model to the condition b). This means that, by using SCOOPS 3D, it is more likely to exactly predict unstable areas than to obtain a false positive result in the class of not occurred landslides.

The wide range of performance variation associated with the different values of the slip-surface search parameters highlights the importance of their correct choice, and thus of the optimization performed. Among the solutions in the Pareto front, the best can be assumed as the one closest to the ideal performance point ($FPR=0, TPR=1$), which is $FPR=0.39$ and $TPR=0.76$ (True Skill Statistic = $TPR - FPR = 0.37$).

The results described above in terms of FPR and TPR are reported in the following Table 5-IV as well as the optimized value of the slip surfaces search parameters for SCOOPS 3D in correspondence with the ultimate solution of simulation II.

Table 5-IV Ultimate values of the objective functions FPR and TPR in Simulations I and II and corresponding responses of the True Skill Statistic (TSS). Optimized values of the slip-surfaces search parameters for SCOOPS 3D are also reported.

	FPR	TPR	TSS	$Z_{s,min}$	$Z_{s,max}$	a_{min}	a_{max}	Δ_r, increment
	[-]	[-]	[-]	[m]	[m]	[m ²]	[m ²]	[m]
Simulation I	0.12	0.21	0.09	-	-	-	-	-
Simulation II	0.39	0.76	0.37	100	300.5	596	16074	21

The results of the analysis conducted in terms of factor of safety FS are shown in Figure 5.9. In more detail, Figures 5.9 (a) and (b) present the spatial distribution of the factor of safety as a result of both simulations carried out. According to Eqs. (5.12, 5.13), the potentially unstable cells are defined by a $FS < 1$, namely the

dark red cells of the maps. As expected, the 1D slope stability analysis, i.e., simulation I, yield a more disconnected field of the FS, if compared to the FS_{3D} distribution, i.e. simulation II. This reflects the fact that, for the infinite slope assumption, the possible failure of each cell within the study area is independent of the other ones, neglecting connectivity of the real failures.

For a more objective comparison between the two maps, the conditional distributions of the factor safety, respect to observed landslide and stable areas have been computed, and represented as cumulative empirical frequency plots in Figure 5.9 (c). As can be seen, the 3D model is able to better distinguish stable from unstable conditions, with a general higher cumulative frequency and factor of safety values ranking from 0.5 to 1.2 in the case of the observed landslides and until 2.5 in the case of no landslide occurrence. Relatively to the 1D model, instead, lower cumulative frequencies are accompanied by a missing clear discrimination in terms of factor of safety between the areas interested by the observed landslides and the remaining part of the study area, as depicted by the dashed lines in Figure 5.9 (c).

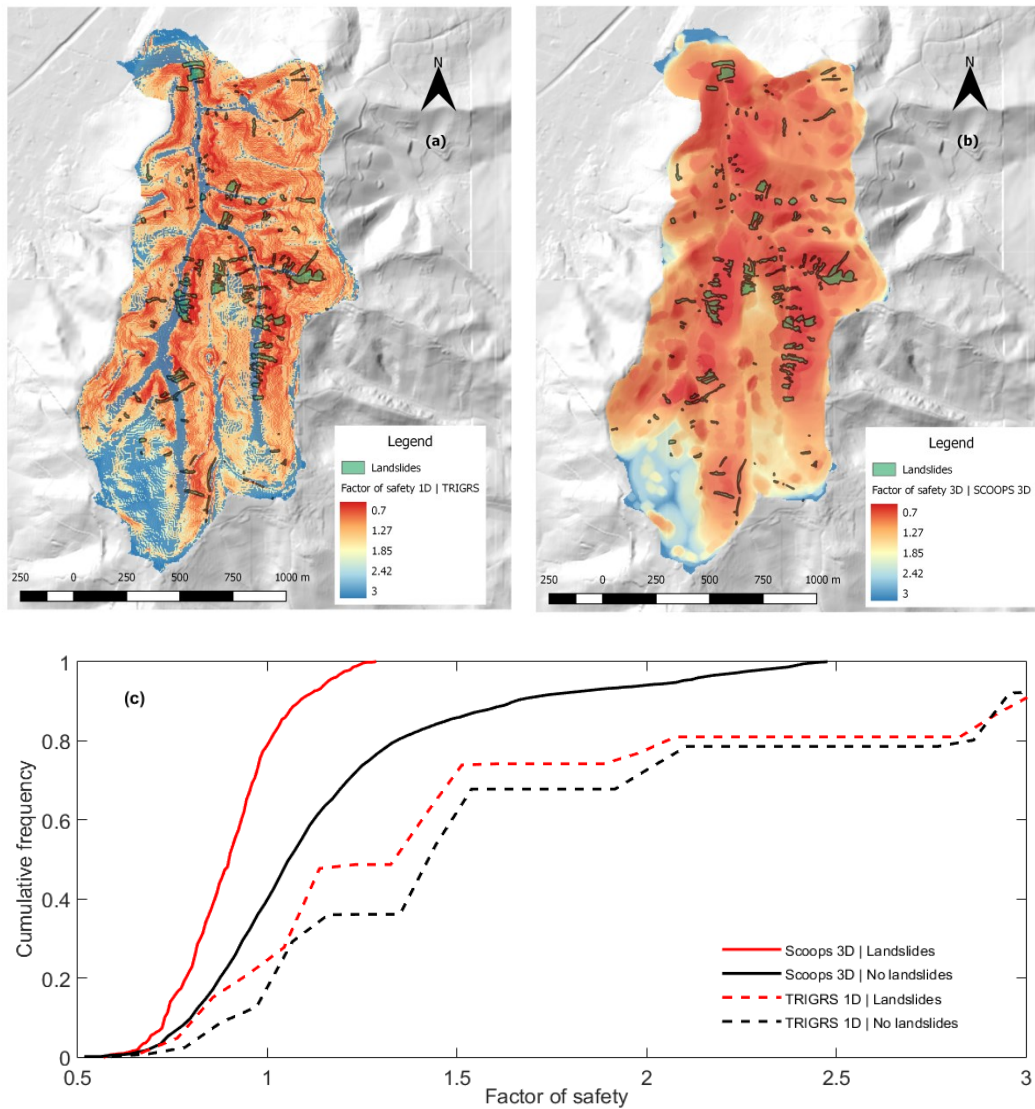


Figure 5.9 (a) Factor of safety spatial distribution as a result of 1D slope stability analysis (Simulation I); (b) Factor of safety spatial distribution as a result of 3D slope stability analysis (Simulation II); (c) Cumulative frequency of the factor of safety resulting by both 1D and 3D models

Furthermore, in order to evaluate the performance of the landslide models adopted in this paper, the landslide ratio of each predicted FS class was used, namely the LR_{class} index (Park et al., 2013). LR_{class} index is defined as the ratio of the percentage of contained slope failure locations in each FS class to the predicted percentage of area in each class of FS category. A larger value of $\%LR_{class}$ corresponds to a lower over-prediction by the model (Park et al., 2013). Table 5-V shows the results obtained concerning the LR_{class} analysis to allow an

additional comparison with Tran et al. (2018). The unstable areas predicted are 37.5% by the 3D method and 12.8% by the 1D method. The %LR_{class}=82 of the 3D approach is pretty higher than %LR_{class}=64.5 of the 1D method.

Table 5-V Comparison of LR_{class} index obtained with the 3D and 1D approaches, both calculated at 9 p.m. on 27 April, 2009.

FS class	Observed sites (a)		Observed sites (%) (c)		Predicted area (%) (d)		LR _{class} (e)=(c)/(d)		%LR _{class} (e)/(f)	
	3D	1D	3D	1D	3D	1D	3D	1D	3D	1D
FS < 1	2365	676	73.4	21	37.5	12.8	1.9	1.6	82	64.5
FS ≥ 1	857	2546	26.6	79	62.5	87.2	0.4	0.9	18	35.5
Sum	3222	3222	100	100	100	100	2.3 (f)	2.5 (f)	100	100

Overall, these results show that there is a large uncertainty in landslide prediction. On this regard, it is worthwhile to compare the performance we obtained with similar studies in the literature. In particular, relatively to the 1D model, Baum et al. (Baum et al., 2010) showed performance of the TRIGRS model for a study area north of Seattle, Washington in terms of ROC statistics, reporting a FPR = 0.08 and a TPR = 0.35 which are better than in our case (FPR = 0.12 and TPR = 0.21), likely for the availability of more detailed geological data than in our case. If we compare our results with those of Tran et al. (2018), in terms of the %LR_{class} index for FS<1, again we find better performances for the 1D model (85.6% vs. 64.5% in our case), while for the 3D model we obtain only slightly worse performances (87.4 vs. 82%). From another standpoint, this comparison, reveals a greater gain in performance when passing from the 1D to the 3D model. When comparing our results to those of He et al. (He et al., 2021), again in terms of the %LR_{class} index for FS<1, the results for the 1D model are closer (71.28% vs. our 64.5 %), while we obtain slightly better performances for the 3D model (82% in our case, vs. 80.16 %). The greater gain in performances from 1D to the 3D that we obtain demonstrates the success of the optimization process we propose.

5.6. Conclusions

This work presented the comparison of 1D (TRIGRS) and 3D (SCOOPS 3D) slope stability models combined with the hydrological analysis performed with the former software. The applications concerned the simulation of the landslides triggered by an intense rain event, with 160 mm in 48 h, in the Oltrepò Pavese in the year 2009.

Compared to other case studies in the scientific literature, this paper is the first, to the best of our knowledge, where SCOOPS 3D is tested against a detailed inventory of observed landslides with accurately measured shapes. This resulted in a more accurate evaluation of the modelling performance and in the opportunity to set up a more reliable model parameterization, obtained through the application of multi-objective optimization in the trade-off between true positive rate (TPR) and false positive rate (FPR), to be maximized and minimized respectively.

Overall, the analysis of the results has pointed out that SCOOPS 3D can enable better prediction of landslide prone areas, leading to TSS values up to 0.37, in comparison with a value of 0.09 for the 1D model TRIGRS. In comparison to other studies, we find the 1D model performs worse than in other studies, likely for the availability of less detailed geological data. On the other side, for the 3D model we find even better results than the two other studies present to date in the scientific literature. This is to be attributed to the optimization process we proposed, which allows to have a greater gain of performance passing from the 1D to the 3D simulation, in comparison to the above-mentioned studies, where no optimization has been applied.

Thus, our study contributes to improving the performances of landslide models, and marks out the way for future developments, e.g., the refinement of the computation of the hydrological response, required by the 3D slope stability analysis, by introducing soil moisture information.

In this regard, the use of soil moisture global dataset can be explored for deriving the initial conditions for modeling rainfall infiltration leading to shallow landsliding.

Chapter 6

Post-Failure Dynamics of Rainfall-Induced Landslide in Oltrepò Pavese

Manenti, S., Amicarelli, A., Palazzolo, N., Bordoni, M., Creaco, E., Meisina, C.

Abstract

Prediction of landslide hazard risk at hill slope induced by intense rainfall requires the appropriate modeling of the interactions between soil and weather phenomena, leading to failure as well as a reliable prediction of post-failure dynamics. In the peculiar case of fast shallow landslides behaving like dense granular flows, a suitable modeling approach for large and rapid deformations is necessary to estimate potential related damage. The impact force exerted by the leading edge of the earth-flow on the downstream structure should be estimated for both damage prediction and design of effective protection measures. In this paper, a free open-source 3D research code (Amicarelli et al. 2020b) based on standard weakly compressible smoothed particle hydrodynamics (WCSPH) method is validated on a full-scale rainfall-induced shallow landslide which occurred in Oltrepò Pavese (Northern Italy). SPHERA allows resolving the vertical velocity gradients, potentially providing a more reliable representation of the landslide dynamics and impact force. Mechanical parameters are consistent with average soil characteristics, avoiding calibration analysis. The final landslide profile is compared with an experimental survey for validation, showing good fit. Influence of uncertainties of geotechnical parameters on the landslide front velocity and impact force on the downstream wall is evaluated.

Keywords: rainfall-induced shallow landslide; post failure dynamics; soil-water interaction; validation; non-Newtonian fluid; WCSPH; natural hazards

6.1. Introduction

Post-failure shallow landslide dynamics may be characterized by opposite behaviors. In the case where low displacement rates occur at a narrow shear zone just below the ground surface, some simplified mathematical approaches may be adopted in the engineering practice to describe effectively the landslide dynamics (Conte et al., 2017). In the case of fast rainfall-induced shallow landslides, the dynamics is more complex to predict if the run-out starts as shallow rotational-translational failure subsequently changing into earth-flows. This kind of landslide is triggered by intense rainfall events inducing water infiltration at slopes that increases the volumetric water content and pore water pressure, thus worsening the slope stability (Zizioli et al., 2013). Therefore, a reliable assessment of landslide susceptibility requires, among the other things, proper definition of the hydro-mechanical features, as well as rainfall characteristics considering recent climate trends affecting rainfall and intense storm events (Barbero et al., 2014). A rainfall-induced shallow landslide represents one of the most common natural hazards in some areas of the world (Bordoni et al., 2015b, c). Ongoing research is being carried out for defining a new integrated hydrogeological model to assess shallow landslides and flood prone areas at catchment scale in Oltrepò Pavese, in order to predict their spatial and temporal occurrence, and to develop early-warning strategies (ANDROMEDA project, funded by Fondazione Cariplo) (Bordoni et al., 2019). The above-described dynamic behavior of fast rainfall-induced shallow landslide is due to the large water content. As a consequence, this kind of landslide behaves like a dense granular flow, and suitable modeling approaches should be adopted for handling large spatial and temporal displacement gradients. Meshless particle methods could be helpful for this purpose. Among the numerous types of meshless particle methods, the smoothed particle hydrodynamics (SPH) method (Monaghan, 2005) is successfully applied to simulate complex multiphase flows with impact and

shock (Guandalini et al., 2015; Manenti et al., 2011a), involving fluids with high-density ratio (Manenti et al., 2018) as well as non-Newtonian fluids (Manenti et al., 2016, 2011b; Guandalini et al., 2012; Shao and Lo, 2003). These problems are of great concern in the applied engineering dealing with water related natural hazards (Manenti et al., 2019), such as landslide induced tsunami in artificial reservoir (Manenti et al., 2016) and intense rainfall-induced shallow landslides (Pastor et al., 2004). The weakly compressible smoothed particle hydrodynamics (WCSPH) research code SPHERA v.9.0.0 (RSE SpA) (<https://github.com/AndreaAmicarelliRSE/SPHERA>) is a free open-source research software (FOSS) featured by several numerical schemes, such as the scheme for dense granular flows (Amicarelli et al., 2017). SPHERA has been validated on various application fields including, for instance, floods with transport of solid bodies and bed-load transport; fast landslides and their interactions with water reservoirs; sediment removal from water bodies (Amicarelli et al., 2020b). The validation of SPHERA on the post-failure dynamics of rainfall-induced fast shallow landslide will be illustrated in this work. In the analysis for a reliable estimate of the risk level of rainfall-induced landslide hazard, the susceptibility evaluation represents only one of the relevant issues. In fact, relevant dynamic features of landslide run-out, such as width and length of damage corridor, travel velocity, characteristic depth of both moving mass and deposit, should be properly assessed in order to provide a quantitative estimate of the hazard and select appropriate protective measures for risk mitigation (Dai et al., 2002). This target may be achieved through the adoption of reliable predictive models providing quantitative information on the destructive potential of the landslide. There are several approaches that have been successfully adopted for the post-failure dynamic analysis of fast shallow landslides. In the work of (Stancanelli et al., 2017), the post-failure flow model simulates the moving landslide as single-phase continuum through FLO-2D

commercial software that solves numerically the depth-integrated flow equations with the finite volume approach. The SPH model in (Pastor et al., 2009) allows one to predict the path, velocity, and depth of flow-like landslides following a two-phase approach where the mixture is made up of a solid skeleton with the voids filled by a liquid phase. The mixture dynamics is described by quasi-Lagrangian depth integrated governing equations of mass and momentum balance, and the pore pressure dissipation equation. The model was used to reproduce a catastrophic event occurred on May 1998 in the Campania region (Italy), showing the relevant role of geotechnical parameters (especially the fluid phase and angle of internal friction) for the reliable prediction of the run-out distance, velocity, and height of the landslide. A proper selection of the values assigned to these parameters assured the best agreement with the field observations. When the initial average depth is comparable with the horizontal length and width of the collapsed soil, as in the present case, significant variations in both thickness and vertical velocity profile may occur along the flow direction, advising against the adoption of depth-integrated models. Furthermore, a numerical model that does not require the calibration of relevant parameters in the landslide post-analysis may be used for run-out prediction in a risk analysis. In this work, the shallow landslide is simulated with the 3D code SPHERA (Amicarelli et al., 2020b) that allows resolving the velocity gradient in the vertical direction, potentially providing a more reliable representation of the landslide dynamics and impact force. No tuning of the relevant geotechnical parameters has been carried out to reproduce the final landslide profile with suitable accuracy. The impact force on the vertical downstream wall can be calculated for both quantitatively evaluating landslide risk level and supporting the design of protective structures. The following Section 6.2 illustrates briefly the relevant features of the numerical model SPHERA (Amicarelli et al., 2020b) and the case study. Section 6.3 presents and discusses the simulations results,

including: the model validation on a full-scale rainfall-induced shallow landslide; the effects of uncertainty of the relevant geotechnical model parameters (i.e., angle of internal friction ϕ , effective porosity e and solid phase density ρ_s) on the leading front celerity and impact force on the downstream wall. Conclusions are illustrated in Section 6.4.

6.2. Model description and Test Case Configuration

SPHERA v.9.0.0 (Amicarelli et al., 2020b) holds several numerical schemes, among which an SPH formulation of mixture model for the analysis of dense granular flows consistent with the kinetic theory of granular flow (KTGF). Those features of this scheme relevant for the present study are summarized in the current section; for a complete description, the reader is referred to (Amicarelli et al., 2017). The 3D fluid dynamics of both water and soil mixture is obtained by solving numerically the mass and momentum balance equations that are discretized according to standard WCSPH formulation:

$$\begin{aligned} \left\langle \frac{d\rho_i}{dt} \right\rangle &= -\rho_i \sum_{j=1}^N \frac{m_j}{\rho_j} (\mathbf{u}_j - \mathbf{u}_i) \cdot \nabla W_{ij,h} + \mathbf{B}_\rho \\ \left\langle \frac{d\mathbf{u}_i}{dt} \right\rangle &= -\frac{1}{\rho_i} \sum_{j=1}^N \frac{m_j}{\rho_j} \left(p_i + p_j + \frac{\Pi_{ij}}{\rho_i} \right) \nabla W_{ij} + \frac{\nabla \cdot \boldsymbol{\tau}_i}{\rho_i} + \mathbf{g} + \mathbf{B}_u \end{aligned} \quad (6.1)$$

In the Eqs. (6.1) the symbols assume the following meaning: \mathbf{u} mixture velocity; \mathbf{g} gravity acceleration; \mathbf{B}_ρ and \mathbf{B}_u boundary contributions for mass and, respectively, momentum balance equations according to semi-analytic approach (Di Monaco et al., 2011); c mixture pressure; m particle mass; ρ mixture density; W_{ij} compact supported central kernel function of the relative distance between a generic fluid particle, denoted by index i , and each one of the N neighbouring particles, denoted by index j ; Π_{ij} Monaghan (2005) artificial viscosity term used for the fluid phase solely. The divergence of the mixture viscous stress tensor $\boldsymbol{\tau}$ in the momentum balance (for the mixture solely) is computed as a function of the

strain rate tensor \mathbf{D} through the apparent viscosity μ_{fr} depending on the effective stress σ' , the second invariant of the strain rate tensor II_D and the angle of internal friction of soil φ :

$$\begin{aligned} \nabla \cdot \boldsymbol{\tau}^s &= \nabla \cdot (2\mu_{fr}\mathbf{D}) \\ \mu_{fr} &= \frac{\sigma' \sin \varphi}{2\sqrt{II_D}} \end{aligned} \quad (6.2)$$

The time integration is carried out through second-order Leapfrog scheme calculating the velocity of each particle at mid time-step with respect to both position and density (Amicarelli et al., 2015a). As the numerical scheme for the solution of discretized mass and momentum balance equations is explicit, the following stability condition must be satisfied for the integration time step dt (Amicarelli et al., 2015a):

$$dt = \min \left\{ C_v \frac{2h^2}{\mu/\rho}; \quad CFL \frac{2h}{c+|\mathbf{u}|} \right\} \quad (6.3)$$

In Eq. (6.3) h denotes the smoothing length related to particle size dx , c is the sound speed and CFL denotes the Courant–Friedrichs–Lewy number. A severe time step reduction occurs caused by the viscosity stability condition when shear rate comes close to zero and the apparent viscosity approaches higher values according to pseudo-plastic behavior (second of Eqs. 6.2). To avoid the unbounded growth of both mixture viscosity and computational time at very low shear rate, the maximum (or threshold) viscosity μ_{max} is introduced with a physical meaning (Amicarelli et al., 2017). When approaching to zero shear rates those mixture particles with an apparent viscosity higher than the maximum viscosity are considered in the elastic–plastic regime of soil deformation where the kinetic energy of solid particles is relatively small and the frictional regime of the packing limit in the KTGF does not apply. In this condition, the maximum viscosity is assigned to those particles that are excluded from the SPH

computation and considered as fixed particles. When these particles fall inside the neighbor list of a nearby moving particle, suitable physical properties are assumed. The value of the maximum viscosity does not require tuning or calibration. For a specific problem, the value assigned to the maximum viscosity is the smallest value that does not influence the numerical results appreciably. Any increase above this value would only affect the computational time through a reduction of the time step (Eq. 6.3). This procedure is described in section 6.4.1.

By analogy with the experimental behavior of high polymer solutions, the transition from the frictional regime (i.e., solid particle in motion) to the elastic-plastic regime (i.e., solid particle at rest) can be reproduced within a limiting region in the flow curve that is characterized by a constant value of the apparent viscosity referred to as limiting viscosity μ_0 . The limiting viscosity acts as a numerical parameter (Manenti et al., 2018). The value assigned to viscosity μ_0 should be evaluated through an optimization procedure leading to the definition of the lower value of the limiting viscosity to obtain a suitable accuracy in the results. This approach was successfully tested against a 2D laboratory experiment reproducing, along a representative transversal section of the artificial basin, the run-out of the 1968 Vajont landslide on the left-hand slope (Manenti et al., 2018). By taking into account landslide interaction with the water (both stored in the artificial basin and filling the saturated landslide portion) the scheme of SPHERA for dense granular flows (Amicarelli et al., 2017) allowed predicting maximum wave run-up with both suitable accuracy and significant reduction in the computational time.

In the present work, the cited scheme is validated on the post-failure analysis of a rainfall induced shallow landslide. This landslide occurred during an intense rainfall event on April 2009 in a hilly area of the Oltrepò Pavese named Recoaro valley (North-western part of Italy). Even if SPHERA is a 3D code, its simpler and faster 2D execution has been conveniently chosen for this case: as the

landslide is relatively narrow in the transversal direction, in the upper and mid parts of the domain the flow may be assumed as two-dimensional in the longitudinal vertical plane (Fig. 6.1 (a)).

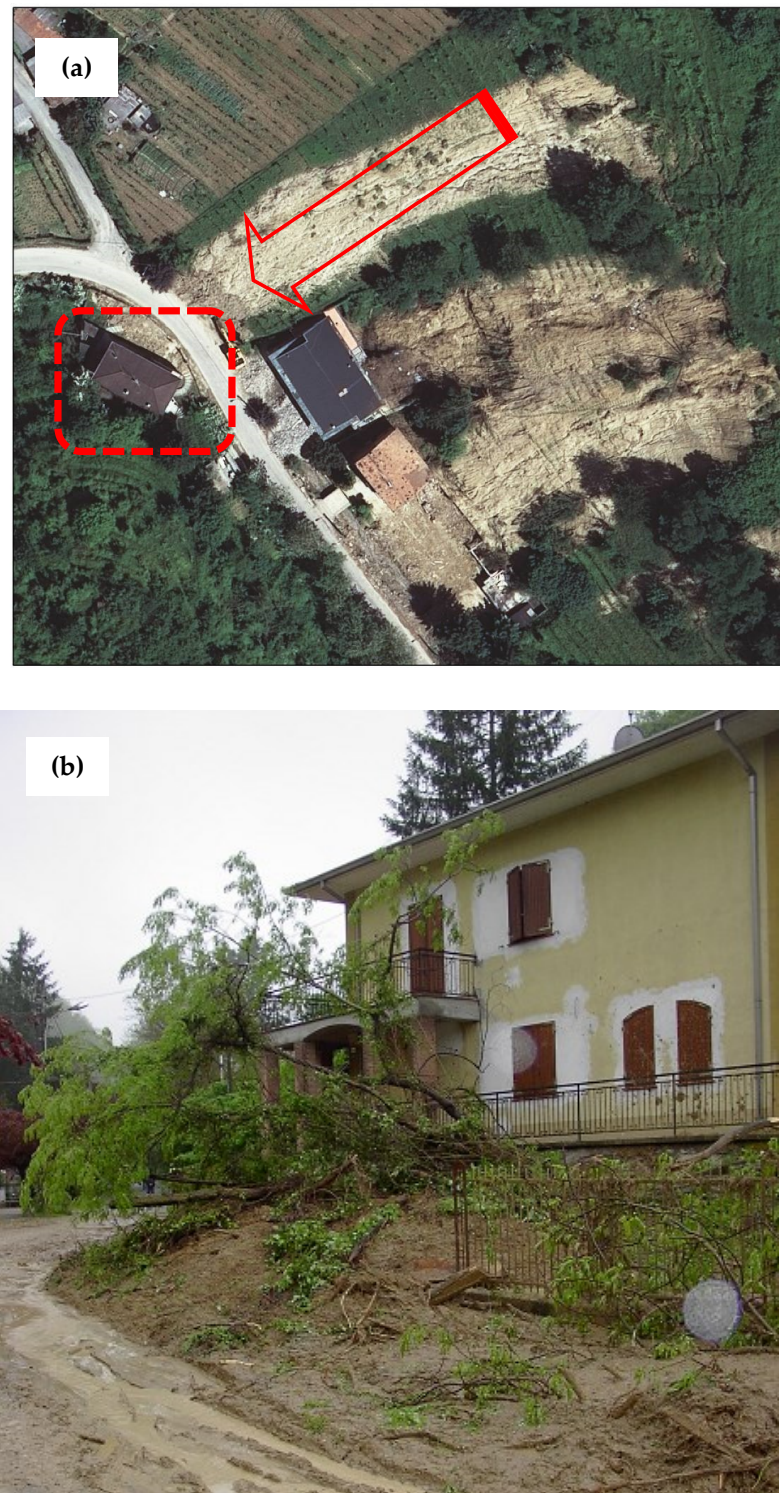


Figure 6.1 Rainfall induced landslide occurred on April 2009 in the Recoaro valley of the Oltrepò Pavese: (a) Plan view with the sliding direction (red arrow) and the downstream structure impacted by the landslide (dashed red square), the aerial photograph of the area was taken by Ditta Rossi s.r.l. (Brescia, Italy) on May 18th 2009; (b) Impacted structure showing part of the slide.

After sliding inside an almost straight corridor with nearly constant width of about 14m (Fig. 6.1 (a)), the saturated soil impacted against the vertical wall of a building located at the toe of the opposite slope causing the landslide to stop abruptly (Fig. 6.1 (b)). Some small trees were transported by the earth-flow but they were neglected in the present simulation. The portion of the deposit obstructing the street on the valley floor was suddenly removed for safety purposes. Anyway, the upstream portion of the deposit was not altered and survey data of its final profile are available. The position of the downstream obstacle is not perpendicular to the landslide propagation direction, thus after the impact the actual landslide behavior near the wall may deviate from the 2D assumption. However, this feature does not affect the landslide characteristics during the run-out phase that are relevant for risk assessment (i.e., front thickness and velocity) but may affect the prediction of impact force that cannot be considered uniformly distributed in the transversal direction. Furthermore, from Fig. 6.1 (b) the depth of the deposit just in front of the impacted structure can be estimated and it seems almost uniformly distributed in the transversal direction. This information is used as reference for comparison with the landslide simulated final profile. The relevant geotechnical characteristics of the soil involved in the collapse are collected from Bordoni et al. (2015b) and summarized in Table 6-I. These soils are clayey-sandy silts, characterized by close to nil cohesion. The values of the soil features have been used to estimate the input parameters adopted in the validation analysis.

Table 6-I Summary of the values assigned to relevant geotechnical parameters.

Relevant geotechnical soil parameters	
angle of internal friction φ	24-26°
saturated unit weight γ_{sat}	18-19 kN/m ³
saturated volumetric water content \mathcal{S}_s	0.42-0.46

6.3. Results and discussion

This section illustrates and discusses the results of performed simulations. An overall number of 26 simulations have been carried out to investigate various parameters that are relevant for the analysis, as discussed in the following. Table 6-II shows the relevant geotechnical parameters of the rainfall induced landslide occurred on April 2009 in the Recoaro valley. According to the observations, the soil mass is assumed fully saturated at the beginning of the collapse under the gravity force. Furthermore, it is quite reasonable to neglect the soil cohesion as the failure takes place. The speed of sound α in the solid phase is the square root of the ratio between the bulk compressibility modulus and the density. The artificial viscosity coefficient is here slightly smaller than $\alpha_M=0.10$ (Manenti et al., 2018): the reference value for the landslides simulated with SPHERA should be considered as $\alpha_M=0.09\pm 0.01$.

Table 6-II Summary of the relevant input parameters

Relevant input parameters	
particle resolution dx	0.25; 0.10 m
smoothing length h	0.325m; 0.13 m
artificial viscosity coefficient α_M	0.075
sound speed c	80 m/s
solid phase density ρ_s	2650 kg/m ³
angle of internal friction φ	24°
effective porosity e	0.42
maximum initial landslide height h_0	136.7 m a.m.s.l.
run-up length on the downstream wall l_{r-u}	4.0 m

First of all, the simulation results involving the effects of both maximum viscosity and limiting viscosity are discussed to explore the trade-off between computational time and accuracy in the results (Sect. 6.4.1). Then the final landslide profile after the stop at the toe of the downstream structure is

compared with survey data for model validation (Sect. 6.4.2). Finally, the influence of geotechnical input parameters on the landslide front celerity and impact force that affect the dangerousness associated with a landslide occurrence is analyzed (Sect. 6.4.3).

6.3.1. Analysis of viscosity

As explained in the previous section, early simulations have been carried out to define the value of the maximum viscosity μ_{max} for the problem under consideration. Following the approach tested in previous works (Amicarelli et al., 2017; Manenti et al., 2018), the initial simulation is performed by assuming a suitably high value that is $\mu_{max} = 1.0 \text{ e}+6 \text{ kPa}$. This choice requires the adoption of a suitable initial value of the particle spacing which is conveniently set at $dx = 0.25\text{m}$ based on the problem characteristic length-scale. The effect of limiting viscosity is neglected at this stage of investigation by assigning to it a value greater than maximum viscosity. The resulting rheological behavior is shown in the lower right-hand part of Fig. 6.2: pseudo-plastic behavior is assumed for those shear rates that correspond to an apparent viscosity $\mu_{\dot{\gamma}}$ lower than μ_{max} . At each subsequent simulation, the maximum viscosity value is reduced by one order of magnitude down to $\mu_{max} = 1.0 \text{ e}+3 \text{ kPa}$. The landslide front celerity is monitored during the run-out until the stop. The main plot in Fig. 6.2 shows the non-dimensional evolution of the landslide front position ξ over non-dimensional time τ , where x is the horizontal abscissa along the sliding direction, h_0 denotes the maximum initial landslide height (Tab. 6-II), that is the height of the upper landslide front at $x=16.20\text{m}$. No noticeable variation in the landslide kinematics can be appreciated, despite the significant reduction in the computational time. An additional simulation is then performed to assess the effect of lowering the maximum viscosity to $\mu_{max} = 0.5 \text{ e}+3 \text{ kPa}$. As it can be seen from the black dashed curve in Fig. 6.2, this further reduction in the maximum viscosity produces some effects on the kinematics of the landslide front: the final

position around time $\tau=3.5$ is nearly the same as in previous simulations, but the leading front celerity is a little bit smaller in the time interval $\tau = [1.5 - 3.0]$.

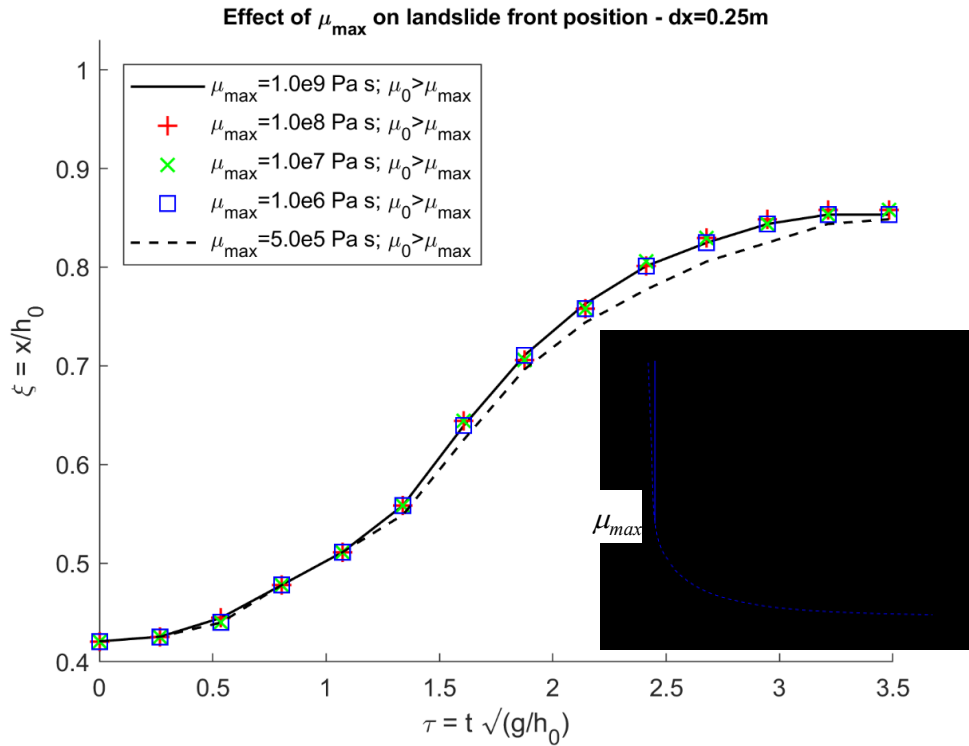


Figure 6.2 Effect of maximum viscosity μ_{max} on landslide front propagation. Non-dimensional front position ξ as a function of the non-dimensional time τ .

From the simulations performed it can be concluded that the value $\mu_{max} = 1.0 \text{ e}+3$ kPa does not affect appreciably the landslide dynamics and allows significantly reducing the computational time. Therefore, this value is adopted for the maximum viscosity in subsequent simulations.

As a result of the computational time reduction, the particle resolution was changed from the initial value down to a lower value of $dx = 0.10\text{m}$. Further reduction in dx below such a value does not significantly affect the numerical results while increasing the computational time. Although the value of the maximum viscosity depends on the spatial resolution and the limiting viscosity, the above procedure seems sufficient for the current test case.

The subsequent set of simulations is carried out to define the optimal value for

the limiting viscosity in order to further reduce the computational time while maintaining suitable level of accuracy of the simulation results. The lower right-hand part of Fig. 6.3 shows the resulting rheological behavior when activating the limiting viscosity μ_0 (red curve). As it can be seen, in the limiting region between the transition from the frictional regime to the elastic-plastic regime, the actual value of the mixture viscosity μ_{fr} is approximated with the constant value $\mu_0 < \mu_{max}$. This approximation allows further reduction in the computational time through Eq. (6.3), but the amount of approximation that is introduced should be maintained below a suitable threshold.

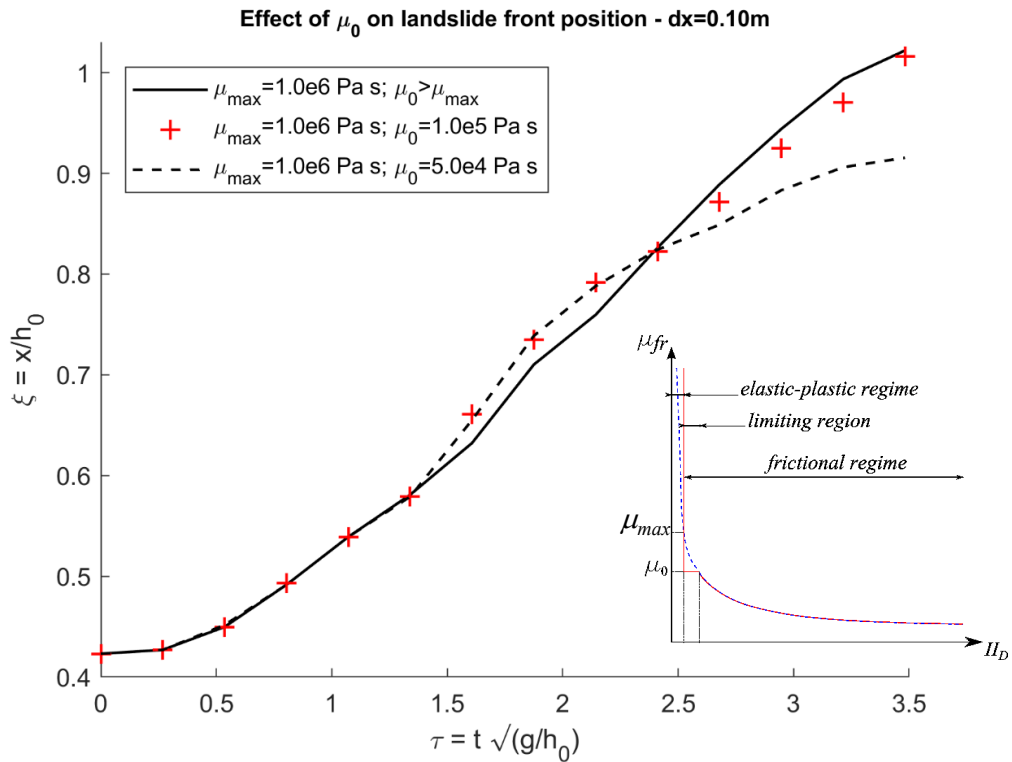


Figure 6.3 Effect of limiting viscosity μ_0 on landslide front propagation. Non-dimensional front position ξ as function of non-dimensional time τ .

The landslide front position versus time is shown in the main plot of Fig. 6.3 when reducing progressively the limiting viscosity below μ_{max} . The vertical downstream wall has been temporarily removed in order not to affect the landslide front kinematics. It can be seen that negligible change in the landslide

front celerity compared to the reference curve (continuous black line with $\mu_0 > \mu_{max}$) can be obtained with the assumption $\mu_0 = 0.1 \text{ e}+3 \text{ kPa}$ (red cross markers). Further reduction in the limiting viscosity to $\mu_0 = 0.05 \text{ e}+3 \text{ kPa}$ causes unacceptable reduction in the landslide front celerity.

In conclusion, for the present analysis the maximum viscosity can be set equal to $\mu_{max} = 1.0 \text{ e}+3 \text{ kPa}$ without influencing the landslide kinematics, while the limiting viscosity can be conveniently assumed equal to $\mu_0 = 0.1 \text{ e}+3 \text{ kPa}$. This result represents an optimal compromise between numerical accuracy and computational time.

6.3.2. Validation

The simulation of the actual landslide occurred on April 2009 in the Recoaro valley after intense rainfall events has been carried out assuming the geotechnical parameters values in Table 6-I. These represents average values for the soil involved in the failure and no calibration was carried out for fitting the numerical results to the observed data.

Figure 6.4 shows some representative frames of the post-failure dynamics. Upper frames show the initial volume of unstable soil that is obtained by subtracting the pre-event profile to the post-event profile. In the central part of the profile no significant variation of the topographic surface can be appreciated, probably due to low run-out ratio. Therefore, in this case soil entrainment was neglected. In the case where soil entrainment represents an important process, it can be simulated with a scheme for the erosion process that has been implemented in SPHERA (Manenti et al., 2011b). It can be seen that in the early phase, at $t = 3.0 \text{ s}$, the mass portion close to the landslide front moves faster than the rear portion. Just after the impact against the vertical wall of the downstream building, at $t = 13.0 \text{ s}$, the landslide front began decelerating and stops while the rear mass portion on the steep slope still maintained a relatively high average speed. In this case the

modeling approach based on the infinite landslide with constant depth and moving at a constant velocity on a constant slope may not be appropriate at all. Instead, SPHERA allows reproducing the velocity gradients along the landslide, potentially providing more reliable representation of the landslide dynamics and the resulting impact force on the rigid wall.

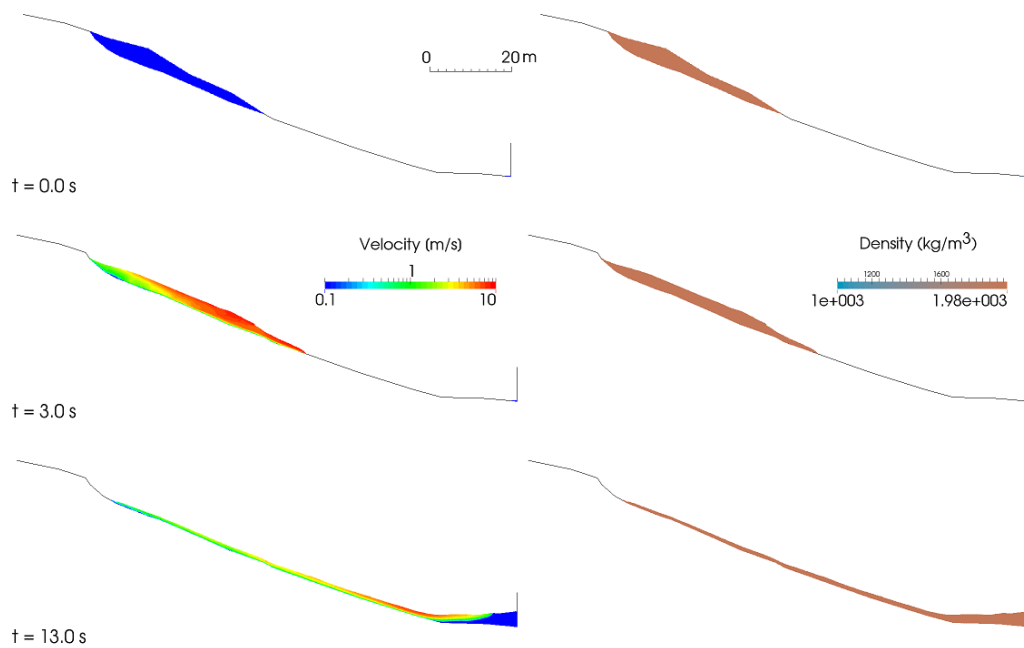


Figure 6.4 Representative frames of landslide run-out and impact. Contour plots show velocity magnitude (left-hand panels) and density field.

The final landslide profile at $t = 60s$ is shown by the red line in Fig. 6.5. At this stage, the major part of the landslide mass has come to a complete stop. The blue markers represent the experimental points obtained during the post event survey. The comparison shows that numerical results provide quite acceptable prediction of the final configuration of the landslide. Even if at $t = 60s$ the main portion of the landslide body has come to a complete stop, some few particles in the upper part of the sliding profile show a small downstream velocity and probably may compensate at later instants for the slight underestimation of the height of experimental points between abscissa 65m and 80m.

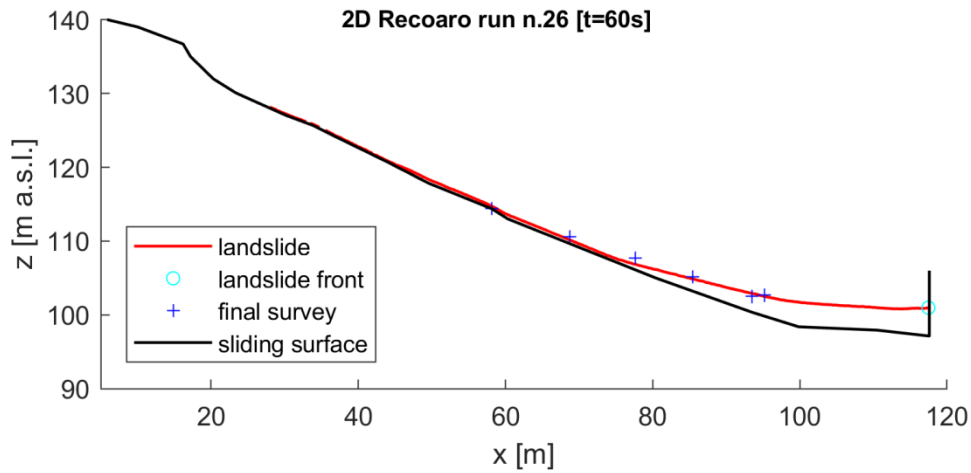


Figure 6.5 Simulated final profile of the landslide at $t = 60$ s (red line). The upper part of the landslide profile is compared with experimental points from the post-event survey (blue markers).

As previously said, the estimate of related risk depends upon several landslide characteristics such as: width and length of damage corridor, travel velocity, characteristic depth of both moving mass and deposit. In this case study, the width and length of the damage corridor are fixed; the characteristic depth of deposit is suitably well represented; the average travel velocity seems quite acceptable as the run-out duration, from the beginning of the sliding till the impact on the wall, is about 10 s which is quite reasonable for the considered case. Therefore, it can be concluded that SPHERA allows obtaining an acceptable estimate of the risk level associated to the landslide.

6.3.3. Influence of input parameters

To consider the effects of the uncertainties potentially affecting the relevant geotechnical parameters, their influence on the landslide front celerity and the impact force on the downstream vertical wall have been evaluated from the fluid pressure field over the wall. SPHERA also allows a more accurate assessment of the fluid forces exerted on solid bodies by means of a scheme for the transport of solid bodies (Amicarelli et al., 2015b, 2020b). The following parameters have been considered in the sensitivity analysis: angle of internal friction φ ; effective

porosity e ; and solid phase density ρ_s . The investigated range of each parameter has been selected based on the typical range for the soil involved in the simulated landslide, as described in Table 6-II. In particular, for the angle of internal friction a variation of $\pm 4^\circ$ is assumed (run 22 and run 23) with respect to the average value $\phi = 24^\circ$ adopted in the validation analysis carried out with the reference run 26 (Tab. 6-I). Concerning the effective porosity, a bigger value of $e = 0.50$ is assumed (run 24). Finally, an increased density value of the solid phase equal to $\rho_s = 2900 \text{ kg/m}^3$ is considered (run 25). The influence produced by the variation of each parameter has been evaluated individually and the obtained results are discussed below.

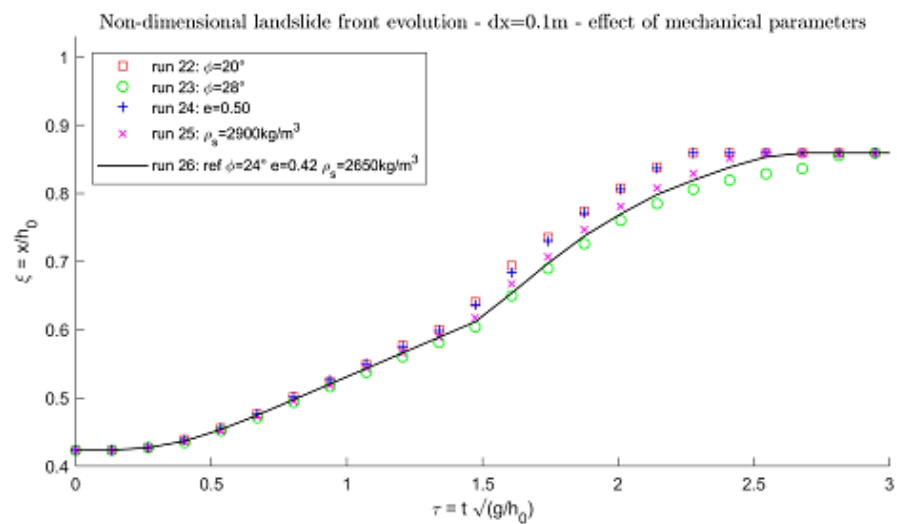


Figure 6.6 Effects of geotechnical parameters variation on landslide front propagation. Non-dimensional front position ξ as function of non-dimensional time τ .

Figure 6.6 shows the evolution of non-dimensional landslide front position ξ versus the non-dimensional time τ . The continuous black line shows the result for the reference run used for model validation. As the wall is assumed rigid, the final landslide front position after the wall impact is independent from the values assigned to the input parameters. According to theoretical expectations, a reduction in the angle of internal friction produces an increase in the landslide front celerity (red square marker). Similar behavior is detected in the simulation

with increased effective porosity (blue plus marker) where the rise of the water content reduces, as expected, the sliding resistance between mixture particles resulting in an increase in the landslide speed. In both runs 22 and 24 the impact against the downstream vertical rigid wall is anticipated around time $\tau = 2.3$.

When increasing the solid phase density in run 25 a restrained increase in the landslide front velocity is attained (pink cross markers). The impact with the vertical downstream wall occurs around time $\tau = 2.5$, slightly before the impact time detected in the reference run at about time $\tau = 2.7$.

The increase in the angle of internal friction in run 23 is responsible for an overall reduction in the landslide front celerity whose impact on the downstream vertical wall occurs at later time close to $\tau = 3.0$. This behavior, which is quite the opposite of the one detected when reducing the angle of internal friction, is in accordance with the formulation in Eqs. (6.2) where the frictional resistance between mixture particles increases with φ .

The influence of these parameters on the landslide kinematics affects the dynamic impact as well. The greater the landslide velocity, the greater and earlier the impact force. This is confirmed by the analysis of results in Fig. 6.7 where the non-dimensional resultant force on the wall per unit width versus non-dimensional time is shown for the four simulations in comparison with the reference run. The parameter l_{r-u} represents the run-up length on the downstream wall (Tab. 6-I).

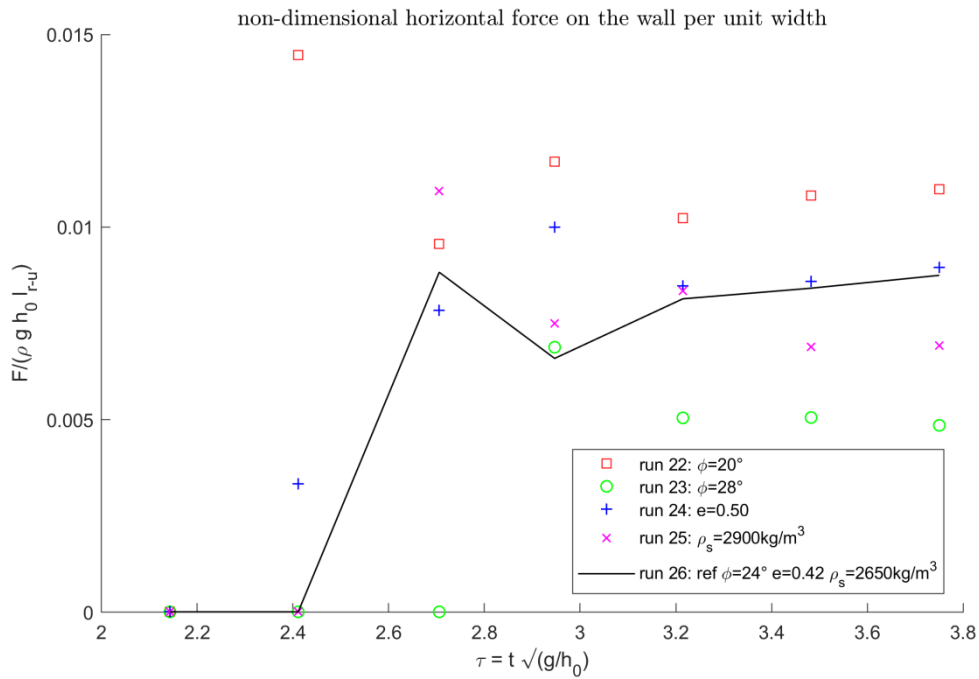


Figure 6.7 Effects of geotechnical parameters variation on the impact force on the vertical downstream wall.

The greatest impact force occurs for run 22 with reduced angle of internal friction; this peak occurs just after the impact instant when the frontal portion of the landslide with the highest kinetic energy has come to almost complete stop. In the case of run 24, which showed a similar landslide front kinematics to run 22, the peak of force is significantly shifted forward in terms of the impact time and is much lower. This is due to the pronounced fluidic behavior caused by the higher water content: as a result, in run 24 the force acting on the downstream wall is distributed over a wider time span (about $\Delta\tau = 0.8$) resulting in a less steep trend and following reduced peak.

In both runs 23 and 25 the peak of impact force occurs just after the impact of landslide front on the downstream wall. The magnitude of the peak for run 25 is much greater than the reference run and close to the peak observed in run 24, but the impact force evolves very quickly over time in run 25.

If compared with run 22, it can be seen that the magnitude of peak force is much lower for run 23 due to the highest frictional dissipation that reduces the overall

amount of kinetic energy transferred to the wall. This behavior is in accordance with Eqs. (6.2).

6.4. Conclusions

This work illustrates the validation of the free open source 3D research code SPHERA (Amicarelli et al., 2020b) based on WCSPH method for simulating a rainfall-induced fast shallow landslide occurred in 2009 on a hilly area in the North-western side of Italy. Owing to the peculiarities of this landslide being characterized by a relatively constant width of the almost straight sliding corridor, the flow may be assumed as two-dimensional in the longitudinal vertical plane and a simpler and faster 2D execution is conveniently carried out.

In contrast with depth integrated models, SPHERA allows resolving the vertical velocity gradients of the landslide that are produced by its geometrical characteristics. Also, the resolution of the vertical velocity gradients leads to a reliable representation of the landslide dynamics and, possibly, of the related impact force on the downstream wall.

The characteristic depth of the final deposit is suitably well represented; the average travel velocity seems quite acceptable for the considered case. These results are fundamental for obtaining reliable estimate of the risk level associated to the landslide.

The time evolution of the resultant impact force on the downstream vertical rigid wall is also computed. This feature may be helpful supporting the design of reliable protection measures.

No tuning of relevant geotechnical parameters is needed for fitting the numerical results to the observed data from the post-event survey. Input parameters can be obtained straightly from average soil characteristics. Overall good accuracy is found: this relevant result seems promising for application of SPHERA to the prediction of fast shallow landslide related risk.

Sensitivity analysis has been finally carried out to assess the possible

uncertainties affecting relevant geotechnical parameters. Obtained results are consistent with the theoretical expectations.

In this work the volume of the soil affected by the landslide can be determined from the comparison between pre- and post-event topography. As an alternative for landslide risk prediction, future developments will be devoted to coupling the code SPHERA with a rainfall-induced landslide triggering model, capable of estimating the landslide volume starting from data concerning rainfall pattern and initial soil conditions.

6.5. Acknowledgment

SPHERA v.9.0.0 is realized by RSE SpA thanks to the funding “Fondo di Ricerca per il Sistema Elettrico” within the frame of a Program Agreement between RSE SpA and the Italian Ministry of Economic Development (Ministero dello Sviluppo Economico).

Chapter 7

Conclusions

This chapter concludes the thesis by summarizing the key research findings in relation to the research aims and questions and discussing the value and contribution thereof. It also reviews the limitations of the study and proposes opportunities for future research.

7.1 Main conclusions

The following main conclusions can be drawn from the research conducted in this thesis:

- The integration of reanalysis soil moisture data in regional landslide triggering thresholds (e.g., Chapter 4) allowed an increase of the predictive performance if compared with those of the traditional *ID* approach, but only when the observed rainfall is inputted into the proposed multi-step procedure. Indeed, a drop in performance occurred when the reanalysis precipitation is used, and lower *TSS* values are obtained in correspondence of all investigated scenarios. Other than that, overall, the use of the ANN-based optimization tool and the subsequent parametrization of the optimal thresholds allowed us to obtain curves that are easy to insert within a LEWS framework. Moreover, although a third variable was added (i.e., the principal components of soil moisture, computed through the PCA), this procedure made it possible for us to come up, anyway, with the identification of 2D thresholds.
- The investigation of the potential rainfall-induced landslide modeling improvements using 3D slope stability analysis and optimization algorithms at the catchment scale (i.e., Chapter 5), allowed obtaining a better prediction of landslide prone areas, leading to greater True Skill

Statistic (TSS) value if compared with one obtained for the 1D approach. This is to be attributed to the proposed optimization process, which allows a greater gain of performance passing from the 1D to the 3D simulation, in comparison to other studies, where no optimization has been applied. Furthermore, the 3D approach is able to reduce the number of false and missing predictions and, although the overestimation of the unstable areas in comparison with the infinite slope approach, it was revealed to be more accurate with regard to the slip surface prediction.

- The analysis of post-failure dynamics using the free open source 3D research code SPHERA (Amicarelli et al., 2020b, 2017) based on WCSPH (i.e. Chapter 6) allowed resolving the vertical velocity gradients of the landslide resulting from its unsteady non-uniform dynamics. Also, the resolution of the vertical velocity gradients leads to a consistent representation of the landslide dynamics and, possibly, of the related impact force on the downstream wall. The comparison with available survey data after deposition shows that SPHERA was able to well represent the characteristic depth of the final deposit. Even if measures of the impact load are not available for model comparison, the time evolution of the resultant impact force on the downstream wall is compatible with the timescale of this kind of debris flow. These aspects are fundamental for obtaining a reliable estimate of the risk level associated to the landslide and supporting the design of reliable protection measures. Furthermore, the sensitivity analysis has been finally carried out to assess the possible uncertainties affecting relevant geotechnical parameters, and obtained results are consistent with the theoretical expectations.

7.2 Limitations and future perspectives

The study presented in this thesis has highlighted some issues which need to be deeply investigated and constitute opportunities for future research. These open issues can be summarized as follow, according to the three main issues covered in this thesis:

- With regard to the identification of the regional landslide triggering thresholds, the reasons behind the drop in performance when reanalysis rainfall is used should be better investigated. Overcoming this issue allows to exploit the larger availability of the reanalysis rainfall, avoiding the difficulties related to the point rain gauges. Besides this, being able to identify the optimal parametric thresholds for more study areas, would surely allow to better assess the general performance gain obtainable with the proposed methodology.
- Even if the 3D slope stability analysis (SCOOPS3D) together with the multi-objective optimization for the model parameterization allowed a more reliable prediction of prone areas, it needs to be more investigated to improve performance. A way to achieve this is probably assessing the input initial conditions of the TRIGRS model integrating soil moisture information, in order to obtain a more reliable hydrological response which can be used as input in the 3D slope stability analysis.
- Concerning the analysis of the post-failure dynamics, future developments can be devoted to coupling the code SPHERA with a rainfall-induced landslide triggering model, capable of estimating landslide volume, starting from data concerning rainfall pattern and initial soil conditions. This triggering model could be just SCOOPS3D, which, providing the terrain elevation pre- and post- failure, indirectly yields the landslide volume.

Acknowledgments

Coming to the end of my Ph.D. adventure, I wish to acknowledge all the people who have stood by me in these three years.

This thesis is also yours.

Firstly, I would like to acknowledge my Supervisor, *Prof. Enrico Creaco*, who always assisted and guided me throughout this research project, and who greeted me warmly since my first day here in Pavia.

Thanks to *Prof. Sauro Manenti* and to *Dr. Andrea Amicarelli* to give me the opportunity to plunge me into the SPHERA world. I would like to thank you for your patience and hard work.

I would also thank the Ph.D. coordinator, *Prof. Alessandro Reali*. It was truly a pleasure to meet such a friendly and always available professor.

To *Prof. Antonio Cancelliere*, a staple for me, I express my gratitude and heartfelt thanks for having believed in me since my Master's degree and for having assisted me to this day.

Thanks to *Dr. Peres*, for his concrete and generous support. *David*, I would like to thank you for your time and for having taught me so much.

A special thanks to *Dr. Rex L. Baum*, Supervisory Research Geologist at United States Geological Survey (USGS) in Golden (Colorado, US), who hosted me during my research internship abroad. Thank you for your sincere efforts in continue to make science with me, despite the uncertainties and concerns about the COVID-19 pandemic, that had just begun at that time. It was a privilege to work with you.

To the Reviewers of this thesis, *Prof. Brunella Bonaccorso* and *Prof. Giovanna Capparelli*, goes my gratefulness for their comments and suggestions that have for sure improved and enhanced this research.

Finally, these acknowledgments are also and, above all, to my family. So, sorry, but now I have to switch to Italian.

Grazie ai miei *genitori* e ai miei *fratelli*. Grazie per aver sostenuto ogni mia scelta. Grazie per avermi sempre compreso. Tutto il mio impegno e ogni sforzo sono e continueranno ad essere per voi, affinché possiate essere orgogliosi di me.

E per concludere, grazie a *Francesco*. Grazie per avermi incondizionatamente spronata a superare i miei limiti e a credere in qualcosa in cui persino io faticavo a credere. Solo tu sai quanto tutto questo abbia significato per me, e per noi.

Nunziarita

List of symbols

Chapter 4

I	mean rainfall intensity
D	rainfall duration
α	power law threshold intercept parameter
β	power law threshold slope parameter
E	total event rainfall
Z_w	depth of the potential failure surfaces
θ	soil water content
C_w	warm period in a year
C_c	cold period in a year
G_s	resolution of the rain gauge
A	principal components' loadings (i.e., coefficients) table
S_i	principal components for the generic row i
σ_1	percentage of variance explained by the first principal component
σ^*	percentage of variance explained threshold
x_0, x_1, y_0, y_1	optimal threshold's parameters
a_{ij}	generic loadings value for the PCA
P	number of observed landslides
N	number of non-landslides

Chapter 5

Z	vertical downward coordinate
t	time
$\theta(Z, t)$	soil water content
$\psi(Z, t)$	pore pressure
$K(\psi)$	hydraulic conductivity
∂	ground slope surface
K_s	saturated hydraulic conductivity
α	inverse height of the capillary rise
θ_r	residual water content
I	infiltration
P	precipitation rate
R_u	runoff rate from the upslope cells

R_d	runoff the downslope cells
φ'	soil friction angle for effective stress
c'	soil cohesion for effective stress
γ_s	soil unit weight
γ_w	unit weight of groundwater
δ	slope angle
s	average shear resistance (strength)
τ	shear stress
σ_n	total normal stress acting on the failure surface
u	pore-water pressure acting on the shear surface
A_{hij}	horizontal area of the trial slip surface
R_{ij}	distance from the axis of rotation to the center of trial slip area
W_{ij}	weigh of the trial slip surface
u_{ij}	pore-water pressure of the trial slip surface
c_{ij}	cohesion of the trial slip surface
φ_{ij}	angle of internal friction on trial slip surface
$m_{a_{ij}}$	part of the computation of normal force acting on the trial slip surface of the i,j column in a potential failure mass, used in Bishop's simplified method
K_{eq}	term related to the option to simulate earthquake or seismic loading effects
e_{ij}	term related to the option to simulate earthquake or seismic loading effects
Δ_r	radius increment to explore trial surfaces
$Z_{s,min}$	minimum elevation of the search-lattice nodes with respect to the DEM elevation
$Z_{s,max}$	maximum elevation of the search-lattice nodes with respect to the DEM elevation
a_{min}	minimum horizontal surface area for potential failure masses
a_{max}	maximum horizontal surface area for potential failure masses
α	Gardner's parameter
y_{min}	minimum values of effective soil depth
y_{max}	maximum values of effective soil depth
x_i	slope angle at point i

Chapter 6

u	mixture velocity
g	gravity acceleration
B_ρ	boundary contributions for mass balance equations
B_u	boundary contributions for momentum balance equations
c	mixture pressure
m	particle mass
ρ	mixture density
W_{ij}	compact supported central kernel function of the relative distance between a generic fluid particle, denoted by index i , and each one of the N neighbouring particles, denoted by index j
$\pi_{i,j}$	Monaghan artificial viscosity term
τ	viscous stress tensor
\mathbf{D}	strain rate tensor
μ_{fr}	apparent viscosity
σ'	effective stress
φ	angle of internal friction
Π_D	strain rate tensor
h	smoothing length related to particle size dx
c	sound speed
CFL	Courant–Friedrichs–Lewy number
μ_{max}	maximum (or threshold) viscosity
μ_0	limiting viscosity
γ_{sat}	saturated unit weight
ϑ_s	saturated volumetric water content
dx	particle resolution
α_M	artificial viscosity coefficient
ρ_s	solid phase density
e	effective porosity
h_0	maximum initial landslide height
l_{r-u}	run-up length on the downstream wall
τ	non-dimensional time
ξ	non-dimensional front position

List of figures

Figure 2.1 Simple illustration representing some common landslide types (Highland and Bobrowsky, 2008)	17
Figure 2.2 Conceptual examples of some typical triggering mechanism of debris flow by Shen et al. (2018)	19
Figure 2.3 Rainfall intensity-duration (ID) thresholds. Numbers refer to case studies investigated by Guzzetti et al. (2007). Very thick lines are global thresholds and thin lines are local thresholds. Black lines are referred to central and eastern Europe, whereas the grey ones are referred to other regions or areas (Bogaard and Greco, 2018).....	22
Figure 2.4 Infinite slope model to analyze rain infiltration induced shallow failure (Muntohar and Liao, 2009)	26
Figure 2.5 Diagram showing a 3D perspective view of a cone-shaped digital elevation model (DEM) and one potential failure (trial) surface. The potential failure mass (removed from this diagram) is composed of an ensemble of columns defined by the DEM grid with the center of the spherical trial surface and the axis of rotation located above the DEM (Reid et al., 2015).....	27
Figure 3.1 Soil-water retention data and optimized curves for the Oso Flaco fine sand and Columbia sandy loam soil (Tuli and Hopmans, 2004). 34	
Figure 3.2 Sketch showing how Data Assimilation works to generate reanalysis data (ECMWF model).....	42
Figure 3.3 Spatial structure added in HTESSSEL (for a given precipitation $P_1=P_2$ the scheme distributes the water as surface runoff and drainage with functional dependencies on orography and soil texture respectively) (Balsamo et al., 2009) (https://confluence.ecmwf.int/display/OIFS/)	45
Figure 4.1 Schematization of the procedure followed for the dataset creation.....	53

Figure 4.2 Description of the methodology.....	61
Figure 4.3 Elevation map of the study area (Sicily region), showing the location of the landslide occurrences (Calvello and Pecoraro, 2018) and of the rain gauges, over the period 2010-2018 (Distefano et al., 2021).	62
Figure 4.4 Total variance explained by each principal component.	65
Figure 4.5 Traditional power-law threshold on the log-log plane between observed mean rainfall intensity (I) and duration (D).....	66
Figure 4.6 Optimal parametric threshold (black line) on the log-log plane between observed mean rainfall intensity (I) and duration (D). The raw non-parametric threshold (dash black line) is also shown.....	66
Figure 4.7 Panel showing the raw non-parametric thresholds and the corresponding optimal parametric thresholds on the semi-log plane between mean rainfall intensity and soil moisture at the four distinct depths.....	69
Figure 4.8 Optimal parametric threshold (black line) on the semi-log plane between observed mean rainfall intensity (I) and first principal component of soil moisture (S_1). The raw non-parametric threshold (dash black line) is also reported.	70
Figure 4.9 Optimal parametric threshold (black line) on the semi-log plane between the observed mean rainfall intensity (I) and the first principal component of soil moisture (S_1). (a) Shows the case when the first class of the second principal component of soil moisture is considered; (b) Shows the case when the second class of the second principal component of soil moisture is considered. The raw non-parametric thresholds (dash black line) are also reported in both cases.....	71
Figure 4.10 Traditional power-law threshold on the log-log plane between ERA5-Land mean rainfall intensity (I) and duration (D).	73
Figure 4.11 Optimal parametric threshold (black line) on the log-log plane between ERA5-Land mean rainfall intensity (I) and duration (D). The raw non-	

parametric threshold (dash black line) is also shown.....	73
Figure 4.12 Panel showing the raw non-parametric thresholds and the corresponding optimal parametric thresholds on the semi-log plane between ERA5-Land mean rainfall intensity (I) and soil moisture at the four distinct depths.	74
Figure 4.13 Optimal parametric threshold (black line) on the semi-log plane between ERA5-Land mean rainfall intensity (I) and first principal component of soil moisture (S_1). The raw non-parametric threshold (dash black line) is also shown.....	75
Figure 4. 14 Optimal parametric threshold (black line) on the semi-log plane between ERA5-Land mean rainfall intensity (I) and first principal component of soil moisture (S_1). (a) Shows the case when the first class of the second principal component of soil moisture (S_2) is considered; (b) Shows the case when the second class of the second principal component of soil moisture (S_2) is considered. The raw non-parametric thresholds (dash black line) are also shown in both cases.....	76
Figure 5.1 Description of the methodology.....	86
Figure 5.2 One-cell sketch for the TRIGRS model (Rex L. Baum, William Z. Savage, 2008).....	87
Figure 5.3 Diagram showing a 3D search lattice above a DEM. Each dot represents the center of multiple spherical trial surfaces (Reid et al., 2015).....	91
Figure 5.4 (a), (b), (c), (d) Examples of landslide in the study area (Valentino et al., 2014); (e) Catchment within Oltrepò Pavese region.....	97
Figure 5.5 (a) Catchment topography with observed landslides triggered after the extreme rainfall on April 27-28, 2009 and location of soil thickness sampling points. Maximum and minimum areas (a_{min} , a_{max}) considered as lower and upper limits in the optimization process of the slip-surface search parameters for SCOOPS 3D are also represented; (b) Catchment slope.....	98

Figure 5.6 Measured vs. estimated soil thickness points.....	100
Figure 5.7 (a) Hourly rainfall series used in input for simulations; (b) simulated catchment-averaged pressure head series; (c) simulated potential unstable cells for the event of April 27-28, 2009 (1D analysis using TRIGRS v. 2.1).....	102
Figure 5.8 Comparison of the results of TRIGRS and SCOOPS 3D in the FPR-TPR space. Selection of the ultimate solution of SCOOPS 3D is also reported.	103
Figure 5.9 (a) Factor of safety spatial distribution as a result of 1D slope stability analysis (Simulation I); (b) Factor of safety spatial distribution as a result of 3D slope stability analysis (Simulation II); (c) Cumulative frequency of the factor of safety resulting by both 1D and 3D models	106
Figure 6.1 Rainfall induced landslide occurred on April 2009 in the Recoaro valley of the Oltrepò Pavese: (a) Plan view with the sliding direction (red arrow) and the downstream structure impacted by the landslide (dashed red square), the aerial photograph of the area was taken by Ditta Rossi s.r.l. (Brescia, Italy) on May 18 th 2009; (b) Detail of the impacted structure showing part of the slide.....	119
Figure 6.2 Effect of maximum viscosity on landslide front propagation. Non-dimensional front position as a function of the non-dimensional time.....	123
Figure 6.3 Effect of limiting viscosity on landslide front propagation. Non-dimensional front position as function of non-dimensional time.....	124
Figure 6.4 Representative frames of landslide run-out and impact. Contour plots show velocity magnitude (left-hand panels) and density field.....	126
Figure 6.5 Simulated final profile of the landslide at $t = 60$ s (red line). The upper part of the landslide profile is compared with experimental points from the post-event survey (blue markers).....	127
Figure 6.6 Effects of geotechnical parameters variation on landslide front propagation. Non-dimensional front position as function of non-dimensional time.....	128

Figure 6.7 Effects of geotechnical parameters variation on the impact force on the vertical downstream wall. 130

List of tables

Table 3-I Surrogate measures used by different θ_v sensors (Busscher, 2009).....	37
Table 3-I (continue) Surrogate measures used by different θ_v sensors (Busscher, 2009).....	38
Table 3-II Overview of the main characteristics of ERA-Interim, ERA5, and ERA5-Land (Muñoz-Sabater et al., 2021).....	44
Table 4-I Confusion matrix for ROC analysis.....	58
Table 4-II Summarizing table of the TSS values in correspondence of each analyzed scenario when the observed rainfall is used, and parameters (x_0, y_0, x_1, y_1) estimated for the optimal parametric thresholds.....	68
Table 4-III Summarizing table of the TSS values in correspondence of each analyzed scenario when the ERA5-Land rainfall is used, and parameters (x_0, y_0, x_1, y_1) estimated for the optimal parametric thresholds.	77
Table 5-I Confusion matrix for ROC analysis.....	85
Table 5-II Geotechnical and hydraulic properties for the study area (Bordoni et al., 2015c; Zizioli et al., 2013).	100
Table 5-III Decision variables constraints used in the optimization process of the slip-surfaces search parameters for SCOOPS 3D.	101
Table 5-IV Ultimate values of the objective functions FPR and TPR in Simulations I and II and corresponding responses of the True Skill Statistic (TSS). Optimized values of the slip-surfaces search parameters for SCOOPS 3D are also reported.....	104
Table 5-V Comparison of LRclass index obtained with the 3D and 1D approaches, both calculated at 9 p.m. on 27 April, 2009... ..	107
Table 6-I Summary of the values assigned to relevant geotechnical parameters.....	120

Table 6-II Summary of the relevant input parameters....121

References

- Aaron, J., McDougall, S., and Nolde, N.: Two methodologies to calibrate landslide runout models, 16, 907–920, <https://doi.org/10.1007/s10346-018-1116-8>, 2019.
- Abdi, H. and Williams, L. J.: Principal component analysis, Wiley Interdiscip. Rev. Comput. Stat., 2, 433–459, <https://doi.org/10.1002/WICS.101>, 2010.
- Abraham, M. T., Satyam, N., Rosi, A., Pradhan, B., and Segoni, S.: Usage of antecedent soil moisture for improving the performance of rainfall thresholds for landslide early warning, 200, 105147, <https://doi.org/10.1016/j.catena.2021.105147>, 2021.
- Ahmad, M. U. D. and Bastiaanssen, W. G. M.: Retrieving soil moisture storage in the unsaturated zone using satellite imagery and bi-annual phreatic surface fluctuations, Irrig. Drain. Syst., 17, 141–161, <https://doi.org/10.1023/A:1025101217521>, 2003.
- Al-Shamisi, M. H., Assi, A. H., and Hejase, H. A. N.: Artificial neural networks for predicting global solar radiation in Al Ain City - UAE, Int. J. Green Energy, 10, 443–456, <https://doi.org/10.1080/15435075.2011.641187>, 2013.
- Al-Yaari, A., Wigneron, J. P., Ducharne, A., Kerr, Y., de Rosnay, P., de Jeu, R., Govind, A., Al Bitar, A., Albergel, C., Muñoz-Sabater, J., Richaume, P., and Mialon, A.: Global-scale evaluation of two satellite-based passive microwave soil moisture datasets (SMOS and AMSR-E) with respect to Land Data Assimilation System estimates, Remote Sens. Environ., 149, 181–195, <https://doi.org/10.1016/j.rse.2014.04.006>, 2014.
- Alecci, S. and Rossi, G.: Controllo di qualità dei dati pluviometrici ed analisi delle serie temporali, Siccità. Anal. Monit. e mitigazione. Appl. Sicil. Nuova Ed. Bios, Cosenza, Ital., 2007.
- Aleotti, P.: A warning system for rainfall-induced shallow failures, Eng. Geol., 73, 247–265, <https://doi.org/10.1016/j.enggeo.2004.01.007>, 2004a.
- Aleotti, P.: A warning system for rainfall-induced shallow failures, Eng. Geol., 73, 247–265, <https://doi.org/10.1016/j.enggeo.2004.01.007>, 2004b.
- Alvioli, M. and Baum, R. L.: Parallelization of the TRIGRS model for rainfall-induced landslides using the message passing interface, Environ. Model. Softw., 81, 122–135, <https://doi.org/10.1016/j.envsoft.2016.04.002>, 2016.
- Amicarelli, A., Albano, R., Mirauda, D., Agate, G., Sole, A., and Guandalini, R.: A Smoothed Particle Hydrodynamics model for 3D solid body transport in free surface flows, Comput. Fluids, 116, 205–228, <https://doi.org/10.1016/J.compfluid.2015.04.018>, 2015a.
- Amicarelli, A., Albano, R., Mirauda, D., Agate, G., Sole, A., and Guandalini, R.: A Smoothed Particle Hydrodynamics model for 3D solid body transport in free surface flows, Comput. Fluids, 116, 205–228, <https://doi.org/10.1016/j.compfluid.2015.04.018>, 2015b.
- Amicarelli, A., Kocak, B., Sibilla, S., and Grabe, J.: A 3D smoothed particle hydrodynamics model for erosional dam-break floods, 31, 413–434, <https://doi.org/10.1080/10618562.2017.1422731>, 2017.
- Amicarelli, A., Manenti, S., and Paggi, M.: SPH Modelling of Dam-break Floods, with Damage Assessment to Electrical Substations, 35, 3–21, <https://doi.org/10.1080/10618562.2020.1811240>, 2020a.

-
- Amicarelli, A., Manenti, S., Albano, R., Agate, G., Paggi, M., Longoni, L., Mirauda, D., Ziane, L., Viccione, G., Todeschini, S., Sole, A., Baldini, L. M., Brambilla, D., Papini, M., Khellaf, M. C., Tagliafierro, B., Sarno, L., and Pirovano, G.: SPHERA v.9.0.0: A Computational Fluid Dynamics research code, based on the Smoothed Particle Hydrodynamics mesh-less method, *Comput. Phys. Commun.*, 250, 107157, <https://doi.org/10.1016/J.CPC.2020.107157>, 2020b.
- Amjad, M., Yilmaz, M. T., Yucel, I., and Yilmaz, K. K.: Performance evaluation of satellite- and model-based precipitation products over varying climate and complex topography, *J. Hydrol.*, 584, 124707, <https://doi.org/10.1016/J.JHYDROL.2020.124707>, 2020.
- Anagnosti, P.: Three dimensional stability of fill dams, in: *Proceeding of 7th. International Conference on Soil Mechanics and Foundation Engineering.*, 275–280, 1969.
- Anagnostopoulos, G. G., Fatichi, S., and Burlando, P.: An advanced process-based distributed model for the investigation of rainfall-induced landslides: The effect of process representation and boundary conditions, *Water Resour. Res.*, 51, 7501–7523, <https://doi.org/10.1002/2015WR016909>, 2015.
- Anderson, M. G. and Lloyd, D. M.: Using A Combined Slope Hydrology-Stability Model To Develop Cut Slope Design Charts., *Proc. Inst. Civ. Eng.*, 91, 705–718, 1991.
- Aristizábal, E., García, E., and Martínez, C.: Susceptibility assessment of shallow landslides triggered by rainfall in tropical basins and mountainous terrains, *Nat. Hazards*, 78, 621–634, <https://doi.org/10.1007/s11069-015-1736-4>, 2015.
- Arnone, E., Noto, L. V., Lepore, C., and Bras, R. L.: Physically-based and distributed approach to analyze rainfall-triggered landslides at watershed scale, 133, 121–131, <https://doi.org/10.1016/j.geomorph.2011.03.019>, 2011.
- Ashwood, W.: Numerical model for the prediction of total dynamic landslide forces on flexible barriers, 175, 2014.
- Bajpai, P. and Kumar, M.: Genetic algorithm—an approach to solve global optimization problems, *Indian J. Comput. Sci. Eng.*, 1, 199–206, 2010.
- Balsamo, G., Viterbo, P., Beijaars, A., van den Hurk, B., Hirschi, M., Betts, A. K., and Scipal, K.: A revised hydrology for the ECMWF model: Verification from field site to terrestrial water storage and impact in the integrated forecast system, *J. Hydrometeorol.*, 10, 623–643, <https://doi.org/10.1175/2008JHM1068.1>, 2009.
- Balsamo, G., Boussetta, S., Dutra, E., Beljaars, A., Viterbo, P., and Van den Hurk, B.: Evolution of land surface processes in the IFS, *ECMWF Newsl.*, 127, 78, 2011.
- Balsamo, G., Albergel, C., Beljaars, A., Boussetta, S., Brun, E., Cloke, H., Dee, D., Dutra, E., Muñoz-Sabater, J., Pappenberger, F., De Rosnay, P., Stockdale, T., and Vitart, F.: ERA-Interim/Land: A global land surface reanalysis data set, *Hydrol. Earth Syst. Sci.*, 19, 389–407, <https://doi.org/10.5194/hess-19-389-2015>, 2015.
- Balsamo, G., Agustí-Panareda, A., Albergel, C., Arduini, G., Beljaars, A., Bidlot, J., Bousserez, N., Boussetta, S., Brown, A., Buizza, R., Buontempo, C., Chevallier, F., Choulga, M., Cloke, H., Cronin, M. F., Dahoui, M., Rosnay, P. De, Dirmeyer, P. A., Drusch, M., Dutra, E., Ek, M. B., Gentine, P., Hewitt, H., Keeley, S. P. E., Kerr, Y., Kumar, S., Lupu, C., Mahfouf, J. F., McNorton, J., Mecklenburg, S., Mogensen, K., Muñoz-Sabater, J., Orth, R., Rabier, F., Reichle, R., Ruston, B., Pappenberger, F., Sandu, I., Seneviratne, S. I., Tietsche, S., Trigo, I. F., Uijlenhoet, R., Wedi, N., Woolway, R. I., and Zeng, X.: Satellite and in situ observations for advancing

-
- global earth surface modelling: A review, *Remote Sens.*, 10, 1–72, <https://doi.org/10.3390/rs10122038>, 2018.
- Balzano, B., Tarantino, A., Nicotera, M. V., Forte, G., de Falco, M., and Santo, A.: Building physically based models for assessing rainfall-induced shallow landslide hazard at catchment scale: Case study of the Sorrento Peninsula (Italy), *Can. Geotech. J.*, 56, 1291–1303, <https://doi.org/10.1139/cgj-2017-0611>, 2019.
- Bar, N., Kostadinovski, M., Tucker, M., Byng, G., Rachmatullah, R., Maldonado, A., Pötsch, M., Gaich, A., McQuillan, A., and Yacoub, T.: Rapid and robust slope failure appraisal using aerial photogrammetry and 3D slope stability models, *Int. J. Min. Sci. Technol.*, 30, 651–658, <https://doi.org/10.1016/j.ijmst.2020.05.013>, 2020.
- Barbero, G., Moisello, U., and Todeschini, S.: Evaluation of the Areal Reduction Factor in an Urban Area through Rainfall Records of Limited Length: A Case Study, *J. Hydrol. Eng.*, 19, 05014016, [https://doi.org/10.1061/\(ASCE\)HE.1943-5584.0001022](https://doi.org/10.1061/(ASCE)HE.1943-5584.0001022), 2014.
- Baum, R. L. and Godt, J. W.: Early warning of rainfall-induced shallow landslides and debris flows in the USA, 7, 259–272, <https://doi.org/10.1007/s10346-009-0177-0>, 2010.
- Baum, R. L., Savage, W. Z., and Godt, J. W.: TRIGRS-A Fortran Program for Transient Rainfall Infiltration and Grid-Based Regional Slope-Stability Analysis, 2002.
- Baum, R. L., Godt, J. W., and Savage, W. Z.: Estimating the timing and location of shallow rainfall-induced landslides using a model for transient, unsaturated infiltration, *J. Geophys. Res. Earth Surf.*, 115, <https://doi.org/10.1029/2009JF001321>, 2010.
- Beck, H. E., Vergopolan, N., Pan, M., Levizzani, V., van Dijk, A. I. J. M., Weedon, G. P., Brocca, L., Pappenberger, F., Huffman, G. J., and Wood, E. F.: Global-scale evaluation of 22 precipitation datasets using gauge observations and hydrological modeling, *Adv. Glob. Chang. Res.*, 69, 625–653, https://doi.org/10.1007/978-3-030-35798-6_9, 2020.
- Beck, H. E., Pan, M., Miralles, D. G., Reichle, R. H., Dorigo, W. A., Hahn, S., Sheffield, J., Karthikeyan, L., Balsamo, G., Parinussa, R. M., van Dijk, A. I. J. M., Du, J., Kimball, J. S., Vergopolan, N., and Wood, E. F.: Evaluation of 18 satellite- And model-based soil moisture products using in situ measurements from 826 sensors, *Hydrol. Earth Syst. Sci.*, 25, 17–40, <https://doi.org/10.5194/hess-25-17-2021>, 2021.
- Bellugi, D., Milledge, D. G., Dietrich, W. E., McKean, J. A., Perron, J. T., Sudderth, E. B., and Kazian, B.: A spectral clustering search algorithm for predicting shallow landslide size and location, *J. Geophys. Res. Earth Surf.*, 120, 300–324, <https://doi.org/10.1002/2014JF003137>, 2015.
- Belo-Pereira, M., Dutra, E., and Viterbo, P.: Evaluation of global precipitation data sets over the Iberian Peninsula, *J. Geophys. Res. Atmos.*, 116, 1–16, <https://doi.org/10.1029/2010JD015481>, 2011.
- Bengtsson, L., Hagemann, S., and Hodges, K. I.: Can climate trends be calculated from reanalysis data?, *J. Geophys. Res. D Atmos.*, 109, 1–8, <https://doi.org/10.1029/2004JD004536>, 2004.
- Berti, M., Martina, M. L. V., Franceschini, S., Pignone, S., Simoni, A., and Pizziolo, M.: Probabilistic rainfall thresholds for landslide occurrence using a Bayesian approach, *J. Geophys. Res. Earth Surf.*, 117, 1–20, <https://doi.org/10.1029/2012JF002367>, 2012.
-

-
- Bezák, N., Jemec Auflič, M., and Mikoš, M.: Reanalysis of soil moisture used for rainfall thresholds for rainfall-induced landslides: The Italian case study, 13, 1–14, <https://doi.org/10.3390/w13141977>, 2021.
- BISHOP and W., A.: The use of the slip circle in the stability analysis of slopes, 5, 7–17, 1955.
- Bogaard, T. and Greco, R.: Invited perspectives: Hydrological perspectives on precipitation intensity-duration thresholds for landslide initiation: Proposing hydro-meteorological thresholds, *Nat. Hazards Earth Syst. Sci.*, 18, 31–39, <https://doi.org/10.5194/nhess-18-31-2018>, 2018.
- Bordoni, M., Persichillo, M. G., Meisina, C., Cevasco, A., Giannecchini, R., D’Amato Avanzi, G., Galanti, Y., Bartelletti, C., Brandolini, P., and Zizioli, D.: Developing and testing a data-driven methodology for shallow landslide susceptibility assessment: Preliminary results, *Rend. Online Soc. Geol. Ital.*, 35, 25–28, <https://doi.org/10.3301/ROL.2015.55>, 2015a.
- Bordoni, M., Meisina, C., Valentino, R., Lu, N., Bittelli, M., and Chersich, S.: Hydrological factors affecting rainfall-induced shallow landslides : From the field monitoring to a simplified slope stability analysis, 193, 19–37, <https://doi.org/10.1016/j.enggeo.2015.04.006>, 2015b.
- Bordoni, M., Meisina, C., Valentino, R., Bittelli, M., and Chersich, S.: Site-specific to local-scale shallow landslides triggering zones assessment using TRIGRS, 1025–1050, <https://doi.org/10.5194/nhess-15-1025-2015>, 2015c.
- Bordoni, M., Bittelli, M., Valentino, R., Chersich, S., and Meisina, C.: Improving the estimation of complete field soil water characteristic curves through field monitoring data, *J. Hydrol.*, 552, 283–305, <https://doi.org/10.1016/j.jhydrol.2017.07.004>, 2017.
- Bordoni, M., Corradini, B., Lucchelli, L., Valentino, R., Bittelli, M., Vivaldi, V., and Meisina, C.: Empirical and physically based thresholds for the occurrence of shallow landslides in a prone area of Northern Italian Apennines, 11, <https://doi.org/10.3390/W11122653>, 2019.
- Bowman, E. T., Take, W. A., Rait, K. L., and Hann, C.: Physical models of rock avalanche spreading behaviour with dynamic fragmentation, *Can. Geotech. J.*, 49, 460–476, <https://doi.org/10.1139/T2012-007>, 2012.
- Brien, D. L. and Reid, M. E.: Modeling 3-D Slope Stability of Coastal Bluffs , Using 3-D Ground-Water Flow , Southwestern Seattle , Washington, *Sci. Investig. Rep.* 2007-5092, 61, 2007.
- Brocca, L., Ciabatta, L., Moramarco, T., Ponziani, F., Berni, N., and Wagner, W.: Use of Satellite Soil Moisture Products for the Operational Mitigation of Landslides Risk in Central Italy, Elsevier Inc., 231–247 pp., <https://doi.org/10.1016/B978-0-12-803388-3.00012-7>, 2016.
- Brocca, L., Ciabatta, L., Massari, C., Camici, S., and Tarpanelli, A.: Soil moisture for hydrological applications: Open questions and new opportunities, 9, <https://doi.org/10.3390/w9020140>, 2017.
- Brooks, R. H. and Corey, A. T.: Properties of Porous Media Affecting Fluid Flow, *J. Irrig. Drain. Div.*, 92, 61–88, <https://doi.org/10.1061/jrcea4.0000425>, 1964.
- Brunetti, M. T., Peruccacci, S., Rossi, M., Luciani, S., Valigi, D., and Guzzetti, F.: Rainfall thresholds for the possible occurrence of landslides in Italy, *Nat. Hazards Earth*
-

-
- Syst. Sci., 10, 447–458, <https://doi.org/10.5194/nhess-10-447-2010>, 2010.
- Busscher, W. J.: Field Estimation of Soil Water Content: A review, *J. Soil Water Conserv.*, 64, 116A-116A, <https://doi.org/10.2489/jswc.64.4.116a>, 2009.
- Caine, N.: The Rainfall Intensity: Duration Control of Shallow Landslides and Debris Flows, *Geogr. Ann. Ser. A, Phys. Geogr.*, 62, 23–27, <https://doi.org/10.2307/520449>, 1980.
- Calvello, M. and Pecoraro, G.: FranelItalia: a catalog of recent Italian landslides, 5, <https://doi.org/10.1186/s40677-018-0105-5>, 2018.
- Cannon, S. H., Gartner, J. E., Wilson, R. C., Bowers, J. C., and Laber, J. L.: Storm rainfall conditions for floods and debris flows from recently burned areas in southwestern Colorado and southern California, 96, 250–269, <https://doi.org/10.1016/j.geomorph.2007.03.019>, 2008.
- Cannon, S. H., Boldt, E. M., Laber, J. L., Kean, J. W., and Staley, D. M.: Rainfall intensity-duration thresholds for postfire debris-flow emergency-response planning, *Nat. Hazards*, 59, 209–236, <https://doi.org/10.1007/s11069-011-9747-2>, 2011.
- Capparelli, G.: Applicazione al caso della Calabria centrale. Atti del XXXIII Corso di Aggiornamento in Tecniche di Difesa dall’Inquinamento Title, 203–232, 2012.
- Capparelli, G. and Versace, P.: Analysis of landslide triggering conditions in the Sarno area using a physically based model, *Hydrol. Earth Syst. Sci.*, 18, 3225–3237, <https://doi.org/10.5194/hess-18-3225-2014>, 2014.
- Catani, F., Segoni, S., and Falorni, G.: An empirical geomorphology-based approach to the spatial prediction of soil thickness at catchment scale, *Water Resour. Res.*, 46, 1–15, <https://doi.org/10.1029/2008WR007450>, 2010.
- Chacón, J., Irigaray, C., Fernández, T., and El Hamdouni, R.: Engineering geology maps: Landslides and geographical information systems, *Bull. Eng. Geol. Environ.*, 65, 341–411, <https://doi.org/10.1007/s10064-006-0064-z>, 2006.
- Chae, B. G., Park, H. J., Catani, F., Simoni, A., and Berti, M.: Landslide prediction, monitoring and early warning: a concise review of state-of-the-art, *Geosci. J.*, 21, 1033–1070, <https://doi.org/10.1007/s12303-017-0034-4>, 2017.
- Chakraborty, A. and Goswami, D.: State of the art: Three Dimensional (3D) Slope-Stability Analysis, *Int. J. Geotech. Eng.*, 10, 493–498, <https://doi.org/10.1080/19386362.2016.1172807>, 2016.
- Chen, H. X., Zhang, L. M., Chang, D. S., and Zhang, S.: Mechanisms and runout characteristics of the rainfall-triggered debris flow in Xiaojiagou in Sichuan Province, China, *Nat. Hazards*, 62, 1037–1057, <https://doi.org/10.1007/s11069-012-0133-5>, 2012.
- Chen, Z., Mi, H., Zhang, F., and Wang, X.: A simplified method for 3D slope stability analysis, *Can. Geotech. J.*, 40, 675–683, <https://doi.org/10.1139/t03-002>, 2003.
- Cheng, Y. M. and Yip, C. J.: Three-Dimensional Asymmetrical Slope Stability Analysis Extension of Bishop’s, Janbu’s, and Morgenstern–Price’s Techniques, *J. Geotech. Geoenvironmental Eng.*, 133, 1544–1555, [https://doi.org/10.1061/\(asce\)1090-0241\(2007\)133:12\(1544\)](https://doi.org/10.1061/(asce)1090-0241(2007)133:12(1544)), 2007.
- Chiu, Y. Y., Chen, H. E., and Yeh, K. C.: Investigation of the influence of rainfall runoff on shallow landslides in unsaturated soil using a mathematical model, 11, <https://doi.org/10.3390/w11061178>, 2019.
- Cho, S. E. and Lee, S. R.: Considering Rainfall Characteristics, *Eval. surficial Stab. Homog.*
-

- slopes considering rainfall Charact., 128, 756–763, 2002.
- Collins, B. D. and Znidarcic, D.: Stability Analyses of Rainfall Induced Landslides, *J. Geotech. Geoenvironmental Eng.*, 130, 362–372, [https://doi.org/10.1061/\(asce\)1090-0241\(2004\)130:4\(362\)](https://doi.org/10.1061/(asce)1090-0241(2004)130:4(362)), 2004.
- Collow, T. W., Robock, A., Basara, J. B., and Illston, B. G.: Evaluation of SMOS retrievals of soil moisture over the central United States with currently available in situ observations, *J. Geophys. Res. Atmos.*, 117, 1–15, <https://doi.org/10.1029/2011JD017095>, 2012.
- Conrad, J. L., Morphew, M. D., Baum, R. L., and Mirus, B. B.: HydroMet: A new code for automated objective optimization of hydrometeorological thresholds for landslide initiation, 13, <https://doi.org/10.3390/w13131752>, 2021.
- Conte, E., Donato, A., and Troncone, A.: A simplified method for predicting rainfall-induced mobility of active landslides, 14, 35–45, <https://doi.org/10.1007/S10346-016-0692-8/TABLES/4>, 2017.
- Corominas, J.: The angle of reach as a mobility index for small and large landslides, *Can. Geotech. J.*, 33, 260–271, 1996.
- Crosta, G. B. and Frattini, P.: Distributed modelling of shallow landslides triggered by intense rainfall, *Natural Hazards and Earth System Sciences*, 81–93 pp., 2003.
- Crosta, G. B., Imposimato, S., and Roddeman, D. G.: Numerical modelling of large landslides stability and runout, *Nat. Hazards Earth Syst. Sci.*, 3, 523–538, <https://doi.org/10.5194/nhess-3-523-2003>, 2003.
- Crow, W. T., Berg, A. A., Cosh, M. H., Loew, A., Mohanty, B. P., Panciera, R., De Rosnay, P., Ryu, D., and Walker, J. P.: Upscaling sparse ground-based soil moisture observations for the validation of coarse-resolution satellite soil moisture products, *Rev. Geophys.*, 50, 1–20, <https://doi.org/10.1029/2011RG000372>, 2012.
- Crozier, M. J.: Prediction of rainfall-triggered landslides: a test of the Antecedent Water Status Model, *Earth Surf. Process. Landforms*, 24, 825–833, [https://doi.org/https://doi.org/10.1002/\(SICI\)1096-9837\(199908\)24:9<825::AID-ESP14>3.0.CO;2-M](https://doi.org/https://doi.org/10.1002/(SICI)1096-9837(199908)24:9<825::AID-ESP14>3.0.CO;2-M), 1999.
- Cruden, D. M. and Varnes, D. J.: Landslide types and processes, *Spec. Rep. - Natl. Res. Council. Transp. Res. Board*, 247, 36–75, 1996.
- Dahal, R. K. and Hasegawa, S.: Representative rainfall thresholds for landslides in the Nepal Himalaya, 100, 429–443, <https://doi.org/10.1016/j.geomorph.2008.01.014>, 2008.
- Dai, F. C., Lee, C. F., and Ngai, Y. Y.: Landslide risk assessment and management: an overview, *Eng. Geol.*, 64, 65–87, [https://doi.org/10.1016/S0013-7952\(01\)00093-X](https://doi.org/10.1016/S0013-7952(01)00093-X), 2002.
- Dai, Z., Huang, Y., Cheng, H., and Xu, Q.: 3D numerical modeling using smoothed particle hydrodynamics of flow-like landslide propagation triggered by the 2008 Wenchuan earthquake, *Eng. Geol.*, 180, 21–33, <https://doi.org/10.1016/j.enggeo.2014.03.018>, 2014.
- Dane, J. H. and Hopmans, J. W.: *Methods of Soil Analysis: Part 4 Physical Methods, Methods Soil Anal. Part 4 Phys. Methods*, 5, 671–673, 2002.
- Dane, J. H. and Topp, C. G.: *Methods of soil analysis, Part 4: Physical methods*, John Wiley & Sons, 2020.
- Davies, T. R. H., McSaveney, M. J., and Boulton, C. J.: Elastic strain energy release from

- fragmenting grains: Effects on fault rupture, *J. Struct. Geol.*, 38, 265–277, <https://doi.org/10.1016/j.jsg.2011.11.004>, 2012.
- Deb, K., Pratap, A., Agarwal, S., and Meyarivan, T.: A fast and elitist multiobjective genetic algorithm: NSGA-II, *IEEE Trans. Evol. Comput.*, 6, 182–197, <https://doi.org/10.1109/4235.996017>, 2002.
- Dee, D. P., Uppala, S. M., Simmons, A. J., Berrisford, P., Poli, P., Kobayashi, S., Andrae, U., Balmaseda, M. A., Balsamo, G., Bauer, P., Bechtold, P., Beljaars, A. C. M., van de Berg, L., Bidlot, J., Bormann, N., Delsol, C., Dragani, R., Fuentes, M., Geer, A. J., Haimberger, L., Healy, S. B., Hersbach, H., Hólm, E. V., Isaksen, I., Kållberg, P., Köhler, M., Matricardi, M., McNally, A. P., Monge-Sanz, B. M., Morcrette, J. J., Park, B. K., Peubey, C., de Rosnay, P., Tavolato, C., Thépaut, J. N., and Vitart, F.: The ERA-Interim reanalysis: Configuration and performance of the data assimilation system, *Q. J. R. Meteorol. Soc.*, 137, 553–597, <https://doi.org/10.1002/qj.828>, 2011.
- Delaney, K. B. and Evans, S. G.: The 1997 Mount Munday landslide (British Columbia) and the behaviour of rock avalanches on glacier surfaces, 11, 1019–1036, <https://doi.org/10.1007/s10346-013-0456-7>, 2014.
- Distefano, P., Peres, D. J., Scandura, P., and Cancelliere, A.: Brief communication: Rainfall thresholds based on Artificial neural networks can improve landslide early warning, <https://doi.org/10.5194/nhess-2021-206>, 2021.
- Dorigo, W., Wagner, W., Albergel, C., Albrecht, F., Balsamo, G., Brocca, L., Chung, D., Ertl, M., Forkel, M., Gruber, A., Haas, E., Hamer, P. D., Hirschi, M., Ikonen, J., de Jeu, R., Kidd, R., Lahoz, W., Liu, Y. Y., Miralles, D., Mistelbauer, T., Nicolai-Shaw, N., Parinussa, R., Pratola, C., Reimer, C., van der Schalie, R., Seneviratne, S. I., Smolander, T., and Lecomte, P.: ESA CCI Soil Moisture for improved Earth system understanding: State-of-the art and future directions, *Remote Sens. Environ.*, 203, 185–215, <https://doi.org/10.1016/j.rse.2017.07.001>, 2017.
- Eberhardt, E., Clague, J. J., and Stead, D.: Landslide monitoring: the role of investigative monitoring to improve understanding and early warning of failure, *Landslides Types, Mech. Model.* Ed. by Clague, JJ Stead, D., Cambridge Univ. Press. Cambridge, UK, 222–234, 2012.
- Entekhabi, B. D., Njoku, E. G., Neill, P. E. O., Kellogg, K. H., Crow, W. T., Edelstein, W. N., Entin, J. K., Goodman, S. D., Jackson, T. J., Johnson, J., Kimball, J., Piepmeier, J. R., Koster, R. D., Martin, N., McDonald, K. C., Moggaddam, M., Moran, S., Reichle, R., Shi, J. C., Spencer, M. W., Thurman, S. W., Tsang, L., and Zyl, J. Van: (SMAP) Mission, 98, 2015.
- Fan, L., Lehmann, P., and Or, D.: Load redistribution rules for progressive failure in shallow landslides: Threshold mechanical models, *Geophys. Res. Lett.*, 44, 228–235, <https://doi.org/10.1002/2016GL071763>, 2017.
- FAO: Digital soil map of the world (DSMW). Tech. rep., Food and Agriculture Organization of the United Nations, 2003.
- Fawcett, T.: An introduction to ROC analysis, *Pattern Recognit. Lett.*, 27, 861–874, <https://doi.org/10.1016/j.patrec.2005.10.010>, 2006.
- FELLENIUS and W.: Calculation of stability of earth dam, *Trans. 2nd Congr. Large Dams*, Washington, D. C., 1936, 4, 445–462, 1936.
- Finlay, P. J., Fell, R., and Maguire, P. K.: The relationship between the probability of landslide occurrence and rainfall, *Can. Geotech. J.*, 34, 811–824,

- <https://doi.org/10.1139/t97-047>, 1997.
- Fiorillo, F., Guadagno, F., Aquino, S., and De Blasio, A.: The December 1999 Cervinara landslides: Further debris flows in the pyroclastic deposits of Campania (Southern Italy), *Bull. Eng. Geol. Environ.*, 60, 171–184, <https://doi.org/10.1007/s100640000093>, 2001.
- Ford, T. W. and Quiring, S. M.: Comparison of Contemporary In Situ, Model, and Satellite Remote Sensing Soil Moisture With a Focus on Drought Monitoring, *Water Resour. Res.*, 1565–1582, <https://doi.org/10.1029/2018WR024039>, 2019.
- Froese, C. R., Charriere, M., Humair, F., Jaboyedoff, M., And Pedrazzini, A.: 25 Characterization and management of rockslide hazard at Turtle Mountain, Alberta, Canada, *Landslides Types, Mech. Model.*, 310, 2012.
- Froude, M. J. and Petley, D. N.: Global fatal landslide occurrence from 2004 to 2016, *Nat. Hazards Earth Syst. Sci.*, 18, 2161–2181, <https://doi.org/10.5194/nhess-18-2161-2018>, 2018.
- Gain, A. K., Bühler, Y., Haegeli, P., Molinari, D., Parise, M., Peres, D. J., Pinto, J. G., Trigo, R. M., Llasat, M. C., and Kreibich, H.: Brief Communication : Key papers of 20 years in Natural Hazards and Earth System Sciences, 1–13, 2021.
- GARDNER, W. R.: SOME STEADY-STATE SOLUTIONS OF THE UNSATURATED MOISTURE FLOW EQUATION WITH APPLICATION TO EVAPORATION FROM A WATER TABLE, *Soil Sci.*, 85, 1958.
- Gariano, S. L. and Guzzetti, F.: Landslides in a changing climate, *Earth-Science Rev.*, 162, 227–252, <https://doi.org/10.1016/J.EARSCIREV.2016.08.011>, 2016.
- Gariano, S. L., Brunetti, M. T., Iovine, G., Melillo, M., Peruccacci, S., Terranova, O., Vennari, C., and Guzzetti, F.: Calibration and validation of rainfall thresholds for shallow landslide forecasting in Sicily, southern Italy, 228, 653–665, <https://doi.org/10.1016/j.geomorph.2014.10.019>, 2015.
- Gelaro, R., McCarty, W., Suárez, M. J., Todling, R., Molod, A., Takacs, L., Randles, C. A., Darmenov, A., Bosilovich, M. G., Reichle, R., Wargan, K., Coy, L., Cullather, R., Draper, C., Akella, S., Buchard, V., Conaty, A., da Silva, A. M., Gu, W., Kim, G. K., Koster, R., Lucchesi, R., Merkova, D., Nielsen, J. E., Partyka, G., Pawson, S., Putman, W., Rienecker, M., Schubert, S. D., Sienkiewicz, M., and Zhao, B.: The modern-era retrospective analysis for research and applications, version 2 (MERRA-2), *J. Clim.*, 30, 5419–5454, <https://doi.org/10.1175/JCLI-D-16-0758.1>, 2017.
- Van Genuchten, M. T.: A closed-form equation for predicting the hydraulic conductivity of unsaturated soils, *Soil Sci. Soc. Am. J.*, 44, 892–898, 1980.
- Giannecchini, R., Galanti, Y., and D’Amato Avanzi, G.: Critical rainfall thresholds for triggering shallow landslides in the Serchio River Valley (Tuscany, Italy), *Nat. Hazards Earth Syst. Sci.*, 12, 829–842, <https://doi.org/10.5194/nhess-12-829-2012>, 2012.
- Glade, T., Crozier, M., and Smith, P.: Applying probability determination to refine landslide-triggering rainfall thresholds using an empirical “Antecedent Daily Rainfall Model,” *Pure Appl. Geophys.*, 157, 1059–1079, <https://doi.org/10.1007/s000240050017>, 2000.
- Godt, J. W., Baum, R. L., Savage, W. Z., Salciarini, D., Schulz, W. H., and Harp, E. L.: Transient deterministic shallow landslide modeling: Requirements for susceptibility and hazard assessments in a GIS framework, *Eng. Geol.*, 102, 214–

-
- 226, <https://doi.org/10.1016/j.enggeo.2008.03.019>, 2008.
- Gruber, A., Dorigo, W. A., Crow, W., and Wagner, W.: Triple Collocation-Based Merging of Satellite Soil Moisture Retrievals, *IEEE Trans. Geosci. Remote Sens.*, 55, 6780–6792, <https://doi.org/10.1109/TGRS.2017.2734070>, 2017.
- Gruber, A., Scanlon, T., Van Der Schalie, R., Wagner, W., and Dorigo, W.: Evolution of the ESA CCI Soil Moisture climate data records and their underlying merging methodology, *Earth Syst. Sci. Data*, 11, 717–739, <https://doi.org/10.5194/essd-11-717-2019>, 2019.
- Guandalini, R., Agate, G., Manenti, S., Sibilla, S., and Gallati, M.: Innovative numerical modeling to investigate local scouring problems induced by fluvial structures, 2012.
- Guandalini, R., Agate, G., Manenti, S., Sibilla, S., and Gallati, M.: SPH Based Approach toward the Simulation of Non-cohesive Sediment Removal by an Innovative Technique Using a Controlled Sequence of Underwater Micro-explosions, *Procedia IUTAM*, 18, 28–39, <https://doi.org/10.1016/J.PIUTAM.2015.11.004>, 2015.
- Guidicini, G. and Iwasa, O. Y.: Essai de correlation entre la pluviosite et les glissements de terrain sous climat tropical humide, *Bull. Int. Assoc. Eng. Geol. - Bull. l'Association Int. Géologie l'Ingénieur*, 16, 13–20, <https://doi.org/10.1007/BF02591434>, 1977.
- Guzzetti, F., Peruccacci, S., Rossi, M., and Stark, C. P.: Rainfall thresholds for the initiation of landslides in central and southern Europe, *Meteorol. Atmos. Phys.*, 98, 239–267, <https://doi.org/10.1007/s00703-007-0262-7>, 2007a.
- Guzzetti, F., Peruccacci, S., Rossi, M., and Stark, C. P.: Rainfall thresholds for the initiation of landslides in central and southern Europe, *Meteorol. Atmos. Phys.*, 98, 239–267, <https://doi.org/10.1007/s00703-007-0262-7>, 2007b.
- Guzzetti, F., Peruccacci, S., Rossi, M., and Stark, C. P.: Rainfall thresholds for the initiation of landslides in central and southern Europe, *Meteorol. Atmos. Phys.*, 98, 239–267, <https://doi.org/10.1007/s00703-007-0262-7>, 2007c.
- Guzzetti, F., Peruccacci, S., Rossi, M., and Stark, C. P.: The rainfall intensity-duration control of shallow landslides and debris flows: An update, 5, 3–17, <https://doi.org/10.1007/s10346-007-0112-1>, 2008a.
- Guzzetti, F., Peruccacci, S., Rossi, M., and Stark, C. P.: The rainfall intensity-duration control of shallow landslides and debris flows: An update, 5, 3–17, <https://doi.org/10.1007/s10346-007-0112-1>, 2008b.
- Hagan, D. F. T., Parinussa, R. M., Wang, G., and Draper, C. S.: An evaluation of soil moisture anomalies from global model-based datasets over the people's Republic of China, 12, <https://doi.org/10.3390/w12010117>, 2020.
- Haines, W. B.: Studies in the physical properties of soil. V. The hysteresis effect in capillary properties, and the modes of moisture distribution associated therewith, *J. Agric. Sci.*, 20, 97–116, <https://doi.org/DOI:10.1017/S002185960008864X>, 1930.
- Hammond C., Hall D., Miller S., S. P.: Level Stability Analysis (LISA) Documentation for Version 2.0, 1992.
- Han, X., Li, X., He, G., Kumbhar, P., Montzka, C., Kollet, S., Miyoshi, T., Rosolem, R., Zhang, Y., Vereecken, H., and Franssen, H.-J. H.: DasPy 1.0 -- the Open Source Multivariate Land Data Assimilation Framework in combination with the Community Land Model 4.5, *Geosci. Model Dev. Discuss.*, 8, 7395–7444,
-

-
- <https://doi.org/10.5194/gmdd-8-7395-2015>, 2015.
- Haykin, S.: A comprehensive foundation, 2, 41, 2004.
- He, J., Qiu, H., Qu, F., Hu, S., Yang, D., Shen, Y., Zhang, Y., Sun, H., and Cao, M.: Prediction of spatiotemporal stability and rainfall threshold of shallow landslides using the TRIGRS and Scoops3D models, 197, 104999, <https://doi.org/10.1016/j.catena.2020.104999>, 2021.
- Hersbach, H., Bell, B., Berrisford, P., Hirahara, S., Horányi, A., Muñoz-Sabater, J., Nicolas, J., Peubey, C., Radu, R., Schepers, D., Simmons, A., Soci, C., Abdalla, S., Abellan, X., Balsamo, G., Bechtold, P., Biavati, G., Bidlot, J., Bonavita, M., De Chiara, G., Dahlgren, P., Dee, D., Diamantakis, M., Dragani, R., Flemming, J., Forbes, R., Fuentes, M., Geer, A., Haimberger, L., Healy, S., Hogan, R. J., Hólm, E., Janisková, M., Keeley, S., Laloyaux, P., Lopez, P., Lupu, C., Radnoti, G., de Rosnay, P., Rozum, I., Vamborg, F., Villaume, S., and Thépaut, J. N.: The ERA5 global reanalysis, Q. J. R. Meteorol. Soc., 146, 1999–2049, <https://doi.org/10.1002/qj.3803>, 2020.
- Highland, L. M. and Bobrowsky, P.: The landslide Handbook - A guide to understanding landslides, US Geol. Surv. Circ., 1–147, <https://doi.org/10.3133/cir1325>, 2008.
- Hong, Y., Hiura, H., Shino, K., Sassa, K., Suemine, A., Fukuoka, H., and Wang, G.: The influence of intense rainfall on the activity of large-scale crystalline schist landslides in Shikoku Island, Japan, 2, 97–105, <https://doi.org/10.1007/s10346-004-0043-z>, 2005.
- Hong, Y., Alder, R., and Huffman, G.: Evaluation of the potential of NASA multi-satellite precipitation analysis in global landslide hazard assessment, Geophys. Res. Lett., 33, <https://doi.org/10.1029/2006GL028010>, 2006.
- Hopmans, J. W.: Infiltration and Unsaturated Zone, Treatise Water Sci., 2, 103–114, <https://doi.org/10.1016/B978-0-444-53199-5.00031-2>, 2011.
- Horton, R. E.: The role of infiltration in the hydrology cycle, Trans. Am. Geophys. Union, 446–460, 1931.
- Hu, M., Liu, M. B., Xie, M. W., and Liu, G. R.: Three-dimensional run-out analysis and prediction of flow-like landslides using smoothed particle hydrodynamics, Environ. Earth Sci., 73, 1629–1640, <https://doi.org/10.1007/s12665-014-3513-1>, 2015.
- Huang, C.-C., Tsai, C.-C., and Chen, Y.-H.: Generalized Method for Three-Dimensional Slope Stability Analysis, J. Geotech. Geoenvironmental Eng., 128, 836–848, [https://doi.org/10.1061/\(asce\)1090-0241\(2002\)128:10\(836\)](https://doi.org/10.1061/(asce)1090-0241(2002)128:10(836)), 2002.
- Hübl, J., Suda, J., Proske, D., Kaitna, R., and Scheidl, C.: Debris Flow Impact Estimation, Int. Symp. Water Manag. Hydraul. Eng., 137–148, 2009.
- Von Huene, R., Miller, J. J., and Dartnell, P.: A possible transoceanic tsunami directed toward the U.S. west coast from the Semidi segment, Alaska convergent margin, Geochemistry, Geophys. Geosystems, 17, 645–659, <https://doi.org/10.1002/2015GC006147>, 2016.
- Hungr, O.: An extension of Bishop's simplified method of slope stability analysis to three dimensions, 37, 113–117, <https://doi.org/10.1680/geot.1987.37.1.113>, 1987.
- Hungr, O. and Evans, S. G.: Entrainment of debris in rock avalanches: An analysis of a long run-out mechanism, Bull. Geol. Soc. Am., 116, 1240–1252, <https://doi.org/10.1130/B25362.1>, 2004.
- Hungr, O., Salgado, F. M., and Byrne, P. M.: Evaluation of a three-dimensional method of
-

-
- slope stability analysis, *Can. Geotech. J.*, 26, 679–686, <https://doi.org/10.1139/t89-079>, 1989.
- Hunter, G. and Fell, R.: Travel distance angle for “rapid” landslides in constructed and natural soil slopes, *Can. Geotech. J.*, 40, 1123–1141, <https://doi.org/10.1139/t03-061>, 2003.
- Indoria, A. K., Sharma, K. L., and Reddy, K. S.: Hydraulic properties of soil under warming climate, *LTD*, 473–508 pp., <https://doi.org/10.1016/b978-0-12-818032-7.00018-7>, 2020.
- Innes, J. L.: Debris flows, *Prog. Phys. Geogr. Earth Environ.*, 7, 469–501, <https://doi.org/10.1177/030913338300700401>, 1983a.
- Innes, J. L.: Debris flows, *Prog. Phys. Geogr. Earth Environ.*, 7, 469–501, <https://doi.org/10.1177/030913338300700401>, 1983b.
- Iverson, R. M.: Landslide triggering by rain infiltration, *Water Resour. Res.*, 36, 1897–1910, <https://doi.org/10.1029/2000WR900090>, 2000a.
- Iverson, R. M.: Landslide triggering by rain infiltration *iverson_wrr_july2000.pdf*, 36, 1897–1910, 2000b.
- Iverson, R. M.: Elementary theory of bed-sediment entrainment by debris flows and avalanches, *J. Geophys. Res. Earth Surf.*, 117, 1–17, <https://doi.org/10.1029/2011JF002189>, 2012.
- Iverson, R. M., Reid, M. E., Logan, M., LaHusen, R. G., Godt, J. W., and Griswold, J. P.: Positive feedback and momentum growth during debris-flow entrainment of wet bed sediment, *Nat. Geosci.*, 4, 116–121, <https://doi.org/10.1038/ngeo1040>, 2011.
- Jakob, M. and Weatherly, H.: A hydroclimatic threshold for landslide initiation on the North Shore Mountains of Vancouver, British Columbia, 54, 137–156, [https://doi.org/10.1016/S0169-555X\(02\)00339-2](https://doi.org/10.1016/S0169-555X(02)00339-2), 2003.
- Jakob, M., McDougall, S., Weatherly, H., and Ripley, N.: Debris-flow simulations on Cheekye River, British Columbia, 10, 685–699, <https://doi.org/10.1007/s10346-012-0365-1>, 2013.
- Janbu, N.: Application of composite slip surface for stability analysis, in: *Proceedings of European Conference on Stability of Earth Slopes, Sweden, 1954*, 43–49, 1954.
- Janbu, N.: Earth Pressures and Bearing Capacity Calculations by Generalized Procédure of Slices, *Proc. 4th Int. Conf. Soil Mech. Found. Eng.*, 207–212, 1957.
- Jeremić, B.: Finite element methods for 3D slope stability analysis, *Proc. Sess. Geo-Denver 2000 - Slope Stab. 2000*, *GSP* 101, 289, 224–238, [https://doi.org/10.1061/40512\(289\)17](https://doi.org/10.1061/40512(289)17), 2000.
- Jiang, Q., Li, W., Fan, Z., He, X., Sun, W., Chen, S., Wen, J., Gao, J., and Wang, J.: Evaluation of the ERA5 reanalysis precipitation dataset over Chinese Mainland, *J. Hydrol.*, 595, 125660, <https://doi.org/10.1016/J.JHYDROL.2020.125660>, 2021.
- Jiao, D., Xu, N., Yang, F., and Xu, K.: Evaluation of spatial-temporal variation performance of ERA5 precipitation data in China, <https://doi.org/10.1038/s41598-021-97432-y>, 2021.
- Julian, M. and Anthony, E.: Aspects of landslide activity in the Mercantour Massif and the French Riviera, southeastern France, 15, 275–289, [https://doi.org/10.1016/0169-555X\(95\)00075-G](https://doi.org/10.1016/0169-555X(95)00075-G), 1996.
- Kalnay, E., Kanamitsu, M., Kistler, R., Collins, W., Deaven, D., and Gandin, L.: *The NCEP / NCAR 40-Year Reanalysis Project*, 1996.
-

-
- Kawanishi, T., Sezai, T., Ito, Y., Imaoka, K., Takeshima, T., Ishido, Y., Shibata, A., Miura, M., Inahata, H., and Spencer, R. W.: The Advanced Microwave Scanning Radiometer for the Earth Observing System (AMSR-E), NASDA's contribution to the EOS for global energy and water cycle studies, *IEEE Trans. Geosci. Remote Sens.*, 41, 184–194, <https://doi.org/10.1109/TGRS.2002.808331>, 2003.
- Kerr, Y. H.: Soil moisture from space: Where are we?, *Hydrogeol. J.*, 15, 117–120, <https://doi.org/10.1007/s10040-006-0095-3>, 2007.
- Kerr, Y. H., Waldteufel, P., Wigneron, J. P., Delwart, S., Cabot, F., Boutin, J., Escorihuela, M. J., Font, J., Reul, N., Gruhier, C., Juglea, S. E., Drinkwater, M. R., Hahne, A., Martin-Neira, M., and Mecklenburg, S.: The SMOS L: New tool for monitoring key elements of the global water cycle, *Proc. IEEE*, 98, 666–687, <https://doi.org/10.1109/JPROC.2010.2043032>, 2010.
- Kherif, F. and Latypova, A.: Principal component analysis, *Mach. Learn. Methods Appl. to Brain Disord.*, 209–225, <https://doi.org/10.1016/B978-0-12-815739-8.00012-2>, 2019.
- Kong, X., Dorling, S., and Smith, R.: Soil moisture modelling and validation at an agricultural site in Norfolk using the Met Office surface exchange scheme (MOSES), *Meteorol. Appl.*, 18, 18–27, <https://doi.org/10.1002/met.197>, 2011.
- Koster, R. D., Guo, Z., Yang, R., Dirmeyer, P. A., Mitchell, K., and Puma, M. J.: On the nature of soil moisture in land surface models, *J. Clim.*, 22, 4322–4335, <https://doi.org/10.1175/2009JCLI2832.1>, 2009.
- Kosugi, K., Hopmans, J. W., and Dane, J. H.: 3.3.4 Parametric Models, <https://doi.org/https://doi.org/10.2136/sssabookser5.4.c27>, January 2002.
- Kwan, J. S. H.: Supplementary Technical Guidance on Design of Rigid Debris-resisting Barriers, GEO Report, 2012.
- Lagamarsino, D., Segoni, S., Fanti, R., and Catani, F.: Updating and tuning a regional-scale landslide early warning system, 10, 91–97, <https://doi.org/10.1007/s10346-012-0376-y>, 2013.
- Lam, L. and Fredlund, D. G.: A general limit equilibrium model for three-dimensional slope stability analysis, *Can. Geotech. J.*, 30, 905–919, <https://doi.org/10.1139/t93-089>, 1993.
- Lee, W. Y., Park, S. K., and Sung, H. H.: The optimal rainfall thresholds and probabilistic rainfall conditions for a landslide early warning system for Chuncheon, Republic of Korea, 18, 1721–1739, <https://doi.org/10.1007/s10346-020-01603-3>, 2021.
- Legros, F.: Landslide mobility and the role of water, in: *Landslides from massive rock slope failure*, vol. 49, Springer Dordrecht, 233–242, 2006.
- Lehmann, P. and Or, D.: Hydromechanical triggering of landslides: From progressive local failures to mass release, *Water Resour. Res.*, 48, <https://doi.org/10.1029/2011WR010947>, 2012.
- Leonarduzzi, E., Molnar, P., and McArdell, B. W.: Predictive performance of rainfall thresholds for shallow landslides in Switzerland from gridded daily data, *Water Resour. Res.*, 53, 6612–6625, <https://doi.org/10.1002/2017WR021044>, 2017a.
- Leonarduzzi, E., Molnar, P., and McArdell, B. W.: Predictive performance of rainfall thresholds for shallow landslides in Switzerland from gridded daily data, *Water Resour. Res.*, 53, 6612–6625, <https://doi.org/10.1002/2017WR021044>, 2017b.
- Lepore, C., Arnone, E., Noto, L. V., Sivandran, G., and Bras, R. L.: Physically based modeling of rainfall-triggered landslides: A case study in the Luquillo forest,

-
- Puerto Rico, *Hydrol. Earth Syst. Sci.*, 17, 3371–3387, <https://doi.org/10.5194/hess-17-3371-2013>, 2013.
- Li Tianchi: A mathematical model for predicting the extent of a major rockfall., *Zeitschrift fur Geomorphol.*, 27, 473–482, <https://doi.org/10.1127/zfg/27/1983/473>, 1983.
- Li, W. C., Lee, L. M., Cai, H., Li, H. J., Dai, F. C., and Wang, M. L.: Combined roles of saturated permeability and rainfall characteristics on surficial failure of homogeneous soil slope, *Eng. Geol.*, 153, 105–113, <https://doi.org/https://doi.org/10.1016/j.enggeo.2012.11.017>, 2013.
- Li, Y. and Mo, P.: A unified landslide classification system for loess slopes: A critical review, 340, 67–83, <https://doi.org/10.1016/j.geomorph.2019.04.020>, 2019.
- Liu, H., Li, G., Cumberland, W. G., and Wu, T.: Testing Statistical Significance of the Area under a Receiving Operating Characteristics Curve for Repeated Measures Design with Bootstrapping, *Test. Stat. Significance Area under a Receiv. Oper. Charact. Curve Repeated Meas. Des. with Bootstrapping*, 3, 257–278, [https://doi.org/10.6339/JDS.2005.03\(3\).206](https://doi.org/10.6339/JDS.2005.03(3).206), 2005.
- Lu, C. Y., Tang, C. L., Chan, Y. C., Hu, J. C., and Chi, C. C.: Forecasting landslide hazard by the 3D discrete element method: A case study of the unstable slope in the Lushan hot spring district, central Taiwan, *Eng. Geol.*, 183, 14–30, <https://doi.org/10.1016/j.enggeo.2014.09.007>, 2014.
- Lu, N. and Godt, J.: Infinite slope stability under steady unsaturated seepage conditions, *Water Resour. Res.*, 44, 1–13, <https://doi.org/10.1029/2008WR006976>, 2008.
- Lucas, A., Mangeney, A., and Ampuero, J. P.: Frictional velocity-weakening in landslides on Earth and on other planetary bodies, *Nat. Commun.*, 5, 1–9, <https://doi.org/10.1038/ncomms4417>, 2014.
- Lumb, P.: Slope failures in Hong Kong, *Q. J. Eng. Geol. Hydrogeol.*, 8, 31–65, <https://doi.org/10.1144/GSL.QJEG.1975.008.01.02>, 1975.
- Mancarella, D. and Hungr, O.: Analysis of run-up of granular avalanches against steep, adverse slopes and protective barriers, *Can. Geotech. J.*, 47, 827–841, <https://doi.org/10.1139/T09-143>, 2010.
- Manenti, Wang, Domínguez, Li, Amicarelli, and Albano: SPH Modeling of Water-Related Natural Hazards, 11, 1875, <https://doi.org/10.3390/w11091875>, 2019.
- Manenti, S., Sibilla, S., Gallati, M., Agate, G., Guandalini, R., Manenti, S., Sibilla, S., Gallati, M., Agate, G., and Guandalini, R.: SPH MODELING OF RAPID MULTIPHASE FLOWS AND SHOCK WAVE PROPAGATION, 2011a.
- Manenti, S., Sibilla, S., Gallati, M., Agate, G., and Guandalini, R.: SPH Simulation of Sediment Flushing Induced by a Rapid Water Flow, *J. Hydraul. Eng.*, 138, 272–284, [https://doi.org/10.1061/\(ASCE\)HY.1943-7900.0000516](https://doi.org/10.1061/(ASCE)HY.1943-7900.0000516), 2011b.
- Manenti, S., Pierobon, ; E, Gallati, ; M, Sibilla, ; S, D'alpaos, ; L, Macchi, ; E, and Todeschini, S.: Vajont Disaster: Smoothed Particle Hydrodynamics Modeling of the Postevent 2D Experiments, *J. Hydraul. Eng.*, 142, 05015007, [https://doi.org/10.1061/\(ASCE\)HY.1943-7900.0001111](https://doi.org/10.1061/(ASCE)HY.1943-7900.0001111), 2016.
- Manenti, S., Amicarelli, A., and Todeschini, S.: WCSPH with limiting viscosity for modeling landslide hazard at the slopes of artificial reservoir, 10, 1–25, <https://doi.org/10.3390/w10040515>, 2018.
- Manenti, S., Amicarelli, A., Palazzolo, N., Bordoni, M., Creaco, E., and Meisina, C.: Post-failure dynamics of rainfall-induced landslide in oltrepò pavese, 12,
-

-
- <https://doi.org/10.3390/w12092555>, 2020.
- Manzanal, D., Drempevic, V., Haddad, B., Pastor, M., Martin Stickle, M., and Mira, P.: Application of a new rheological model to rock avalanches: An SPH approach, *Rock Mech. Rock Eng.*, 49, 2353–2372, <https://doi.org/10.1007/s00603-015-0909-5>, 2016.
- Marin, R. J.: Physically based and distributed rainfall intensity and duration thresholds for shallow landslides, 17, 2907–2917, <https://doi.org/10.1007/s10346-020-01481-9>, 2020.
- Marino, P., Peres, D. J., Cancelliere, A., Greco, R., and Bogaard, T. A.: Soil moisture information can improve shallow landslide forecasting using the hydrometeorological threshold approach, 17, 2041–2054, <https://doi.org/10.1007/s10346-020-01420-8>, 2020.
- Marra, F.: Rainfall thresholds for landslide occurrence: systematic underestimation using coarse temporal resolution data, *Nat. Hazards*, 95, 883–890, <https://doi.org/10.1007/s11069-018-3508-4>, 2019.
- Martelloni, G., Segoni, S., Fanti, R., and Catani, F.: Rainfall thresholds for the forecasting of landslide occurrence at regional scale, 9, 485–495, <https://doi.org/10.1007/s10346-011-0308-2>, 2012.
- Masagus Ahmad Azizi, Irfan Marwanza, M. K. G. and A. A.: Three Dimensional Slope Stability Analysis of Open Pit Mine, 13, 2020.
- Mattia, F., Satalino, G., Pauwels, V. R. N., and Loew, A.: Soil moisture retrieval through a merging of multi-temporal L-band SAR data and hydrologic modelling, *Hydrol. Earth Syst. Sci.*, 13, 343–356, <https://doi.org/10.5194/hess-13-343-2009>, 2009.
- McCall, J.: Genetic algorithms for modelling and optimisation, *J. Comput. Appl. Math.*, 184, 205–222, <https://doi.org/10.1016/j.cam.2004.07.034>, 2005.
- McDougall, S.: 2014 canadian geotechnical colloquium: Landslide runout analysis – current practice and challenges, *Can. Geotech. J.*, 54, 605–620, <https://doi.org/10.1139/cgj-2016-0104>, 2017.
- Melillo, M., Brunetti, M. T., Peruccacci, S., Gariano, S. L., Roccati, A., and Guzzetti, F.: A tool for the automatic calculation of rainfall thresholds for landslide occurrence, *Environ. Model. Softw.*, 105, 230–243, <https://doi.org/10.1016/j.envsoft.2018.03.024>, 2018.
- Méndez-Barroso, L. A., Vivoni, E. R., and Mascaro, G.: Impact of spatially-variable soil thickness and texture on simulated hydrologic conditions in a semiarid watershed in northwest Mexico, *Rev. Mex. Ciencias Geol. Ciencias Geol.*, 33, 365–377, 2016.
- Mercogliano, P., Segoni, S., Rossi, G., Sikorsky, B., Tofani, V., Schiano, P., Catani, F., and Casagli, N.: Brief communication A prototype forecasting chain for rainfall induced shallow landslides, *Nat. Hazards Earth Syst. Sci.*, 13, 771–777, <https://doi.org/10.5194/nhess-13-771-2013>, 2013.
- Milledge, D. G., Bellugi, D., McKean, J. A., Densmore, A. L., and Dietrich, W. E.: A multidimensional stability model for predicting shallow landslide size and shape across landscapes, *J. Geophys. Res. F Earth Surf.*, 119, 2481–2504, <https://doi.org/10.1002/2014JF003135>, 2014.
- Mirus, B. B., Morphew, M. D., and Smith, J. B.: Developing Hydro-Meteorological Thresholds for Shallow Landslide Initiation and Early Warning, *Water* 2018, Vol. 10, Page 1274, 10, 1274, <https://doi.org/10.3390/W10091274>, 2018a.
-

-
- Mirus, B. B., Becker, R. E., Baum, R. L., and Smith, J. B.: Integrating real-time subsurface hydrologic monitoring with empirical rainfall thresholds to improve landslide early warning, 15, 1909–1919, <https://doi.org/10.1007/s10346-018-0995-z>, 2018b.
- Di Monaco, A., Manenti, S., Gallati, M., Sibilla, S., Agate, G., and Guandalini, R.: SPH modeling of solid boundaries through a semi-analytic approach, *Eng. Appl. Comput. Fluid Mech.*, 5, 1–15, <https://doi.org/10.1080/19942060.2011.11015348>, 2011.
- Monaghan, J. J.: Smoothed particle hydrodynamics, *Reports Prog. Phys.*, 68, 1703, 2005.
- Montgomery, D. R. and Dietrich, W. E.: A physically based model for the topographic control on shallow landsliding, *Water Resour. Res.*, 30, 1153–1171, <https://doi.org/10.1029/93WR02979>, 1994.
- Morgenstern, N. R. and Price, V. E.: The Analysis of the Stability of General Slip Surfaces, 15, 79–93, <https://doi.org/10.1680/geot.1965.15.1.79>, 1965.
- Muñoz-Sabater, J., Dutra, E., Agustí-Panareda, A., Albergel, C., Arduini, G., Balsamo, G., Boussetta, S., Choulga, M., Harrigan, S., Hersbach, H., Martens, B., Miralles, D. G., Piles, M., Rodríguez-Fernández, N. J., Zsoter, E., Buontempo, C., and Thépaut, J. N.: ERA5-Land: A state-of-the-art global reanalysis dataset for land applications, *Earth Syst. Sci. Data*, 13, 4349–4383, <https://doi.org/10.5194/essd-13-4349-2021>, 2021.
- Muntohar, A. S. and Liao, H. J.: Analysis of rainfall-induced infinite slope failure during typhoon using a hydrological-geotechnical model, *Environ. Geol.*, 56, 1145–1159, <https://doi.org/10.1007/s00254-008-1215-2>, 2009.
- Nasta, P., Kamai, T., Chirico, G. B., Hopmans, J. W., and Romano, N.: Scaling soil water retention functions using particle-size distribution, *J. Hydrol.*, 374, 223–234, <https://doi.org/10.1016/j.jhydrol.2009.06.007>, 2009.
- Ng, C. W. W., Wang, B., and Tung, Y. K.: Three-dimensional numerical investigations of groundwater responses in an unsaturated slope subjected to various rainfall patterns, *Can. Geotech. J.*, 38, 1049–1062, <https://doi.org/10.1139/cgj-38-5-1049>, 2001.
- Nicoletti, P. G. and Sorriso-Valvo, M.: Geomorphic controls of the shape and mobility of rock avalanches, *Geol. Soc. Am. Bull.*, 103, 1365–1373, [https://doi.org/10.1130/0016-7606\(1991\)103<1365:GCOTSA>2.3.CO;2](https://doi.org/10.1130/0016-7606(1991)103<1365:GCOTSA>2.3.CO;2), 1991.
- Nie, S., Luo, Y., Wu, T., Shi, X., and Wang, Z.: Journal of geophysical research, *Nature*, 175, 238, <https://doi.org/10.1038/175238c0>, 1955.
- Nikolopoulos, E. I., Crema, S., Marchi, L., Marra, F., Guzzetti, F., and Borga, M.: Impact of uncertainty in rainfall estimation on the identification of rainfall thresholds for debris flow occurrence, 221, 286–297, <https://doi.org/10.1016/j.geomorph.2014.06.015>, 2014a.
- Nikolopoulos, E. I., Crema, S., Marchi, L., Marra, F., Guzzetti, F., and Borga, M.: Impact of uncertainty in rainfall estimation on the identification of rainfall thresholds for debris flow occurrence, 221, 286–297, <https://doi.org/10.1016/j.geomorph.2014.06.015>, 2014b.
- Pack, R. T., Tarboton, D. G., and Goodwin, C. N.: Assessing terrain stability in a GIS using SINMAP, 2001.
- Palau, R. M., Hürlimann, M., Berenguer, M., and Sempere-Torres, D.: Towards the use of hydrometeorological thresholds for the regional-scale LEWS of Catalonia (NE Spain), <https://doi.org/10.5194/EGUSPHERE-EGU21-8221>, 2021.
- Papa, M. N., Medina, V., Ciervo, F., and Bateman, A.: Derivation of critical rainfall

- thresholds for shallow landslides as a tool for debris flow early warning systems, *Hydrol. Earth Syst. Sci.*, 17, 4095–4107, <https://doi.org/10.5194/hess-17-4095-2013>, 2013.
- Park, D. W., Nikhil, N. V., and Lee, S. R.: Landslide and debris flow susceptibility zonation using TRIGRS for the 2011 Seoul landslide event, *Nat. Hazards Earth Syst. Sci.*, 13, 2833–2849, <https://doi.org/10.5194/nhess-13-2833-2013>, 2013.
- Pastor, M., Blanc, T., Manzanal, D., Drempevic, V., Pastor, M.J., Sanchez, M., Crosta, G., Imposimato, S., Roddeman, D., et al.: Landslide runout: Review of analytical/empirical models for subaerial slides, submarine slides and snow avalanche. Numerical modelling. Software tools, material models, validation and benchmarking for selected case studies, *Safel. Living with landslide risk Eur. Assessment, Eff. Glob. Chang. risk Manag. Strateg. 7th Framew. Program. Coop. Theme 6 Environ. (including Clim. Chang. Sub-Activity 6.1.3 Nat. Hazards*, 340, 2012.
- Pastor, M., Quecedo, ; M, Gonzá Lez, ; E, Herreros, ; M I, Ferná Ndez Merodo, ; J A, and Mira, P.: Simple Approximation to Bottom Friction for Bingham Fluid Depth Integrated Models, *J. Hydraul. Eng.*, 130, 149–155, [https://doi.org/10.1061/\(ASCE\)0733-9429\(2004\)130:2\(149\)](https://doi.org/10.1061/(ASCE)0733-9429(2004)130:2(149)), 2004.
- Pastor, M., Haddad, B., Sorbino, G., Cuomo, S., and Drempevic, V.: A depth-integrated, coupled SPH model for flow-like landslides and related phenomena, *Int. J. Numer. Anal. Methods Geomech.*, 33, 143–172, <https://doi.org/10.1002/NAG.705>, 2009.
- Pastor, M., Blanc, T., Haddad, B., Petrone, S., Sanchez Morles, M., Drempevic, V., Issler, D., Crosta, G. B., Cascini, L., Sorbino, G., and Cuomo, S.: Application of a SPH depth-integrated model to landslide run-out analysis, 11, 793–812, <https://doi.org/10.1007/s10346-014-0484-y>, 2014.
- Peirce, C. S.: The numerical measure of the success of predictions., *Science*, 4, 453–454, <https://doi.org/10.1126/science.ns-4.93.453-a>, 1884.
- Pelletier, J. D. and Rasmussen, C.: Geomorphically based predictive mapping of soil thickness in upland watersheds, *Water Resour. Res.*, 45, <https://doi.org/10.1029/2008WR007319>, 2009.
- Pelosi, A., Terribile, F., D’Urso, G., and Chirico, G. B.: Comparison of ERA5-Land and UERRA MESCAN-SURFEX reanalysis data with spatially interpolated weather observations for the regional assessment of reference evapotranspiration, 12, <https://doi.org/10.3390/W12061669>, 2020.
- Peng, J., Niesel, J., and Loew, A.: Evaluation of soil moisture downscaling using a simple thermal-based proxy-the REMEDHUS network (Spain) example, *Hydrol. Earth Syst. Sci.*, 19, 4765–4782, <https://doi.org/10.5194/hess-19-4765-2015>, 2015.
- Peng, J., Loew, A., Merlin, O., and Verhoest, N. E. C.: A review of spatial downscaling of satellite remotely sensed soil moisture, *Rev. Geophys.*, 55, 341–366, <https://doi.org/10.1002/2016RG000543>, 2017.
- Peng, J., Albergel, C., Balenzano, A., Brocca, L., Cartus, O., Cosh, M. H., Crow, W. T., Dabrowska-Zielinska, K., Dadson, S., Davidson, M. W. J., de Rosnay, P., Dorigo, W., Gruber, A., Hagemann, S., Hirschi, M., Kerr, Y. H., Lovergine, F., Mahecha, M. D., Marzahn, P., Mattia, F., Musial, J. P., Preuschmann, S., Reichle, R. H., Satalino, G., Silgram, M., van Bodegom, P. M., Verhoest, N. E. C., Wagner, W., Walker, J. P., Wegmüller, U., and Loew, A.: A roadmap for high-resolution satellite soil moisture

- applications – confronting product characteristics with user requirements, *Remote Sens. Environ.*, 252, 112162, <https://doi.org/10.1016/j.rse.2020.112162>, 2021.
- Peres, D. J. and Cancelliere, A.: Derivation and evaluation of landslide-triggering thresholds by a Monte Carlo approach, *Hydrol. Earth Syst. Sci.*, 18, 4913–4931, <https://doi.org/10.5194/hess-18-4913-2014>, 2014.
- Peres, D. J. and Cancelliere, A.: Estimating return period of landslide triggering by Monte Carlo simulation, *J. Hydrol.*, 541, 256–271, <https://doi.org/10.1016/j.jhydrol.2016.03.036>, 2016.
- Peres, D. J. and Cancelliere, A.: Analisi degli impatti dei cambiamenti climatici sull'insnesco di frane superficiali, L'acqua, *Riv. Bimest. dell'Associazione Idrotec. Ital.*, 2, 71–82, 2018a.
- Peres, D. J. and Cancelliere, A.: Modeling impacts of climate change on return period of landslide triggering, *J. Hydrol.*, 567, 420–434, <https://doi.org/10.1016/j.jhydrol.2018.10.036>, 2018b.
- Peres, D. J. and Cancelliere, A.: Comparing methods for determining landslide early warning thresholds: potential use of non-triggering rainfall for locations with scarce landslide data availability, 18, 3135–3147, <https://doi.org/10.1007/s10346-021-01704-7>, 2021.
- Peres, D. J., Cancelliere, A., Greco, R., and Bogaard, T. A.: Influence of uncertain identification of triggering rainfall on the assessment of landslide early warning thresholds, *Nat. Hazards Earth Syst. Sci.*, 18, 633–646, <https://doi.org/10.5194/nhess-18-633-2018>, 2018.
- Peruccacci, S., Brunetti, M. T., Luciani, S., Vennari, C., and Guzzetti, F.: Lithological and seasonal control on rainfall thresholds for the possible initiation of landslides in central Italy, 139–140, 79–90, <https://doi.org/10.1016/j.geomorph.2011.10.005>, 2012a.
- Peruccacci, S., Brunetti, M. T., Luciani, S., Vennari, C., and Guzzetti, F.: Lithological and seasonal control on rainfall thresholds for the possible initiation of landslides in central Italy, 139–140, 79–90, <https://doi.org/10.1016/j.geomorph.2011.10.005>, 2012b.
- Piciullo, L., Calvello, M., and Cepeda, J. M.: Territorial early warning systems for rainfall-induced landslides, *Earth-Science Rev.*, 179, 228–247, <https://doi.org/10.1016/j.earscirev.2018.02.013>, 2018.
- Polemio, M. and Petrucci, O.: Rainfall as a Landslide Triggering Factor ;, *Landslides Res. Theory Pract.*, 1219–1226, 2000.
- Ponziani, F., Pandolfo, C., Stelluti, M., Berni, N., Brocca, L., and Moramarco, T.: Assessment of rainfall thresholds and soil moisture modeling for operational hydrogeological risk prevention in the Umbria region (central Italy), 9, 229–237, <https://doi.org/10.1007/s10346-011-0287-3>, 2012.
- Popescu, M. E.: A suggested method for reporting landslide causes, *Bull. Int. Assoc. Eng. Geol. - Bull. l'Association Int. Géologie l'Ingénieur*, 50, 71–74, <https://doi.org/10.1007/BF02594958>, 1994.
- Postance, B., Hillier, J., Dijkstra, T., and Dixon, N.: Comparing threshold definition techniques for rainfall-induced landslides: A national assessment using radar rainfall, *Earth Surf. Process. Landforms*, 43, 553–560, <https://doi.org/10.1002/ESP.4202>, 2018.
- Pumo, D., Carlino, G., Blenkinsop, S., Arnone, E., Fowler, H., and Noto, L. V.: Sensitivity of extreme rainfall to temperature in semi-arid Mediterranean regions, *Atmos.*

- Res., 225, 30–44, <https://doi.org/10.1016/j.atmosres.2019.03.036>, 2019.
- Rahardjo, H., Ong, T. H., Rezaur, R. B., and Leong, E. C.: Factors Controlling Instability of Homogeneous Soil Slopes under Rainfall, *J. Geotech. Geoenvironmental Eng.*, 133, 1532–1543, [https://doi.org/10.1061/\(asce\)1090-0241\(2007\)133:12\(1532\)](https://doi.org/10.1061/(asce)1090-0241(2007)133:12(1532)), 2007.
- Raia, S., Alvioli, M., Rossi, M., Baum, R. L., Godt, J. W., and Guzzetti, F.: Improving predictive power of physically based rainfall-induced shallow landslide models: A probabilistic approach, *Geosci. Model Dev.*, 7, 495–514, <https://doi.org/10.5194/gmd-7-495-2014>, 2014a.
- Raia, S., Alvioli, M., Rossi, M., Baum, R. L., Godt, J. W., and Guzzetti, F.: Improving predictive power of physically based rainfall-induced shallow landslide models: A probabilistic approach, *Geosci. Model Dev.*, 7, 495–514, <https://doi.org/10.5194/gmd-7-495-2014>, 2014b.
- Ramli, I., Devianti, D., Murthada, S., and Chandika, H.: Analysis of unsaturated hydraulic conductivity parameter in Central Aceh District, *IOP Conf. Ser. Earth Environ. Sci.*, 644, <https://doi.org/10.1088/1755-1315/644/1/012027>, 2021.
- Ran, Q., Hong, Y., Li, W., and Gao, J.: A modelling study of rainfall-induced shallow landslide mechanisms under different rainfall characteristics, *J. Hydrol.*, 563, 790–801, <https://doi.org/10.1016/j.jhydrol.2018.06.040>, 2018a.
- Ran, Q., Hong, Y., Li, W., and Gao, J.: A modelling study of rainfall-induced shallow landslide mechanisms under different rainfall characteristics, *J. Hydrol.*, 563, 790–801, <https://doi.org/10.1016/j.jhydrol.2018.06.040>, 2018b.
- Rao, A. R. and Burke, T. T.: PRINCIPAL COMPONENT ANALYSIS OF HYDROLOGIC DATA, 1997.
- Reder, A. and Rianna, G.: Exploring ERA5 reanalysis potentialities for supporting landslide investigations: a test case from Campania Region (Southern Italy), 18, 1909–1924, <https://doi.org/10.1007/S10346-020-01610-4/FIGURES/11>, 2021.
- Reed, P., Minsker, B. S., and Goldberg, D. E.: Simplifying multiobjective optimization: An automated design methodology for the nondominated sorted genetic algorithm-II, *Water Resour. Res.*, 39, 1–6, <https://doi.org/10.1029/2002WR001483>, 2003.
- Reichenbach, P., Cardinali, M., De Vita, P., and Guzzetti, F.: Regional hydrological thresholds for landslides and floods in the Tiber River Basin (central Italy), *Environ. Geol.*, 35, 146–159, <https://doi.org/10.1007/s002540050301>, 1998.
- Reid, M. E., Christian, S. B., Brien, D. L., and Henderson, S. T.: Scoops3D—Software to Analyze Three-Dimensional Slope Stability Throughout a Digital Landscape, 218, <https://doi.org/10.3133/tm14A1>, 2015.
- Rencher, A. C.: *Multivariate statistical inference and applications*, Wiley-Interscience, 1998.
- Reshad Md. Ekram Ali, L. W. T., Reshad Md. Ekram Ali, L. W. T., Rajinder Kumar Bhasin, S. A., Rajinder Kumar Bhasin, S. A., And, M. Z. U., And, M. Z. U., and Khan, M. M. H.: *Landslide Susceptibility of Chittagong City, Bangladesh, and Development of Landslides Early Warning System*, i, 13, 2016.
- Rex L. Baum, William Z. Savage, and J. W. G.: *Trigrs*, 1–4, 2008.
- Richards, L. A.: *Capillary conduction of liquids through porous mediums*, *Physics (College. Park. Md.)*, 1, 318–333, 1931.
- Rienecker, M. M., Suarez, M. J., Gelaro, R., Todling, R., Bacmeister, J., Liu, E., Bosilovich, M. G., Schubert, S. D., Takacs, L., Kim, G. K., Bloom, S., Chen, J., Collins, D.,

-
- Conaty, A., Da Silva, A., Gu, W., Joiner, J., Koster, R. D., Lucchesi, R., Molod, A., Owens, T., Pawson, S., Pegion, P., Redder, C. R., Reichle, R., Robertson, F. R., Ruddick, A. G., Sienkiewicz, M., and Woollen, J.: MERRA: NASA's modern-era retrospective analysis for research and applications, *J. Clim.*, 24, 3624–3648, <https://doi.org/10.1175/JCLI-D-11-00015.1>, 2011.
- Roccati, A., Faccini, F., Luino, F., Ciampalini, A., and Turconi, L.: Heavy rainfall triggering shallow landslides: A susceptibility assessment by a GIS-approach in a Ligurian Apennine catchment (Italy), 11, <https://doi.org/10.3390/w11030605>, 2019.
- Roccati, A., Paliaga, G., Luino, F., Faccini, F., and Turconi, L.: Rainfall threshold for shallow landslides initiation and analysis of long-term rainfall trends in a mediterranean area, <https://doi.org/10.3390/atmos11121367>, 2020.
- Rosi, A., Segoni, S., Catani, F., and Casagli, N.: Statistical and environmental analyses for the definition of a regional rainfall threshold system for landslide triggering in Tuscany (Italy), *J. Geogr. Sci.*, 22, 617–629, <https://doi.org/10.1007/s11442-012-0951-0>, 2012.
- Rosi, A., Segoni, S., Canavesi, V., Monni, A., Gallucci, A., and Casagli, N.: Definition of 3D rainfall thresholds to increase operative landslide early warning system performances, 18, 1045–1057, <https://doi.org/10.1007/s10346-020-01523-2>, 2021.
- Rossi, G., Catani, F., Leoni, L., Segoni, S., and Tofani, V.: HIRESSS: A physically based slope stability simulator for HPC applications, *Nat. Hazards Earth Syst. Sci.*, 13, 151–166, <https://doi.org/10.5194/nhess-13-151-2013>, 2013.
- Rosso, R., Rulli, M. C., and Vannucchi, G.: A physically based model for the topographic control on shallow landsliding, *Water Resour. Res.*, 30, 1153–1171, <https://doi.org/10.1029/93WR02979>, 2006.
- RT Pack, DG Tarboton, C. G.: *Sinmap 2 A Stability Index Approach To Terrain Stability Hazard Mapping*, 1999.
- Sabaghy, S., Walker, J. P., Renzullo, L. J., and Jackson, T. J.: Spatially enhanced passive microwave derived soil moisture: Capabilities and opportunities, *Remote Sens. Environ.*, 209, 551–580, <https://doi.org/10.1016/j.rse.2018.02.065>, 2018.
- Salciarini, D., Godt, J. W., Savage, W. Z., Conversini, P., Baum, R. L., and Michael, J. A.: Modeling regional initiation of rainfall-induced shallow landslides in the eastern Umbria Region of central Italy, 3, 181–194, <https://doi.org/10.1007/s10346-006-0037-0>, 2006.
- Salciarini, D., Fanelli, G., and Tamagnini, C.: A probabilistic model for rainfall–induced shallow landslide prediction at the regional scale, 14, 1731–1746, <https://doi.org/10.1007/s10346-017-0812-0>, 2017.
- Salvatici, T., Tofani, V., Rossi, G., D'Ambrosio, M., Tacconi Stefanelli, C., Benedetta Masi, E., Rosi, A., Pazzi, V., Vannocci, P., Petrolo, M., Catani, F., Ratto, S., Stevenin, H., and Casagli, N.: Application of a physically based model to forecast shallow landslides at a regional scale, *Nat. Hazards Earth Syst. Sci.*, 18, 1919–1935, <https://doi.org/10.5194/nhess-18-1919-2018>, 2018.
- Saulnier, G. M., Beven, K., and Obled, C.: Including spatially variable effective soil depths in TOPMODEL, *J. Hydrol.*, 202, 158–172, [https://doi.org/10.1016/S0022-1694\(97\)00059-0](https://doi.org/10.1016/S0022-1694(97)00059-0), 1997.
- Savage, W. Z., Godt, J. W., and Baum, R. L.: *A model for spatially and temporally distributed shallow landslide initiation by rainfall infiltration*, 2003.

-
- Scheidegger, A. E.: On the prediction of the reach and velocity of catastrophic landslides, *Rock Mech. Felsmechanik Mécanique des Roches*, 5, 231–236, <https://doi.org/10.1007/BF01301796>, 1973.
- Segoni, S., Leoni, L., Benedetti, A. I., Catani, F., Righini, G., Falorni, G., Gabellani, S., Rudari, R., Silvestro, F., and Rebola, N.: Towards a definition of a real-time forecasting network for rainfall induced shallow landslides, *Nat. Hazards Earth Syst. Sci.*, 9, 2119–2133, <https://doi.org/10.5194/nhess-9-2119-2009>, 2009.
- Segoni, S., Piciullo, L., and Gariano, S. L.: A review of the recent literature on rainfall thresholds for landslide occurrence, 15, 1483–1501, <https://doi.org/10.1007/s10346-018-0966-4>, 2018a.
- Segoni, S., Piciullo, L., and Gariano, S. L.: A review of the recent literature on rainfall thresholds for landslide occurrence, <https://doi.org/10.1007/s10346-018-0966-4>, 1 August 2018b.
- Segoni, S., Rosi, A., Lagomarsino, D., Fanti, R., and Casagli, N.: Brief communication: Using averaged soil moisture estimates to improve the performances of a regional-scale landslide early warning system, *Nat. Hazards Earth Syst. Sci.*, 18, 807–812, <https://doi.org/10.5194/NHESS-18-807-2018>, 2018c.
- Shanmugam, G. and Wang, Y.: The landslide problem, *J. Palaeogeogr.*, 4, 109–166, <https://doi.org/10.3724/SP.J.1261.2015.00071>, 2015.
- Shao, S. and Lo, E. Y. M.: Incompressible SPH method for simulating Newtonian and non-Newtonian flows with a free surface, *Adv. Water Resour.*, 26, 787–800, [https://doi.org/10.1016/S0309-1708\(03\)00030-7](https://doi.org/10.1016/S0309-1708(03)00030-7), 2003.
- Shen, P., Zhang, L., Chen, H., and Fan, R.: EDDA 2.0: Integrated simulation of debris flow initiation and dynamics considering two initiation mechanisms, *Geosci. Model Dev.*, 11, 2841–2856, <https://doi.org/10.5194/gmd-11-2841-2018>, 2018.
- Sidle, R. C. and Ochiai, H.: *Landslides: Processes, Prediction, and Land Use*, 2006.
- Simoni, S., Zanotti, F., Bertoldi, G., and Rigon, R.: Modelling the probability of occurrence of shallow landslides and channelized debris flows using GEOtop-FS, <https://doi.org/10.1002/hyp.6886>, 2008.
- Spencer, E.: A method of analysis of the stability of embankments assuming parallel inter-slice forces, 17, 11–26, <https://doi.org/10.1680/geot.1967.17.1.11>, 1967.
- Srivastava, R. and Yeh, T. -C J.: Analytical solutions for one-dimensional, transient infiltration toward the water table in homogeneous and layered soils, *Water Resour. Res.*, 27, 753–762, <https://doi.org/10.1029/90WR02772>, 1991.
- Stähli, M., Sättele, M., Huggel, C., McArdell, B. W., Lehmann, P., Van Herwijnen, A., Berne, A., Schleiss, M., Ferrari, A., Kos, A., Or, D., and Springman, S. M.: Monitoring and prediction in early warning systems for rapid mass movements, *Nat. Hazards Earth Syst. Sci.*, 15, 905–917, <https://doi.org/10.5194/nhess-15-905-2015>, 2015.
- Staley, D. M., Kean, J. W., Cannon, S. H., Schmidt, K. M., and Laber, J. L.: Objective definition of rainfall intensity-duration thresholds for the initiation of post-fire debris flows in southern California, 10, 547–562, <https://doi.org/10.1007/s10346-012-0341-9>, 2013.
- Stancanelli, L. M., Peres, D. J., Cancelliere, A., and Foti, E.: A combined triggering-propagation modeling approach for the assessment of rainfall induced debris flow susceptibility, *J. Hydrol.*, 550, 130–143, <https://doi.org/10.1016/j.jhydrol.2017.04.038>,

- 2017.
- Stanic, F., Delage, P., Cui, Y. J., Laure, E. D. E., Versini, P. A., Schertzer, D., and Tchiguirinskaia, I.: A new approach of accounting for impedance effects in Gardner's method of determining the hydraulic conductivity of unsaturated soils, *E3S Web Conf.*, 195, 1–5, <https://doi.org/10.1051/e3sconf/202019503012>, 2020.
- Strauch, R., Istanbuluoglu, E., and Riedel, J.: A new approach to mapping landslide hazards: A probabilistic integration of empirical and physically based models in the North Cascades of Washington, USA, *Nat. Hazards Earth Syst. Sci.*, 19, 2477–2495, <https://doi.org/10.5194/nhess-19-2477-2019>, 2019.
- Sun, G., Zheng, H., and Jiang, W.: A global procedure for evaluating stability of three-dimensional slopes, *Nat. Hazards*, 61, 1083–1098, <https://doi.org/10.1007/s11069-011-9963-9>, 2012.
- Tall, M., Albergel, C., Bonan, B., Zheng, Y., Guichard, F., Dramé, M. S., Gaye, A. T., Sintondji, L. O., Hountondji, F. C. C., Nikiema, P. M., and Calvet, J. C.: Towards a long-term reanalysis of land surface variables over western Africa: LDAS-Monde applied over Burkina Faso from 2001 to 2018, *Remote Sens.*, 11, <https://doi.org/10.3390/RS11060735>, 2019.
- Taylor Donald W.: *Fundamentals of Soil Mechanics*, 1948.
- Terlien, M. T. J.: The determination of statistical and deterministic hydrological landslide-triggering thresholds, *Environ. Geol.*, 35, 124–130, <https://doi.org/10.1007/s002540050299>, 1998.
- Tesfa, T. K., Tarboton, D. G., Chandler, D. G., and Mcnamara, J. P.: Modeling soil depth from topographic and land cover attributes, *Water Resour. Res.*, 45, 10438, <https://doi.org/10.1029/2008WR007474>, 2009.
- Thiebes, B. and Glade, T.: Landslide Early Warning Systems-fundamental concepts and innovative applications, *Landslides Eng. Slopes. Exp. Theory Pract.*, 3, 1903–1911, <https://doi.org/10.1201/b21520-238>, 2016.
- Thomas, M. A., Mirus, B. B., and Collins, B. D.: Identifying Physics-Based Thresholds for Rainfall-Induced Landsliding, *Geophys. Res. Lett.*, 45, 9651–9661, <https://doi.org/10.1029/2018GL079662>, 2018.
- Thomas, M. A., Collins, B. D., and Mirus, B. B.: Assessing the Feasibility of Satellite-Based Thresholds for Hydrologically Driven Landsliding, *Water Resour. Res.*, 55, 9006–9023, <https://doi.org/10.1029/2019WR025577>, 2019.
- Tofani, V., Bilocchi, G., Rossi, G., Segoni, S., D'Ambrosio, M., Casagli, N., and Catani, F.: Soil characterization for shallow landslides modeling: a case study in the Northern Apennines (Central Italy), 14, 755–770, <https://doi.org/10.1007/s10346-017-0809-8>, 2017.
- Topp, G. C., Davis, J. L., and Annan, A. P.: Electromagnetic determination of soil water content: Measurements in coaxial transmission lines, *Water Resour. Res.*, 16, 574–582, <https://doi.org/10.1029/WR016i003p00574>, 1980.
- Tran, T. V., Alvioli, M., Lee, G., and An, H. U.: Three-dimensional, time-dependent modeling of rainfall-induced landslides over a digital landscape: a case study, 15, 1071–1084, <https://doi.org/10.1007/s10346-017-0931-7>, 2018.
- Tuli, A. and Hopmans, J. W.: Effect of degree of fluid saturation on transport coefficients in disturbed soils, *Eur. J. Soil Sci.*, 55, 147–164, <https://doi.org/10.1046/j.1365-2389.2003.00551.x>, 2004.

-
- Ugai, K.: Three-Dimensional Slope Stability Analysis By Slice Methods. Proceedings Of The Sixth International Conference On Numerical Methods In Geomechanics, 11-15 April 1988, Innsbruck, Austria. Volumes 1-3, Publ. Balkema, 1988.
- Valentino, R., Montrasio, L., Losi, G. L., and Bittelli, M.: An empirical model for the evaluation of the degree of saturation of shallow soils in relation to rainfalls, *Can. Geotech. J.*, 48, 795–809, <https://doi.org/10.1139/t10-098>, 2011.
- Valentino, R., Meisina, C., Montrasio, L., Losi, G. L., and Zizioli, D.: Predictive Power Evaluation of a Physically Based Model for Shallow Landslides in the Area of Oltrepò Pavese, Northern Italy, *Geotech. Geol. Eng.*, 32, 783–805, <https://doi.org/10.1007/s10706-014-9758-3>, 2014.
- Varnes, D.: Slope Movement Types and Processes, *Spec. Rep.*, 176, 11–33, 1978.
- Venturella, G.: Climatic and pedological features of Sicily, 17, 47–53, 2004.
- Vischel, T., Pegram, G. G. S., Sinclair, S., Wagner, W., and Bartsch, A.: Comparison of soil moisture fields estimated by catchment modelling and remote sensing: A case study in South Africa, *Hydrol. Earth Syst. Sci.*, 12, 751–767, <https://doi.org/10.5194/hess-12-751-2008>, 2008.
- Wagner, W., Hahn, S., Kidd, R., Melzer, T., Bartalis, Z., Hasenauer, S., Figa-Saldana, J., De Rosnay, P., Jann, A., and Schneider, S.: The ASCAT soil moisture product: A review of its specifications, validation results, and emerging applications, *Meteorol. Zeitschrift*, 2013.
- van Westen, C. J., Castellanos, E., and Kuriakose, S. L.: Spatial data for landslide susceptibility, hazard, and vulnerability assessment: An overview, *Eng. Geol.*, 102, 112–131, <https://doi.org/10.1016/j.enggeo.2008.03.010>, 2008.
- Wicki, A., Lehmann, P., Hauck, C., Seneviratne, S. I., Waldner, P., and Stähli, M.: Assessing the potential of soil moisture measurements for regional landslide early warning, 17, 1881–1896, <https://doi.org/10.1007/s10346-020-01400-y>, 2020.
- Willenberg, H., Eberhardt, E., Loew, S., McDougall, S., and Hungr, O.: Hazard assessment and runout analysis for an unstable rock slope above an industrial site in the Riviera valley, Switzerland, 6, 111–119, <https://doi.org/10.1007/s10346-009-0146-7>, 2009.
- Xu, X., Frey, S. K., Boluwade, A., Erler, A. R., Khader, O., Lapen, D. R., and Sudicky, E.: Evaluation of variability among different precipitation products in the Northern Great Plains, *J. Hydrol. Reg. Stud.*, 24, 100608, <https://doi.org/10.1016/J.EJRH.2019.100608>, 2019.
- Yao, W., Li, C., Zhan, H., and Zeng, J.: Time-dependent slope stability during intense rainfall with stratified soil water content, *Bull. Eng. Geol. Environ.*, October, <https://doi.org/10.1007/s10064-018-01437-3>, 2019a.
- Yao, W., Li, C., Zhan, H., and Zeng, J.: Time-dependent slope stability during intense rainfall with stratified soil water content, *Bull. Eng. Geol. Environ.*, 1st October, <https://doi.org/10.1007/s10064-018-01437-3>, 2019b.
- Yusoff, Y., Ngadiman, M. S., and Zain, A. M.: Overview of NSGA-II for optimizing machining process parameters, in: *Procedia Engineering*, 3978–3983, <https://doi.org/10.1016/j.proeng.2011.08.745>, 2011.
- Zeng, J., Yuan, X., Ji, P., and Shi, C.: Effects of meteorological forcings and land surface model on soil moisture simulation over China, *J. Hydrol.*, 603, 126978, <https://doi.org/10.1016/j.jhydrol.2021.126978>, 2021.
-

-
- Zhang, L. L., Zhang, J., Zhang, L. M., and Tang, W. H.: Stability analysis of rainfall-induced slope failure: a review, *Proc. Inst. Civ. Eng. - Geotech. Eng.*, 164, 299–316, <https://doi.org/10.1680/geng.2011.164.5.299>, 2011.
- Zhao, B., Dai, Q., Han, D., Dai, H., Mao, J., and Zhuo, L.: Probabilistic thresholds for landslides warning by integrating soil moisture conditions with rainfall thresholds, *J. Hydrol.*, 574, 276–287, <https://doi.org/10.1016/j.jhydrol.2019.04.062>, 2019a.
- Zhao, B., Dai, Q., Han, D., Dai, H., Mao, J., and Zhuo, L.: Probabilistic thresholds for landslides warning by integrating soil moisture conditions with rainfall thresholds, *J. Hydrol.*, 574, 276–287, <https://doi.org/10.1016/j.jhydrol.2019.04.062>, 2019b.
- Zhao, B., Dai, Q., Han, D., Dai, H., Mao, J., and Zhuo, L.: Probabilistic thresholds for landslides warning by integrating soil moisture conditions with rainfall thresholds, *J. Hydrol.*, 574, 276–287, <https://doi.org/10.1016/j.jhydrol.2019.04.062>, 2019c.
- Zieher, T., Schneider-Muntau, B., and Mergili, M.: Are real-world shallow landslides reproducible by physically-based models? Four test cases in the Laternser valley, Vorarlberg (Austria), 14, 2009–2023, <https://doi.org/10.1007/s10346-017-0840-9>, 2017a.
- Zieher, T., Schneider-Muntau, B., and Mergili, M.: Are real-world shallow landslides reproducible by physically-based models? Four test cases in the Laternser valley, Vorarlberg (Austria), 14, 2009–2023, <https://doi.org/10.1007/s10346-017-0840-9>, 2017b.
- Zizioli, D., Meisina, C., Valentino, R., and Montrasio, L.: Comparison between different approaches to modeling shallow landslide susceptibility: A case history in Oltrepo Pavese, Northern Italy, *Nat. Hazards Earth Syst. Sci.*, 13, 559–573, <https://doi.org/10.5194/nhess-13-559-2013>, 2013.
- Zwartendijk, B. W., van Meerveld, H. J., Ghimire, C. P., Bruijnzeel, L. A., Ravelona, M., and Jones, J. P. G.: Rebuilding soil hydrological functioning after swidden agriculture in eastern Madagascar, *Agric. Ecosyst. Environ.*, 239, 101–111, <https://doi.org/10.1016/j.agee.2017.01.002>, 2017.